Light-Dependent Growth Kinetics and Mathematical Modeling of *Synechocystis* sp. PCC 6803

by

Levi Straka

A Dissertation Presented in Partial Fulfillment
of the Requirements for the Degree
Doctor of Philosophy

Approved March 2017 by the
Graduate Supervisory Committee:

Bruce Rittmann, Chair
Peter Fox
César Torres

ARIZONA STATE UNIVERSITY

May 2017

ABSTRACT

One solution to mitigating global climate change is using cyanobacteria or single-celled algae (collectively microalgae) to replace petroleum-based fuels and products, thereby reducing the net release of carbon dioxide. This work develops and evaluates a mechanistic kinetic model for light-dependent microalgal growth. Light interacts with microalgae in a variety of positive and negative ways that are captured by the model: light intensity (LI) attenuates through a microalgal culture, light absorption provides the energy and electron flows that drive photosynthesis, microalgae pool absorbed light energy, microalgae acclimate to different LI conditions, too-high LI causes damage to the cells' photosystems, and sharp increases in light cause severe photoinhibition that inhibits growth. The model accounts for all these phenomena by using a set of state variables that represent the pooled light energy, photoacclimation, PSII photo-damage, PSII repair inhibition and PSI photodamage. Sets of experiments were conducted with the cyanobacterium *Synechocystis* sp. PCC 6803 during step-changes in light intensity and flashing light. The model was able to represent and explain all phenomena observed in the experiments. This included the spike and depression in growth rate following an increasing light step, the temporary depression in growth rate following a decreasing light step, the shape of the steady-state growth-irradiance curve, and the "blending" of light and dark periods under rapid flashes of light. The LI model is a marked improvement over previous light-dependent growth models, and can be used to design and interpret future experiments and practical systems for generating renewable feedstock to replace petroleum.

ACKNOWLEDGMENTS

There are many people whose support, intellectual and moral, has allowed me to prepare this dissertation. I would like to thank everybody who has been part of my life for the past six years. Specifically, and this is not exhaustive:

I would like to thank my peers in the Photobioreactor team, Biodesign Swette Center for Environmental Biotechnology, and IGERT SUN fellowship program, for their mentorship, collaboration, feedback and tolerance. This work would not be possible from myself alone. A few members include: Chao Zhou, Hyun Woo Kim, Binh Nguyen, Alex Zevin, Matt Thompson, Brendan Cahill, Everett Eustance, Joseph Laureanti, Anna Beiler, Lisa Dirks, and Leah Holton.

I would like to thank my friends and family who kept me going throughout this process. The path to a PhD can be tedious, lonely, and often feel unrewarding. These people vitalize me, and remind me that my life is about more than work. In addition to the peers listed above I would like to specifically recognize the following people: Haley Lowrance, Dave Hanigan, Allan Greenfield, Matt Miles, Chase Holton, Steve Goodman, Sara Carey, Onur Apul, and Frank, Donna, Luke, and Umnia Straka.

Finally, I would like to thank Arizona State University and all the faculty and staff who have worked with me, taught a class that I took, or coordinated what I need to complete my work. This includes my graduate supervisory committee, Bruce Rittmann, Peter Fox, and César Torres, and our lab managers Carole Flores and Diane Hagner. I underscore that none of this work would have been possible without Bruce, who provided me with the opportunity to come back to school, guidance throughout my degree, and funding for the work. This work was made possible by Dean's funding from ASU, the NSF IGERT SUN fellowship, and Brian Swette for his support to the Swette Center.

TABLE OF CONTENTS

Page

CHAPTER Page

CHAPTER Page

LIST OF TABLES

Table Page

LIST OF FIGURES

Figure Page

Figure Page

1. INTRODUCTION

1.1. Global Warming, The Big Problem

It is the consensus of the scientific community that the anthropogenic release of carbon dioxide is leading to an increase in temperatures globally (97% of papers expressing an opinion on global warming between 1991 and 2011 agree (Cook et al., 2013)). Increasing global temperature has innumerous environmental consequences, including changes in global water cycles, glacial and arctic ice melting, and more severe-weather events (IPCC, 2014).

The scientific premise of global climate change is that the Earth absorbs sunlight (ultraviolet and visible wavelengths) and reflects or re-emits most, but not all of the energy back to space in infrared wavelengths. Certain gases in the atmosphere (greenhouse gases) prevent some of the infrared light energy from escaping the earth to space, which then warms the earth's surface temperature (NOAA, 2017). The naturally occurring greenhouse gases are carbon dioxide (CO_2), water vapor, methane, and nitrous oxide. On the one hand, the presence of the greenhouse gases is why the earth's temperature is warm enough to sustain life. On the other hand, humans have been burning fossil fuels since the industrial revolution, and this has led to an excess release of greenhouse gases, mainly CO_2, to the atmosphere.

The relationship of temperature to greenhouse gases has been known for over a century. For example, in 1896, Svante Arrhenius calculated that doubling the atmospheric CO_2 (then about 290 ppm) would result in global temperatures rising 5-6° C (Arrhenius, 1896). With the advent of ice-core sampling and atmosphere CO_2 monitoring, the strong correlation between atmospheric CO_2 levels and global temperature is empirically proven, and temperatures clearly are rising in response to atmospheric CO_2 levels (Petit et al., 1999).

The unprecedented levels of CO_2 in the atmosphere, recently breeching 400 ppm (Keeling, 2015) as opposed to the geological high of ~300 ppm (Petit et al., 1999), is primarily due to the burning of fossil fuels. In 2012, the world produced 13,500 Mtoe (million tonnes of oil equivalent) of energy, of which 82% was from coal, gas, and oil whose combustion emitted 31.7 Gt of CO_2 (IEA, 2014). Furthermore, the past three consecutive years (2014, 2015, and 2016) have broken the record for highest global average temperatures (Gillis, 2017). The Intergovernmental Panel on Climate Change (IPCC) estimates that it is extremely likely that more than half of the warming is caused by human contributions (IPCC, 2014).

One of the most obvious effects of global temperature rise is that Arctic, Antarctic, and glacial ice will melt, thereby raising sea levels. Using tide gauge data, Hay et. al. (2015) found that the global mean sea-level rose at a rate of 1.2 ± 0.2 mm per year between 1901 and 1990 and 3.0 ± 0.7 mm per year from 1993 to 2010 (Hay et al., 2015). Evidence shows that Greenland ice sheets (one of the largest contributors to sea-level rise thus far) have retreated a cumulative 267 km between 2000 and 2010 (Murray et al., 2015). While these changes are mild at present, a sea level rise of 10m puts roughly 25% of the US population under water, and if all ice melts, the sea level could rise by as much as 80 m (Poore et al., 2000).

In addition to melting ice, the direct effects of global temperature rise on the global water systems are changes in evaporation and precipitation. With increasing global temperature, evaporation will increase in some areas, but precipitation will increase in others. This leads to a redistribution of water and increase of extreme weather events (Huntington, 2006). In general, areas that are already water rich will receive more precipitation, and areas that are water limited will become drier (Manabe et al., 2004).

A consequence to human civilization is the effect global climate change will have on agricultural production. Higher temperatures have the potential for increasing occurrence of disease outbreaks that could be devastating to crops (Juroszek and Tiedemann, 2015), and change in water availability is a large issue (Huntington, 2006). Changes in crop production will be region specific, and more studies report overall negative impacts than positive (IPCC, 2014). In particular, areas of low latitude will see more negative affects compared to areas of high latitude (Rosenzweig et al., 2014).

Ecosystem stress is complex, but a metric for assessing stress is extinctions. Coral reef ecosystems are particularly sensitive to climate change and have received a lot of attention. Research shows that the number of reports of coral reef bleaching (a stress response where coral rejects the symbiotic algae inhabiting it) has drastically increased since the early 1980s, which correlates well with increases in sea temperatures (Baker et al., 2008). Looking to the land, tree mortality has been increasing in some forests globally in response to climate change (Allen et al., 2010). Additionally, terrestrial organisms have been moving to higher latitudes and higher elevations (Chen et al., 2011). Projections suggest a continued decline in biodiversity worldwide (Pereira et al., 2010), and a survey of the fossil record over the past 500 million years shows that warmer periods correlate to relatively low biodiversity and higher levels of extinction (Mayhew et al., 2008).

The changes I've outlined are happening extremely fast when considering a geological time scale, which is the time scale over which large swings in atmospheric CO_2 have taken in the past. At present, the effects have been mild, but already we are seeing trends of increased water scarcity, reduced crop yield, and lower biodiversity.

The climate-change trends can be undone only by equally rapid net removal of CO_2 from the atmosphere. No one approach will solve the CO_2 problem; we will need to

embrace a myriad of strategies to mitigate CO_2 build up and climate change: e.g., increased use of carbon-neutral alternative energy sources (wind, solar, and biofuels), energy efficiency, and atmospheric carbon sequestration. Global climate change is the environmental challenge of our era, and delays in implementing mitigation strategies will make the challenge far more difficult to address in the future.

1.2. Microalgae as Part of the Solution

Microalgae (used here to refer to single celled eukaryotic algae and prokaryotic cyanobacteria) are aquatic organisms able to perform oxygenic photosynthesis, allowing them to fix atmospheric CO_2 into organic biomass, the same as plants. This gives them the potential advantages of removing CO_2 from the air (reducing the effect on global climate change if the biomass is sequestered somehow) and creating carbon-neutral products. What sets microalgae apart from most traditional crops is that they do not require arable land, since they grow in aquatic environments (very important when considering growing them for fuel as to not compete with food production) and can achieve higher production rates (Chisti, 2007; Singh et al., 2011). Microalgae are responsible for the original transformation of earth's atmosphere from a highly reduced environment to an oxygen-rich atmosphere roughly 2.5 billion years ago, known as the Great Oxidation Event (Schirrmeister et al., 2015).

The largest opportunity for microalgae to reduce the release of CO_2 to the atmosphere is by replacing fossil fuels with algae-derived fuels. This is particularly appealing for transportation fuels, where other renewable energy sources (wind and solar) are not feasible without the use of batteries. Microalgae have been proposed for fuel production in several ways, including:

- Directly producing hydrogen gas via the hydrogenase or nitrogenase enzyme
- extracting sugars from algae and fermenting them into ethanol
- extracting fats from algae and performing transesterification to produce biodiesel
- anaerobically digesting algae biomass to produce methane
- liquefying algae biomass to produce bio-oil, hydrogen and methane

- metabolic engineering of algae to produce and secrete biofuels (Bahadar and Bilal Khan, 2013; Daroch et al., 2013).

Each approach has its own advantages and challenges, and many companies are attempting to commercialize different approaches (Bahadar and Bilal Khan, 2013).

In addition to fuel, the cultivation of microalgae has been suggested for the production of other products including: biomass (as a health food, aquaculture feed, or animal feed), poly-unsaturated fatty acids, anti-oxidants, coloring substances, and fertilizers (DOE, 2010). Non-fuel products also can be looked at as co-products, where the primary goal of algae cultivation is fuel, but the residual still holds some value. As an example, if microalgae biomass is separated into lipids, carbohydrates, and proteins, the lipids and carbohydrates can both be used for fuel production, and the proteins can be used as animal feed (DOE, 2010). Each path has challenges to commercialization (or expanded commercialization), but any market that microalgae enters has potential to reduce energy input (due to photosynthetic capacity) or reduce the demand on arable land.

Picking a strain of microalgae with the desired properties is of paramount importance. Natural ecosystem support over 36,000 species of algae (Razzak et al., 2013), including predominantly microalgae, but also macrophytes, or seaweed. Despite the opportunity to prospect for a better organism for any given application, the vast majority of algae species have not been analyzed for their chemical content (Spolaore et al., 2006) or growth kinetics. While it has been the goal of my PhD work to characterize the growth mechanics of one microalgae species (the cyanobacterium *Synechocystis* sp. PCC 6803), the trends of my findings can be applied to many other microalgae species. Many of the molecular mechanisms of photosynthesis are the same or very similar among all oxygenic phototrophs. While the kinetics would not be exactly the same, they

should follow the same trends, which provides insight into characterizing the growth of other species. My work is not as applicable to marcrophytes, because there is further complexity associated with multicellular organisms.

I collectively refer to single-celled eukaryotic algae and cyanobacteria as microalgae because they share similar growth behavior; however, cyanobacteria are part of the domain of bacteria and are therefore not algae, which are eukaryotes. All experimental work in this dissertation was done with the cyanobacterium *Synechocystis* sp. PCC 6803 (simply *Synechocystis* from here), because it is a representative cyanobacterium (there is expertise on the organism at ASU and in the literature), it is fast growing, and efforts at Arizona State University are making modified strains to produce various valuable products such as 3-hydroxypropionate and lauric acid.

1.3. Molecular Mechanisms of Photosynthesis

The ability of plants and microalgae to capture sunlight occurs because of their ability to perform oxygenic photosynthesis (i.e., photosynthesis in which oxygen is produced). In this section I summarize a basic understanding of how oxygenic photosynthesis works, and this understanding is essential to the light-dependent work I present in Chapters 3-7. Most information here is generally accepted in the field of photosynthesis, but I have used one textbook, *Molecular Mechanisms of Photosynthesis*, by Bob Blankenship as my primary reference.

Oxygenic photosynthesis can be thought of as a four-step process: 1) light absorption, 2) primary electron transfer, 3) energy stabilization, and 4) carbon fixation. The main components of these four processes are antenna pigments, the two photosystems (PSI and PSII), the electron transport chain, and the Calvin cycle respectively. (Blankenship, 2002)

Visible light is a narrow wavelength range of electromagnetic radiation (EMR). EMR is physically described as having a particle and wave nature. The quantum unit of EMR is the photon, which is described as having a corresponding wavelength (λ; the wavelength also describes the energy of the photon; higher λ = lower energy). EMR from the sun reaching earth (sunlight) contains infrared radiation (λ = 800 nm to 1000000 nm), visible light (λ = 400 nm to 800 nm), and ultraviolet radiation (λ = 10 nm to 400 nm) composing 53%, 44%, and 3% of the total energy respectfully (Britannica, 2017; Tennessee, 2017). The pigments used by phototrophic organisms typically absorb light in the visible light spectrum, and, therefore, this light is also referred to as Photosynthetically Active Radiation, or PAR. Thus, throughout this dissertation I refer to the intensity of light energy as a quantity of PAR photons per time (photon flux; μmol m^{-2} s^{-1}), which can be converted to energy (E; Joules(J)) by using $E = hc/\lambda$, where h is

Planck's constant ($6.63*10^{-34}$ J s) and c is the speed of light ($3.0*10^{8}$ m s^{-1}) (Lindeburg, 2015). Most light sources do not have a single wavelength of light. For the PAR spectrum of sunlight, the incident energy averages out to approximately 0.22 W m^{-2} per μmol m^{-2} s^{-1} (Chambers, 2017).

Every material has different absorptive and reflective properties. Light absorption occurs by a photon contacting an electron with a similar wavelength, causing that electron to excite. An excited electron does not last long, and it either releases the energy in the form of heat or passes the excitation energy on to another electron (Henderson, 2017). In the case of photosynthesis, the pigment properties are such that the absorbed light energy is passed from antenna pigment to antenna pigment until the energy reaches the reaction center of one of the photosystems and begins the second step, primary electron transfer (Blankenship, 2002).

Different species of microalgae have different pigments, including chlorophylls, carotenoids, and phycobilisomes. Chlorophyll a is the most common pigment, as it is in all oxygenic phototrophs and is the majority of pigmentation in plants. All the chlorophylls have slightly different absorbance spectra, but none is good at absorbing green light, which is why plants and most microalgae appear green. Carotenoids on the other hand, are efficient at absorbing green light, but not as efficient at orange light. During the fall in deciduous trees, the leaves can turn orange because the chlorophyll breaks down before the carotenoids do. Carotenoids also serve the added purpose of what is called non-photochemical quenching. This is essentially the process of dissipating electron excitation energy as heat, which is useful when an excess of light energy would otherwise cause photodamage. Phycobilisomes are protein structures, which are the most common pigments in cyanobacteria including *Synechocystis*. As I discuss in more detail in Chapters 3 and 4, microalgae also have the ability to change the

absorptive properties of their pigments in response to changing light. (Blankenship, 2002)

The second step in photosynthesis is primary charge separation, which occurs in the reaction centers of the photosystems. The reaction center itself is made up of two chlorophyll a molecules that effectively function as a semiconductor. When excitation energy is funneled into the reaction center by antenna pigments, the excited electron is removed and passed down an electron transport chain (step 3) leaving the pair of chlorophylls oxidized. The oxidized reaction center is then reduced by a low energy electron from the oxygen evolving complex in Photosystem II, as well as by plastocyanin in Photosystem I. The oxygen-evolving complex in PSII generates oxygen by splitting water. (Blankenship, 2002)

Step three is the process of transforming these separated electrons into more stable stored energy in the forms of NADPH/NADH or ATP. After charge separation and to avoid recombination (the electron transfers back to the donor releasing heat), a series of very rapid reactions separate the electron from the donor; this is known as the electron-transport chain. While each consecutive electron carrier is at a lower energy level, thereby dissipating some energy, this strategy ensures nearly 100% capture rate of charge separated electrons. (Blankenship, 2002)

Oxygenic photosynthesis uses two photosystems (PSI and PSII), which interact in what is called the Z scheme, as pictured in Figure 1.1 (along with the role of steps 1 and 2). Electrons originate in water, which is split in the oxygen-evolving complex, and they then reduce the PSII reaction center (P680). After P680 is activated, it becomes oxidized as the excited electron passes through a series of quinone electron carriers to the cytochrome b_6f complex. The cytochrome b_6f complex further transfers the electron to a plastocyanin electron carrier meanwhile pumping protons through the membrane to

create a proton motive force. The PSI reaction center (P700) receives electrons from plastocyanin, and, once activated, follows a similar oxidation/reduction to P680, except that P700 is more reduced than P680. Finally, the electron is passed through another series of electron carriers to NADH or NADPH as the terminal electron acceptor. (Blankenship, 2002)

An alternate pathway, cyclic electron transfer, uses an electron carrier before NADH/NADPH (ferredoxin) to pass the electron back to the cytochrome b_6f complex, allowing for additional proton pumping. The proton motive force is used to drive the ATP synthase enzyme, which generates ATP. The ratio of PSI to PSII therefor determines the ratio of ATP to NADPH generated from photosynthesis. It is these products that then go on to fuel cellular processes, in particular the Calvin cycle in step 4. (Blankenship, 2002)

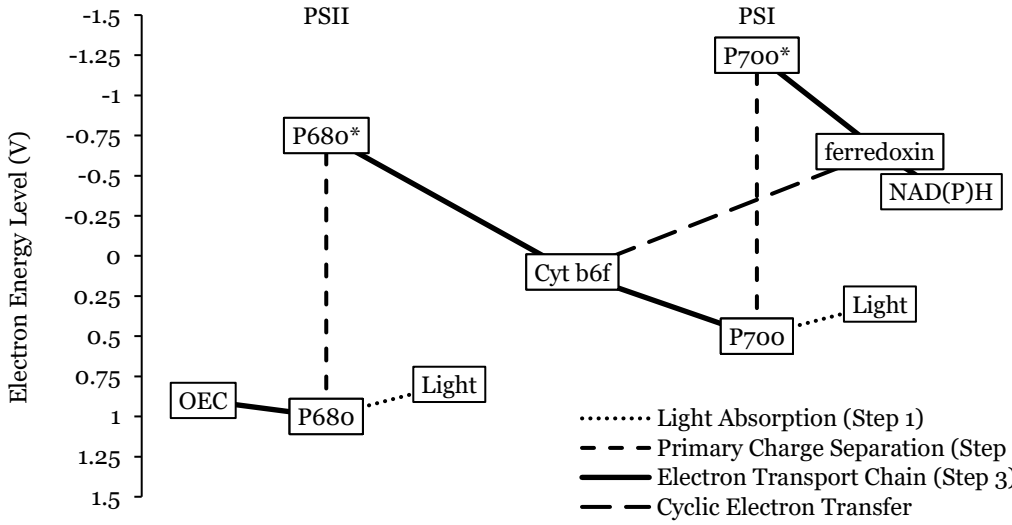

Figure 1.1: The Z scheme for electron transfer in oxygenic photosynthesis illustrating the first three steps of photosynthesis. OEC is oxygen evolving complex, P680 and P700 are the PSII and PSI reaction centers respectively, cyt b_6f is the cytochrome b_6f complex, and ferredoxin and NADPH/NADH are electron carriers. Light energy is absorbed and funneled into a reaction center (P680 or P700; step 1), the reaction center becomes activated donating an electron (step 2), and the electron is passed through an electron transport chain to stabilize the charge (step 3). Cyclic electron transfer occurs when an electron is passed from ferredoxin in PSI back to the cytochrome b_6f complex for additional proton motive force.

In the fourth step, ATP and NADPH are used to fix carbon dioxide into glucose through the Calvin cycle, also known as the Calvin-Benson-Bassham cycle, reductive pentose phosphate cycle, C3 cycle, light-independent reactions of photosynthesis, and the dark reactions of photosynthesis. The sugars from the Calvin cycle are used in cell metabolism, including growth. The details of the Calvin cycle are complex and not especially critical to this work. Nonetheless, one step that warrants further discussion is the first step in the Calvin cycle, carboxylation (binding of carbon dioxide), which is carried out by the RuBisCO enzyme (Blankenship, 2002). RuBisCO is a very important enzyme because its activity accounts for nearly all organic carbon on earth, and it is thought to be the most abundant protein (Ellis, 2010; Feller et al., 2008). However, RuBisCO is inefficient, and this could be a limitation in the use of biofuels over other solar energy capture technologies (Ellis, 2010). To combat this inefficiency, microalgae have developed carbon concentrating mechanisms in order to improve the rate of carbon fixation by RuBisCO (Wang et al., 2011). In Chapter 5, I use RuBisCO as the rate-limiting step to computing a theoretical maximum growth rate of *Synechocystis*.

1.4. Structure of the Dissertation

The opportunities for microalgae to play a role in reducing atmospheric CO_2 depend on growing them as efficiently as possible, because cultivation is a significant cost in microalgae products (Davis et al., 2011). Optimizing algal growth conditions, however, can be difficult, because many factors can affect the growth of algae, including:

- all the chemical constituents in the growth medium
- any other microorganisms in the community
- metabolites released by the microalgae or other members of the community
- aggregation, including as biofilms
- variable light and temperature conditions
- history of the algae itself (acclimation and adaptation).

The major body of work I present in this dissertation is about growth kinetics of *Synechocystis* based on changing light intensity (Chapters 3-7). Light has unique and complex effects, including its attenuation through a culture, photodamage, and photoacclimation. Understanding how light interacts with microalgae is paramount to a mechanisms-based understanding of photosynthesis. Isolating light effects, however, requires a basic understanding of the effects of other mechanisms. Therefore, I took several actions in an effort to standardize all work, and maintain consistency for the light experiments:

- Used standard BG-11 growth media
- pH was controlled to neutral to slightly alkaline (7-9)
- All reactor components were sterilized
- Steady-state behavior was established before looking at a dynamic change

- Temperature was maintained at 30°C

In sections 1.5 and 1.6, I discuss the theory behind experimental measures taken to minimize growth effects of carbon and nitrogen (the largest two nutrient inputs to cell growth) respectively. Similarly, in section 1.7, I address how the microbial community can affect microalgae cultivation and the measures I took to try to minimize effects. In Chapter 2, I present work that I conducted on phosphorus limitation and the role of the microbial community on Phosphorus limitation.

Chapters 3-7 include all work I conducted on light-dependent growth kinetics. Chapter 3 establishes a basis for photoacclimation by demonstrating that biomass grown at higher intensity light absorbs a lower fraction of light than biomass grown at lower intensity light. In Chapter 4, I present a light-dependent growth model that includes photoacclimation (based on the trend from Chapter 3), photodamage, and photodamage repair. This model is parameterized and further discussed in Chapter 5, and is used to explain results from flashing light experiments in Chapter 6 and changes in light intensity caused by mixing of concentrated cultures in Chapter 7.

Mathematical modeling is a powerful tool for understanding the complex, interacting phenomena involved with culturing microalgae, as well as maximizing production yields. A mathematical model is a series of mathematical equations that represent the critical biochemical, chemical, and transport processes of a system. A model should give a comprehensive and quantitative representation of the processes occurring in a system, and it can be used to track the chemical and biological constituents. This capability makes it possible to interpret experimental results mechanistically and to apply that understanding to practical design and operations strategies, as well as to the design of well-informed experiments for research. The most significant outcome of this dissertation is that, from the light-dependent model I

developed and presented in Chapter 4, I was able to mechanistically explain experimental results in Chapters 5-7.

1.5. Carbon kinetics

Carbon makes up the largest fraction of microalgae by mass, totaling just under 50% for *Synechocystis* (Kim et al., 2010), which is typical of bacteria (B E Rittmann and McCarty, 2001) and microalgae (Mirón et al., 2003). Therefore, carbon availability is important for growth. Some microalgae are capable of growing heterotrophically or mixotrophically (Girard et al., 2014), although in the interest of sun-energy capture, I focus on photoautotrophic growth, for which the carbon source is inorganic carbon (C_i).

In aquatic environments, C_i becomes available to microalgae primarily by gaseous CO_2 dissolving from air (Keymer et al., 2013). The rate of this process can be approximated according to a two-film theory:

$$\frac{d[H_2CO_3^*]}{dt} = K_L a([H_2CO_3^*]_s - [H_2CO_3^*]) \qquad \text{Equation 1.1}$$

where K_La is the volumetric mass transfer coefficient, $[H_2CO_3^*]$ is the combined concentration of H_2CO_3 and aqueous CO_2, and $[H_2CO_3^*]_s$ is $[H_2CO_3^*]$ at equilibrium with the dissolving gas (Metcalf & Eddy, 2003). Two-film theory assumes that the rate-limiting mass-transfer step is diffusion through two thin films at the liquid-gas interface; therefore, Fick's Law for diffusion applies (Metcalf & Eddy, 2003). Gas with a higher CO_2 content has a higher $[H_2CO_3^*]_s$ and, therefore, leads to faster CO_2 delivery (Kim et al., 2010). K_La is dependent on the mixing conditions in the fluid, and surface area in contact with the gas (Metcalf & Eddy, 2003). In engineered systems, gas is commonly bubbled through the solution to increase the surface area and increase mixing (Jones and Harrison, 2014).

Dissolved CO_2 is subject to acid-base chemistry in the solution and partitions into carbonic acid ($H_2CO_3^*$), bicarbonate (HCO_3^-), and carbonate (CO_3^{2-}) (Snoeyink and Jenkins, 1980). Different species of microalgae have different affinities for either $H_2CO_3^*$

or HCO_3^- (Kaplan and Reinhold, 1999), while utilization of CO_3^{2-} has not been documented. If the pH gets too high (above 10.3), the dominant C_i species will be CO_3^{2-}, and, therefore, unusable, however, this will also make the concentration of $H_2CO_3^*$ very low, increasing the mass transfer of CO_2 to solution. The alkalinity (capacity to neutralize acids) of the growth media is directly related to the capacity of the solution to hold C_i (Nguyen and Rittmann, 2015). High alkalinity increases speciation of $H_2CO_3^*$ to HCO_3^- and CO_3^{2-} leading to faster mass transfer, and higher levels of C_i in the solution. During growth on standard BG-11 growth media, the alkalinity is increased as microalgae grow, and, thus, an excess of C_i is easily achieved (Nguyen and Rittmann, 2015). This will be addressed further in section 1.6.

In unpublished work, Hyun Woo Kim, Seongjun Park and Bruce Rittmann (2012) determined a C_i-limitation saturation growth curve with a half maximum rate concentration (K_{Ci}) of 0.6 $mgC_i\ L^{-1}$ for *Synechocystis* at pH 8 in BG-11 media. Similarly, Nguyen (2015) found K_{Ci} values for *Synechocystis* ranging from 0.085 to 0.096 mM (1.02 to 1.15 $mgC_i\ L^{-1}$), depending on pH. In these experiments, cultures were grown in BG-11 medium with NH_4NO_3 instead of NO_3^- and augmented with different concentrations of $NaHCO_3$ and pH controlled with CO_2 gas addition. These low K_{Ci} values indicate that *Synechocystis* is adept at scavenging low levels of C_i. Anecdotally, in the benchtop photobioreactor or FMT photobioreactor I used, if the CO_2 supply was stopped, I observed that the pH climbed to as high as 12 (98% of C_i is CO_3^{2-}), indicative of *Synechocystis* growing on very low levels of C_i.

In the work I present in this dissertation, cultures were all grown on standard BG-11, and, therefore, as *Synechocystis* grew, alkalinity was generated and raised the pH of the solution. I delivered C_i to the system by bubbling air, CO_2, or a mixture through the culture, and as CO_2 dissolved, it lowered the pH. Once a culture was established,

provided that the pH is maintained below 10.3 with dissolving CO_2, sufficient C_i was in the system. I do not report any growth rates with pH higher than 9.

For the benchtop photobioreactor described in Chapter 2, I bubbled air at a set flow rate and adjusted the CO_2 content of the air to maintain the pH. For the FMT photobioreactor described in Chapters 3 and 5, I bubbled air in the reactor for mixing, and pure CO_2 was sparged in the reactor when a high pH set point was reached. Similarly, in Chapters 6 and 7, the FMT was sparged with pure CO_2, but mixing was achieved from a mechanical mixer rather than air. In all cases, C_i was sufficient and did not limit growth.

1.6. Nitrogen kinetics

Accounting for roughly 12.5% of *Synechocystis* biomass by weight (Kim et al., 2010), nitrogen (N) is the second largest input required for cell growth. Nitrogen is an important part of proteins, nucleic acids, and several other cell constituents (Madigan and Martinko, 2006). Most microalgae can utilize common forms of N, such as ammonium, nitrate, urea, and amino acids. The N preference and ability to use each N species varies with the microalgae species (Podevin et al., 2015). Ammonium is the most commonly preferred N species among microalgae (including *Synechocystis*), since it takes less energy for incorporation into biomass and is used directly (nitrate must be reduced to ammonia, and urea and amino acids are hydrolyzed to ammonia before they can be used) (Perez-Garcia et al., 2011).

Although ammonium is preferred by *Synechocystis*, the growth media used in this dissertation is BG-11, which, as described by Rippka et al. (1979), contains 246 mg NO_3-N L^{-1} as the primary nitrogen source. This is sufficient to grow approximately 2.0 g L^{-1} of biomass, and, therefore, N was in substantial excess for all experiments reported. At the levels I used, toxicity from nitrate is irrelevant, and nitrate can be autoclaved without losing any to volatilization. This growth medium was, therefore, efficient for precluding growth limitation from nitrogen. I note that ammonium could introduce problems from toxicity, volatility, and loss of alkalinity, but I did not use ammonium.

The effect on pH by microalgae growth can be easily represented by balancing a microalgae growth equation using the available N source (the cell composition was approximated from Kim et al. (2010) as $C_5H_8O_2N$). Since I used only nitrate, I show its reaction:

$$5CO_2 + 4.5\,H_2O + NO_3^- \rightarrow C_5H_8O_2N + 7.25\,O_2 + OH^- \qquad \text{Equation 1.2}$$

For each mole of nitrate (NO_3^-) consumed, a mol of hydroxide ions is produced. This production of alkalinity has a large impact on pH and consequently on the mass transfer of C_i, as discussed in section 1.5. I supplied CO_2 to counteract the pH increase from uptake and reduction of nitrate.

1.7. Community Considerations

Except for producing *niche* high-value products in small quantities, growing axenic cultures of microalgae is not practical. For this reason, it is important to understand that microalgal cultivation involves a community of microorganisms having a variety of functions and interactions. I classify these microbiological "neighbors" into the following categories: heterotrophic bacteria, viruses (cyanophages and algae viruses), and grazers (protozoans and zooplankton). These neighbors can enter the system because they were in the system previously, through the air, or through the growth medium (Wang et al., 2013). Pathogens (some bacteria and viruses) and predators (grazers) are recognized as one of the largest challenges to the stability of scaled-up microalgae systems (DOE, 2010).

All microalgae produce and excrete soluble microbial products (SMP) during growth and decay (Bratbak and Thingstad, 1985). The makeup of SMP is difficult to characterize, as they are comprised of many proteins, neutral and charged polysaccharides, nucleic acids, lipids, and small molecules (Fogg, 1983; Henderson et al., 2008). From the perspective of microalgal productivity, SMP do not contribute to valuable output. However, much of the SMP is biodegradable (Rittmann et al., 1987), and, therefore, fosters the growth of heterotrophic bacteria. In natural systems, microalgae are accompanied by heterotrophic bacteria with a wide range of phylogenetic diversity (Berg et al., 2009).

The impact heterotrophic bacteria have on microalgal growth is often benign. Le Chevanton et al. (2013) did a screening of 48 heterotrophic bacteria co-cultured with microalgae *Dunaliella* and found 2 of them to marginally improve growth, the remaining decreased growth by up to 35% with most showing minimal change to growth. We have performed similar experiments in our research group with similar results (Zevin, 2015).

Heterotrophic bacteria have been attributed with remineralizing organic C to C_i, making other nutrients bioavailable to microalgae, reducing oxygen concentrations, and competing for nutrients (Zevin, 2015).

Some species of bacteria, called phytoplankton-lytic bacteria, can strongly inhibit (up to 90%) the growth of microalgae (Wang et al., 2013). These bacteria are capable of lysing algal cells by either direct cell-to-cell contact or through the production of algicidal substances (Shunyu et al., 2006). Some phytoplankton-lytic bacteria become active due to quorum sensing (high density of the microalgae) or nutrient depletion (Zhou et al., 2011). While most phytoplankton-lytic bacteria have wide host ranges, some have relatively narrow host ranges (Rashidan and Bird, 2001). Relatively little is known about phytoplankton-lytic bacteria, including their abundance and the mechanisms of attack.

Cyanophages and algae viruses (collectively referred to as viruses) appear in abundance in natural ecosystems, typically in number concentrations orders of magnitude higher than their hosts (Dwellon and Parry, 2008). Algae viruses are believed to have narrow host ranges, meaning that a certain virus can only infect an algae species and close relatives whereas cyanophages typically have broader host ranges (Suttle, 2000; Xia et al., 2013). Because microalgal cultures often are grown to be dense monocultures, they are particularly susceptible to infection from viruses. Viruses reproduce by two mechanisms that depend on the host: a lytic cycle in which the virus infects the host, immediately begins to replicate, and is released by cell lysis; and lysogenic, in which the virus inserts its DNA in stable association with the host DNA, where it is housed for an indefinite amount of time until an environmental trigger causes the virus to be produced and cell lyse (Suttle, 2000). Both types of viruses show high diversity, and the variability in lytic cycles and triggers makes it difficult to estimate virus caused cell mortality (Suttle, 2005). Viruses are sensitive to ultraviolet light, including

from solar radiation (Suttle, 2000); therefore, high levels of light penetration would help minimize impacts from viruses. Despite the obvious potential for virus related impact to microalgae cultures, to my knowledge, no one has published work on virus prospecting in photobioreactor systems.

Microalgae grazers (herbivorous protozoa and zooplankton) are infamous for reducing microalgae productivity to very low levels in just a few days through predation (Park et al., 2011). Protozoa typically are more of a problem for cyanobacteria (eukaryotic algae are too big for protozoa), and zooplankton are a larger risk for eukaryotic algae. Although protozoa can show higher growth rates, zooplankton have other growth advantages including leaving eggs that can be difficult to remove from microalgae systems (Montemezzani et al., 2015). Figure 1.2 displays an image of a ciliate protozoan found in one of my bench-top PBR *Synechocystis* cultures. In natural ecosystems, grazer populations are kept in check by predation from higher organisms that are absent from microalgae cultivation systems (Montemezzani et al., 2015). Grazers are thought to be the main cause of culture crashes in microalgae cultivation systems (Wang et al., 2013).

Many strategies have been proposed for combatting grazers, including chemical, physical, and biological methods (reviewed by Montemezzani et al. (2015)). Ideally the microalgae system needs to prevent grazers, not react to them, and controls should not require significant additional cost. While several control strategies have shown some level of effectiveness, preventing gazer related crashes could be considered the "million-dollar discovery to microalgae cultivation."

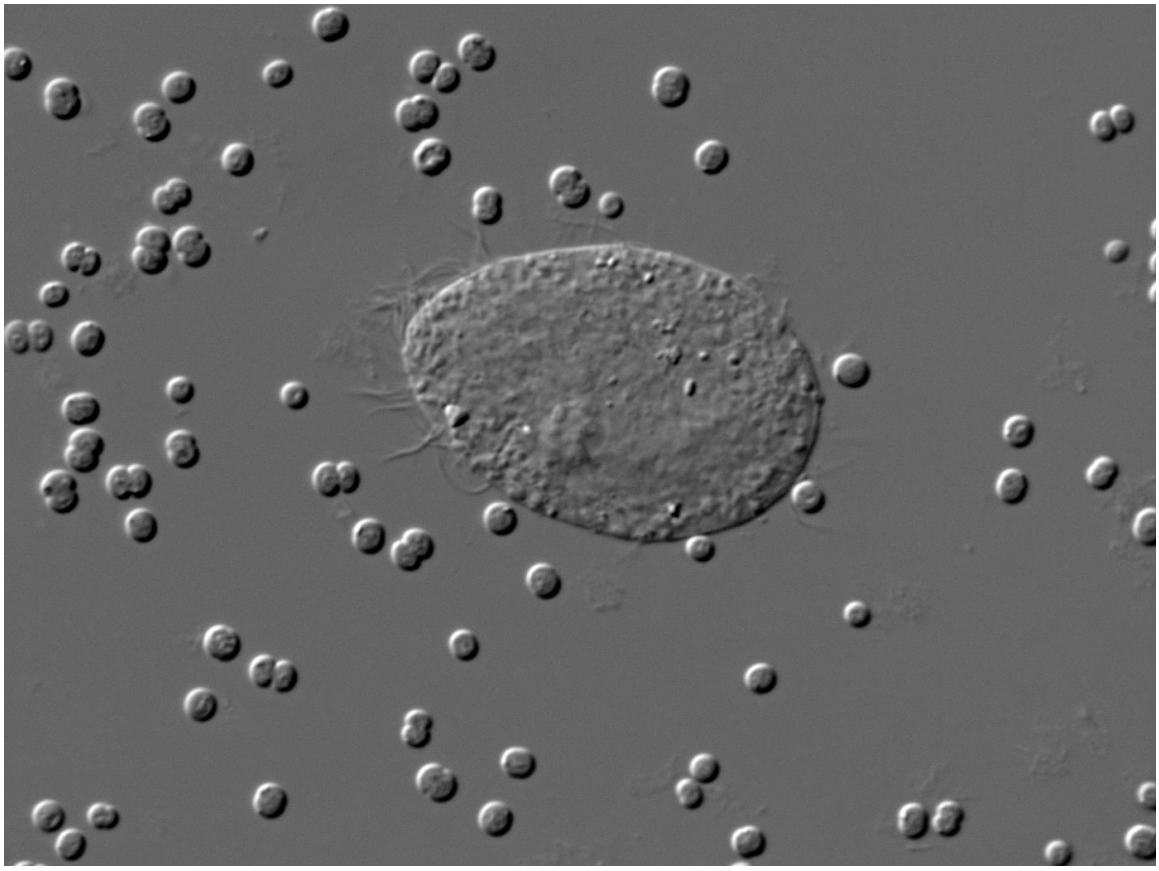

Figure 1.2: Light microscopy image of a *Synechocystis* culture grown in a benchtop PBR showing the presence of a ciliate. Image courtesy of Ricardo Reyes and Robert Robertson, 2013

During my experimental work for this dissertation, my main means for minimizing deleterious effects from the microbial community was to start with pure *Synechocystis* and keep everything as clean as possible. This involved autoclaving flasks for seed cultures, BG-11 growth media, the FMT photobioreactor, and all air and liquid tubing; running all air through a bacterial air vent; flaming the inoculation loop; and inoculating flasks or the FMT from a pure *Synechocystis* plate under a disinfected positive pressure laminar flow hood. Any exposure to the ambient lab air (which would happen, for example, during the changing of media bottles during continuous FMT operation), however, had the possibility to introduce foreign microbes. It is, therefore,

my assumption that the experiments performed in the FMT were not axenic. I have no evidence of deleterious effects from the community, but I also have no direct proof.

The benchtop photobioreactor used in Chapter 2 was too large to autoclave and was therefore only disinfected with bleach. Additionally, for feasibility issues, the BG-11 growth medium was not autoclaved. This may have introduced different levels of bacteria other than *Synechocystis*, depending on the operating conditions and random chance; the effects of heterotrophs on P uptake is a main consideration in the work presented in Chapter 2.

2. THE ROLE OF HETEROTROPHIC BACTERIA IN ASSESSING PHOSPHORUS STRESS TO *SYNECHOCYSTIS* SP. PCC 6803

2.1. Abstract

Microalgae biofuel production, a possible source of carbon-neutral energy, requires phosphorus (P), a limited resource. This study investigates the relationship between specific growth rate of the cyanobacterium *Synechocystis* sp. PCC 6803 and P availability. It has been previously suggested, and I show here, that P-limited growth kinetics are well represented by a quota-type model with a single pool of intracellular P. I also demonstrate that the presence of heterotrophic bacteria plays a large role in understanding these kinetics, because the culture's intracellular P content depends on the level of heterotrophic bacteria. Using batch-growth experiments containing up to a 0.07 biovolume ratio of heterotrophic bacteria to *Synechocystis*, I found that *Synechocystis* could grow with intracellular P content down to approximately 0.5 mg P g dry weight^{-1} biomass, while heterotrophic bacteria maintained roughly 20 mg P g dry weight^{-1}. Thus, a small fraction of heterotrophic bacteria in a microalgal culture can dramatically increase the apparent content of P in the biomass, which affects how to assess P-stress to a P-limited culture.

2.2. Introduction

As population densities and the standard of living increase across the globe, the need for energy sources with low environmental impact becomes more crucial to a sustainable future (Lewis, 2007). One technical strategy under investigation uses microalgae (single-celled eukaryotic algae and cyanobacteria) for biofuel production (Rittmann, 2008). These microorganisms have the ability to grow with sunlight, carbon dioxide, nutrients (primarily nitrogen (N) and phosphorus (P)), and water. Sunlight, carbon dioxide, and water are readily available in many regions, N can be fixed from atmospheric nitrogen gas, but P has no similar renewable source. Instead, P fertilizer is primarily mined as phosphate rock, and some data suggest that readily available, low-cost deposits will be depleted in a few decades (Cordell et al., 2012). Addition of biofuel production from microalgae or plants will exacerbate the demand for P. Clearly, efficient use and recovery of P will become more important in all sectors that require P inputs.

The efficient use of P in microalgae cultivation requires understanding of the relationships between P and microalgal growth, something that is not sufficiently documented. For example, the P content of phytoplankton dry weight is reported to be as low as 2 mg P g dry weight biomass $(DW)^{-1}$ and greater than 30 mgP gDW^{-1}, depending on environmental conditions, culture history, polyphosphate accumulation, and surface adsorption (Reynolds, 2006; Sañudo-Wilhelmy et al., 2004). Attempting to capture the interplay of these different P-pools has led to modeling approaches that include several pools of biomass P (Fuhs, 1969; John and Flynn, 2000; Yao et al., 2011). Additionally, most microalgal cultivation systems are not operated axenically, and, therefore, coexisting heterotrophic bacteria compete for P resources (Danger et al., 2007; Wang et al., 2013).

It has been well established that microalgae are capable of growth with soluble P depleted as long as they have intracellular stores of P available (Droop, 1973; John and Flynn, 2000). In this study, I investigated P-limited growth kinetics of the representative cyanobacterium *Synechocystis* sp. PCC6803 (simply *Synechocystis* from here); in agreement with the understanding of the role of intracellular P, *Synechocystis* continued to grow in batch culture well after soluble P had been depleted. Additionally and as suggested by John and Flynn (2000), a single intracellular-P pool was sufficient to model P-limited growth kinetics of a batch culture; I quantify the minimum size of this intracellular-P pool for *Synechocystis*. I expand on this understanding by adding the effect of the P imbedded in heterotrophic bacteria, which does not contribute to photosynthetic growth. Using this expanded model, I am able to explain different results I observed in repeated batch-growth experiments.

2.3. Materials and Methods

2.3.1. *Synechocystis* Growth Conditions

All results are presented from a bench-top photobioreactor (PBR) operated as described below. The bench-top PBR was inoculated from *Synechocystis* seed culture grown in 1-L Erlenmeyer flasks. The flasks were inoculated from plates, fed with ambient air filtered through a 0.2-μm membrane bacterial air vent (Pall Corporation, Ann Arbor, MI) at approximately 0.1 L min^{-1}, and illuminated continuously with 54-W fluorescent lamps (Hydrofarm, Inc., Petaluma, CA) at approximately 300 μmol m^{-2} s^{-1} incident Photosynthetically Active Radiation (PAR, light frequency 400 - 700nm) from one side. The top of the flask was plugged with cheesecloth, and a pipet passed through the center of the cloth and extended to the base of the flask. Filtered air was pumped into the flask through the pipet, bubbled through the culture, and exited through the cheese cloth. Seed cultures were grown on standard BG-11 medium (Rippka et al., 1979) containing 247 mgN L^{-1} and 5.4 mgP L^{-1} and maintained at 25-30°C. Flasks and growth media were autoclaved before use. Seed culture was ready for transfer to the bench-top PBR when it reached a dry weight concentration of approximately 900 mg L^{-1}.

2.3.2. Bench-top PBR

The bench-top PBR and its operation were described by Kim et al. (2010), although I made some changes that are noted here. Briefly, the PBR was a vertical flat-plate design measuring 55.9 cm wide, 5.1 cm deep, and 61.0 cm tall, and maintained with a liquid volume of approximately 14.5 L. The culture was grown with continuous illumination at approximately 120 μmol m^{-2} s^{-1} of PAR from each side. A thermal jacket maintained the reactor temperature at 30°C, and gas was delivered at a constant 0.3 L min^{-1} through a 15.24 cm long 1.27 cm diameter fine bubble air diffuser (Top Fin®) at the

bottom off-center of the reactor. The carbon dioxide concentration in the gas was adjusted to maintain a culture pH of 7 to 9. The liquid-circulation impellers used by Kim et al. (2010) were removed and replaced by a compact digital mixer (Cole-Parmer, Vernon Hills, IL) set at 1000 rpm and placed opposite the diffuser to achieve a circular mixing pattern. I inoculated the bench-top PBR with approximately 1.5L of seed culture (as described above) and added un-autoclaved BG-11 medium to bring the total liquid volume to 14.5 L. This initial biomass concentration of roughly 90 mg L^{-1} minimized light shock during inoculation.

I conducted batch experiments with 4 different P concentrations ranging from 0.65 to 1.35 mgP L^{-1}. Due to continuous sparging and medium supply, the PBR was not maintained axenic. To alter the BG-11 recipe for lower P concentrations, I added less K_2HPO_4 compared with normal BG-11 (i.e., for the experiment with 1.35 mgP L^{-1} a total of 7.6 mg L^{-1} K_2HPO_4 was added instead of 30.5 mg L^{-1}). The *Synechocystis* cultures for each batch experiment with different concentrations of P were subjected to different conditions prior to the reported batch growth to induce different quantities of heterotrophic bacteria. For the experiment with 0.65 mgP L^{-1}, the culture was grown in a sequencing batch mode for three days: The reactor was initially inoculated with normal BG-11 and was diluted to a DW of approximately 315 mg L^{-1} each day, with BG-11 containing 0 mgP L^{-1} until the final dilution brought P to 0.65 mgP L^{-1}, which is the condition that I report. The experiment with 0.97 mgP L^{-1} was batch grown directly after inoculation from a flask culture, and the reported data period started once the biomass concentration reached 330 mg L^{-1}. Following the final data point of the experiment with 0.97 mgP L^{-1}, the reactor was diluted with fresh medium to start the batch growth experiment at 1.27 mgP L^{-1}, where the reported data start immediately after the dilution. Finally, prior to the reported data period of the experiment with 1.35 mgP L^{-1}, the reactor

was operated as a chemostat for 3 days at a DW of approximately 330 mg L^{-1} and feeding with 1.35 mgP L^{-1} in BG-11. After the 3-day period, the reactor was operated in batch growth, and the reported data collection began.

2.3.3. Sampling and Analytical Methods

I monitored the performance of the PBR by analyzing liquid samples for pH (which was controlled to within the range of 7 to 9 by adjusting carbon dioxide concentration in the sparging gas), total and soluble P, and biomass DW. The results, presented in supplement information Figure S2.1, illustrate that the PBR performance was stable during the experiments. pH was measured using an Orion 4-StarTM Plus Benchtop pH/ISE Meter (Thermo Scientific, Waltham, MA). Total phosphorus was measured using Hach Phosphorus TNTplus, UHR Reactive, and Total kit (Hach Company, Lowland, CO), and soluble phosphate was measured after filtering culture through a 0.45-µm Supor® Membrane Disc Filter (Pall Corporation, Ann Arbor, MI) and measured using PhosVer® 3 Phosphate Reagent (Hach Company, Lowland, CO) orthophosphate colorimetric test. The DW concentration was determined by drying a 0.7-µm glass microfiber filter (Whatman®, Buckinghamshire, UK) at 60°C overnight, weighing it, filtering 10 ml of culture through the filter, drying the filter overnight again, and taking the difference in the dry mass before and after filtration.

Biovolume was estimated by storing a culture sample in 4% formalin at 4°C and imaging the samples using an Axioskop Microscope (Carl Zeiss Microscopy, LLC, Thornwood, NY) at 100x magnification. Heterotrophic bacteria and *Synechocystis* were easily distinguishable. *Synechocystis* are cocci (approximately 3-µm diameter) with a typical biovolume of 14 μm^3 per cell. Heterotrophic bacteria are rod shaped (approximately 4 µm length and 0.5 µm width) with a typical biovolume of 0.75 μm^3 per

cell. I took 8 random images and counted the number of rod-shaped heterotrophic bacteria and sphere-shaped *Synechocystis*. Each image had between 24 and 61 cells. The biovolume ratio of heterotrophic bacteria was the total biovolume of heterotrophic bacteria (cell count multiplied by 0.75 μm^3) divided by the total biovolume of all bacteria (volume of heterotrophic bacteria plus *Synechocystis* count multiplied by 14 μm^3). The final reported value was the average biovolume ratio of the 8 images counted. I assumed that the biovolume ratio was approximately equal to the mass ratio. The biovolume estimation was conducted on the final sample of the batch experiments to determine the approximate heterotrophic content of the PBR.

2.4. Theory / Calculations

The relationship between P and *Synechocystis* growth was modeled using a quota-type model based on a single intracellular P-pool (P_{int}; mgP gDW^{-1}) as suggested by John and Flynn (2000):

$$\mu = \mu_{LI}\left(\frac{P_{int}-P_{min}}{P_{int}-P_{min}+K_P}\right) \qquad \text{Equation 2.1}$$

where μ_{LI} is the μ without P-limitation (light-limited μ; day^{-1}), P_{min} is the threshold of P_{int} (below which the cell cannot grow; mgP gDW^{-1}), and K_P is the half-maximum concentration for P_{int} (mgP gDW^{-1}). Because my cultures were not axenic (containing up to a 0.07 biovolume ratio of heterotrophic bacteria), P_{int} was determined by excluding the P contained in the heterotrophic bacteria P_{het} (mgP L^{-1}):

$$P_{int} = \frac{P_{tot}-P_{sol}-P_{het}}{DW} \qquad \text{Equation 2.2}$$

where P_{tot} is the total P in the culture (mgP L^{-1}) and P_{sol} is the soluble P (mgP L^{-1}). In this study, I found that biomass contained between 12 and 16 mgP gDW^{-1} when subjected to conditions with no limitation by soluble P. Thus, when P_{int} was below 10 mgP gDW^{-1}, all soluble P had been depleted, which was the case for all batch experiments reported here. At all reported time points, soluble P values were measured to be < 0.03 mgP L^{-1}. Because the method detection limit was 0.02 mgP L^{-1}, the soluble-P concentrations were not reliably distinguishable from zero. For this reason, the modeled curves assume P_{sol} = 0 mgP L^{-1}.

During batch cultivation, the biomass concentration was continually increasing; therefore, light attenuation also increased with time, making the average internal LI decrease (LI_{ave}; µmol m^{-2} d^{-1}). I computed the average internal light intensity (LI_{ave}) using the spatially integrated Beer-Lambert's law. Equation 2.3 is the Beer-Lambert Law, and Equation 2.4 is its spatially integrated form:

$$LI = LI_0 e^{-\varepsilon X d} \quad \text{Equation 2.3}$$

$$LI_{ave} = \frac{LI_0 * (1 - e^{-\varepsilon X w})}{\varepsilon X w} \quad \text{Equation 2.4}$$

where LI_o is the incident light intensity (μmol m^{-2} s^{-1}; 240 for the bench-top PBR), ε is the Beer-Lambert constant (m^2 g^{-1}), X is the biomass concentration (mg L^{-1}), d is the depth in the culture (m), and w is the width of the reactor (m; 0.051 for the bench-top PBR) (Kim et al., 2010). I estimated ε by filling a 1-L beaker with culture of a known density (X) and measuring the light intensity at 11 different depths (0.5 cm apart) from a light source below the beaker using a LI-192 PAR sensor (LI-COR Biosciences, Lincoln, NE). The sum of the squares of the difference between the predicted light intensity using Equation 2.3 and measured data was minimized by finding an optimal ε. I did this on 3 reactor samples with biomass density between 330 and 340 mg L^{-1}. This gave a mean ε of 0.251 m^2 g^{-1}, with a standard deviation of 0.023 m^2 g^{-1} and a standard error of less than 6 μmol m^{-2}-s^{-1} for each of the 3 attenuation curves. The mean value is consistent with the value of 0.255 m^2 g^{-1} found by Kim et al. (2010). LI_o was determined by taking a spatially averaged reading of the inside surface of the PBR using a LI-190 PAR sensor (LI-COR Biosciences, Lincoln, NE).

Because my LI_{ave} was relatively small in all experimental conditions (less than 100 μmol m^{-2} d^{-1}), this falls into a region of the light-response curve where μ_{LI} follows a linear relationship with LI_{ave} (Jassby and Platt, 1976):

$$\mu_{LI} = \alpha LI_{ave} \quad \text{Equation 2.5}$$

where α is the relationship between growth and light (m^2 s μmol^{-1} d^{-1}). Assuming a multiplicative relationship for light and P, I used the following overall dual-limitation formula for specific growth rate:

$$\mu = \alpha LI_{ave}\left(\frac{P_{int}-P_{min}}{P_{int}-P_{min}+K_P}\right)$$ Equation 2.6

Using Equations 2.2, 2.4, and 2.6, I modeled a time-series growth curve that I fit to each batch experiment. Each modeled batch experiment was assumed to use the same α, P_{min}, and K_p, but each had a unique P_{het}. I simultaneously fit the seven values by minimizing the sum of squares between the modeled and measured X values (Hastie et al., 2009).

I also compared the measured biovolume ratio of heterotrophic bacteria to the P_{het} best-fit parameter from each batch experiment by assuming that the heterotrophic bacteria had a set P content ($P_{min,het}$; mgP gDW^{-1}):

$$\frac{P_{het}}{P_{tot}} = \frac{P_{min,het}*X_{het}}{P_{min}+(P_{min,het}-P_{min})*X_{het}}$$ Equation 2.7

where X_{het} is the biovolume ratio of heterotrophic bacteria (heterotrophic biomass DW total biomass DW^{-1}). For $P_{min,het}$, I assume a typical stoichiometric P content for heterotrophic bacteria of 20 mgP gDW^{-1} (Bruce E. Rittmann and McCarty, 2001).

2.5. Results and Discussion

2.5.1. *Synechocystis* Batch-Growth Experiments

The biomass-growth results for the four P-limited batch experiments containing 0.65, 0.97, 1.27, and 1.35 mgP L^{-1} are plotted in Figure 2.1. Each curve is a typical light-limited growth curve that transitions at different points to a plateau, indicative of P-limited growth. For the entirety of these experiments, soluble P was depleted (i.e., < 0.03 mgP L^{-1}), but biomass growth was significant for over 6 days in the three cases with the most total P added originally (0.96, 1.27 and 1.35 mgP L^{-1}), and only one case (0.65 mgP L^{-1}) showed almost no growth. This continued growth in the batch experiments clearly supports the understanding that growth does not depend on soluble P, but rather on P_{int}. Because BG-11 contains an excess of nitrate nitrogen (N), the N:P ratio always was large.

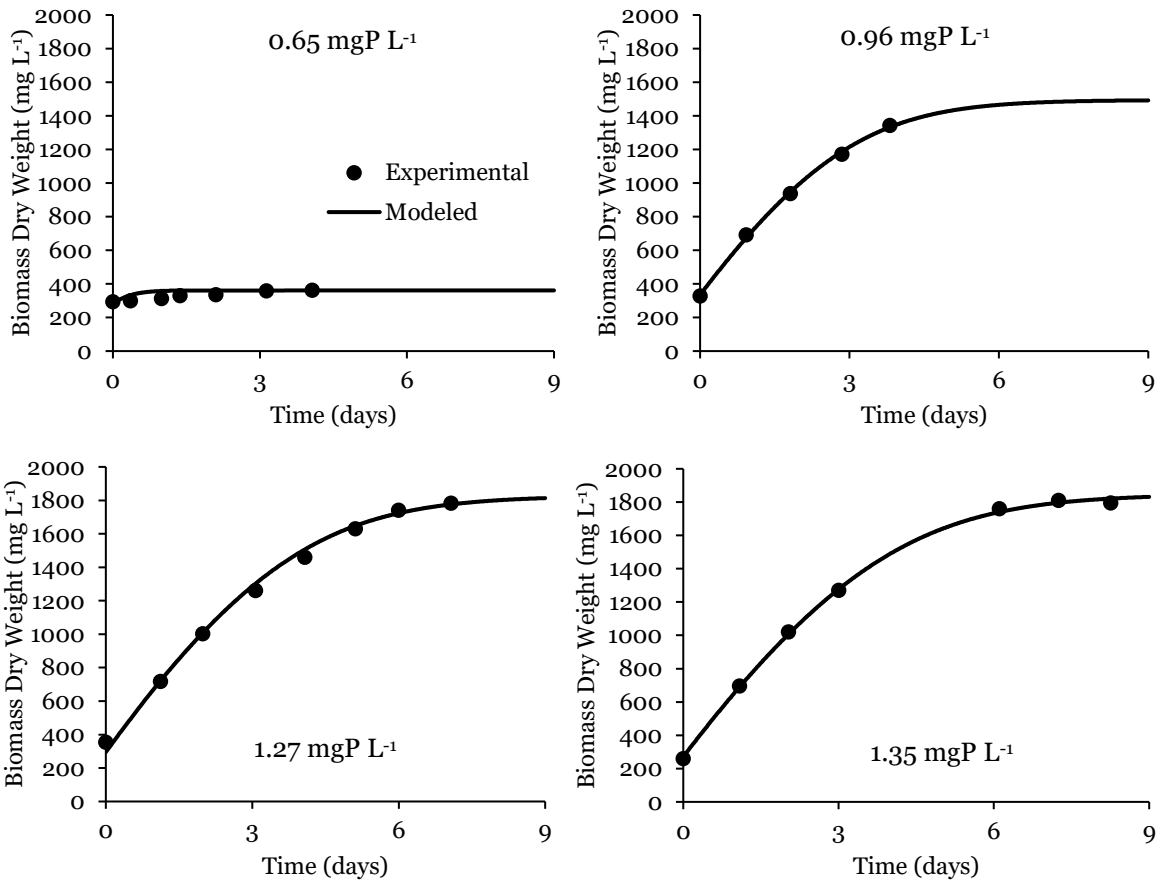

Figure 2.1: Time series for batch growth of four different P-limited *Synechocystis* cultures grown in a flat-panel PBR with a total incident light of 240 μmol m^{-2} s^{-1}. The total P in the system is listed in each plot (0.65, 0.96, 1.27, and 1.35 mgP L^{-1}), and soluble P was depleted (measured < 0.03 mgP L^{-1}) at all times. The modeled biomass utilized the dual-limitation model, Equations 2.2, 2.4, and 2.6 with parameters: α = 0.023 m^2 s μmol^{-1} d^{-1}, P_{min} = 0.48 mgP gDW^{-1}, K_p = 0.16 mgP gDW^{-1}, and P_{het} = 0.48, 0.25, 0.39, and 0.46 mgP L^{-1} for each of the four experiments respectively.

The lines in Figure 2.1 are for the quota-type model (Equations 2.2, 2.4, and 2.6) with best-fit modeling parameters α = 0.023 m^2 s μmol^{-1} d^{-1}, P_{min} = 0.48 mgP gDW^{-1}, and K_p = 0.16 mgP gDW^{-1}, and variable P_{het} as noted in the figure caption. The standard errors for the fits were 10.7, 6.5, 12.2, and 6.3 mgDW L^{-1} in order of ascending total P. As expected, P_{het} varied by experiment, being 0.48, 0.25, 0.39, and 0.46 mgP L^{-1} for each of the four experiments in ascending total P. These values are 74%, 26%, 34%, and 31% of the total P of each experiment. Thus, the heterotrophic bacteria contained a major portion of the total P, and, in general, cultures that had been in the PBR longer showed a higher P_{het}.

The very low P_{min} value for *Synechocystis*, 0.48 mgP gDW^{-1}, indicates that this cyanobacterium was able to function with a very small amount of P-containing compounds. The genome length of *Synechocystis* is 3,573,470 bp (Kaneko et al., 1996), each bp has 2 atoms of P, and the approximate mass of a cell is $1.53x10^{-12}$ g (Liu et al., 2010). From this, I calculated that a single copy of the genome accounts for 0.24 mgP gDW^{-1}. Therefore, when *Synechocystis* contains P at its P_{min} level, its DNA accounts for about one-half of P_{int}, which means that the remaining 0.24 mgP gDW^{-1} must encompass all the P in RNA, lipids, and any additional DNA (Yao et al., 2016).

The value of K_p also is very low (0.16 mgP gDW^{-1}), which underscores that the onset of P-stress can be very rapid when P_{int} approaches P_{min}. At 2 mgP gDW^{-1} (10x less P than the assumed content of heterotrophic bacteria), *Synechocystis* grows at greater than 90% of μ_{LI}, and at 1 mgP gDW^{-1} it still grows at a rate greater than 75% of μ_{LI}. However, a small decline to 0.5 mgP gDW^{-1} drops the specific growth rate to only 10% of μ_{LI}.

2.5.2. Measuring Heterotrophic Biovolume

To evaluate the P_{het} best-fit model parameter, I also counted cells on light microscopy images to directly quantify the heterotrophic bacteria. The biovolume ratios of heterotrophic bacteria I found at the final point of each experimental run were 3.8%, 0.25%, 0.69%, and 2.0% in order of ascending total P. These are plotted against the best-fit P_{het} normalized to total P for each experiment in Figure 2.2, as well as the curve generated using Equation 2.7. The measured values cluster around the model-predicted line, which supports the idea that heterotrophic bacteria were responsible for the relatively higher P_{int} associated with decreased growth rate in the batch experiments compared with "the purer" experiments. While my method of determining the biovolume ratio had modest uncertainty (Standard Error of 0.069) and the actual P content of the heterotrophic bacteria could not be measured directly, my method of estimating P_{het} captured the trends of Figure 2.2, corroborating that heterotrophs became a major competitor to *Synechocystis* for P in P-stressed conditions, such as shown in Figure 2.1.

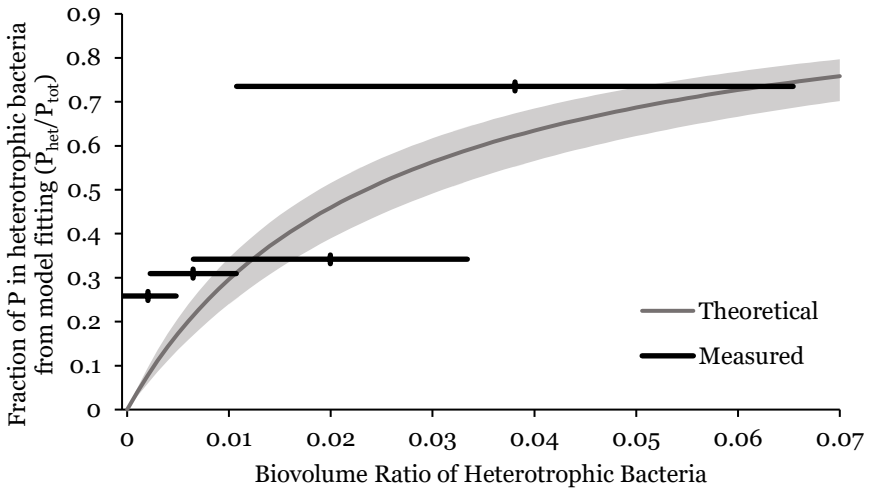

Figure 2.2: Biovolume ratio of heterotrophic bacteria to total biomass (including *Synechocystis*) as determined by cell counting, plotted against the fraction of total P in heterotrophic bacteria. The P in heterotrophic bacteria (P_{het}) is the best-fit modeling parameter for each plot in Figure 2.1 divided by the corresponding total P (P_{tot}). Biovolume was estimated at the final point of each experimental run. The width of the line represents the standard deviation of the 8 different light microscopy image counts and the center tick is the mean. The theoretical line utilizes Equation 2.7 and assumes that P_{min} for *Synechocystis* P_{min} is 0.48 mgP gDW^{-1}, while heterotrophic bacteria have a P content of 20 mgP gDW^{-1} ($P_{het,min}$). The surrounding band represents a range of 15-25 mgP gDW^{-1} for $P_{het,min}$.

The very low value of P_{min} for *Synechocystis* demonstrates a substantial opportunity for reducing the need for P input during biomass cultivation. For instance, *Synechocystis* grown with excess P accumulates 12 to 16 mgP gDW^{-1}, while the slowdown of the specific growth rate is only 10% at P_{int} > 2 mgP gDW^{-1}. However, this potential 80-fold savings can be confounded by the presence of heterotrophic bacteria, which maintain a high P content, such as 20 mgP gDW^{-1}. As shown in Figure 2.2, having only 2% of the biovolume in heterotrophic biomass and *Synechocystis* biomass at P_{min}, P_{het} accounts for half of the P in the culture, which decreases overall culture production of *Synechocystis* by half. Furthermore, predicting when P stress affects the phototroph depends sensitively on P_{het}, which is determined by the concentration of heterotrophic bacteria.

2.6. Conclusions

Synechocystis's specific growth rate in P-limited batch growth was well represented by quota-type kinetics based on intracellular P (P_{int}), not soluble P. The minimum P content of *Synechocystis* was 0.48 mgP gDW^{-1}, of which at least half was in DNA. Besides *Synechocystis*, however, heterotrophic bacteria could contain a large fraction of the culture's P (P_{het}; up to 74% of the total P in the reported experiments), since they contained larger amounts of intracellular P. By considering P_{het}, I was able to explain different outcomes in *Synechocystis* batch-growth experiments, and I highlight that the concentration of heterotrophic bacteria plays an important role in determining P-stress for microalgae.

2.7. Supplementary Material

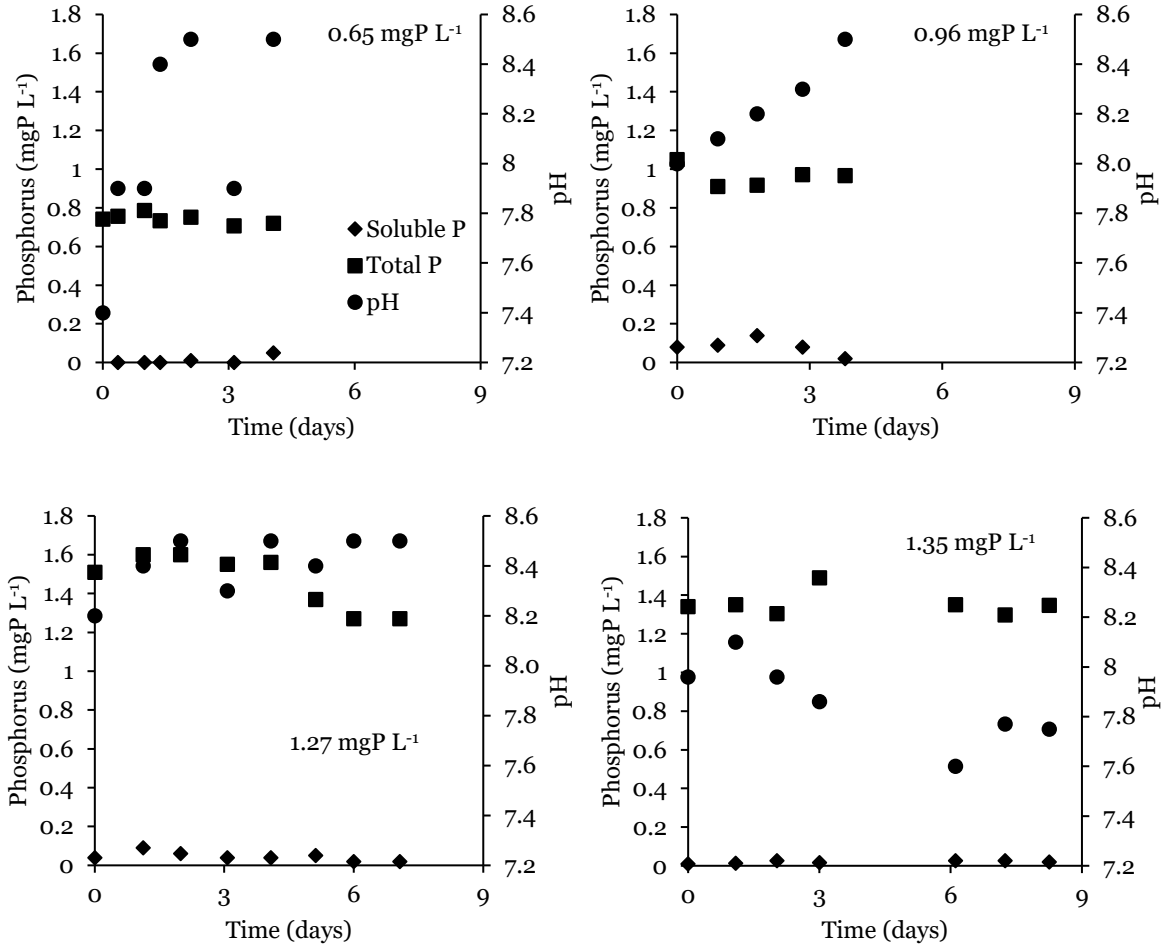

Figure S2.1: Time series soluble P, total P, and pH for the four batch experiments in Figure 2.1. The experiments are identified by their final total P concentration: ~ 0.65, 0.96, 1.27, and 1.35 mgP L^{-1} as labeled on the plots.

3. LIGHT ATTENUATION CHANGES WITH PHOTOACCLIMATION IN A CULTURE OF *SYNECHOCYSTIS* SP. PCC 6803

Published as (Straka and Rittmann, 2017)

3.1. Abstract

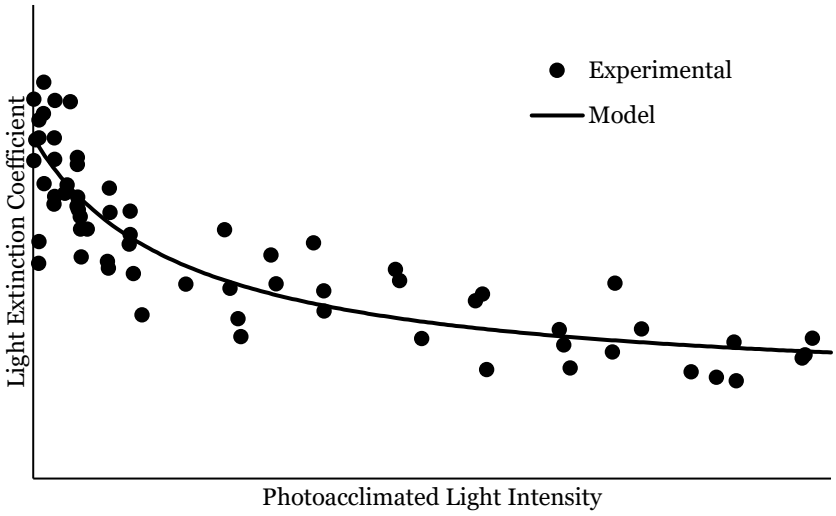

An inherent complication in the relationship between light intensity (LI) and microalgae growth rate is that light attenuates through a culture due to its absorption by biomass. While a biomass's specific extinction coefficient (ε describing how rapidly light attenuates) often is assumed to be a constant for a species for mathematical modeling, it is well documented that pigmentation and light absorption depend on growth conditions, particularly light intensity itself. In this study using *Synechocystis* sp. PCC 6803, I investigated the effect of LI on ε. Using cultures fully acclimated to the LI at which they were grown, I found that biomass grown at higher LI absorbed less light than biomass grown at lower LI; thus, ε was larger for lower LI. I quantify the relationship between ε and the acclimated LI and suggest that ε would be an appropriate metric for describing photoacclimation.

3.2. Introduction

Mathematical modeling of microalgal growth is a valuable tool for optimizing biomass productivity in engineered systems and understanding primary production in natural systems (Iwakuma and Yasuno, 1983). A growth-limiting factor that has received much attention is light, because its intensity varies naturally, and light is the energy source driving photosynthesis (Béchet et al., 2013). Unlike a growth-limiting nutrient, light attenuates through a microalgal culture, which means that the light intensity (LI) declines away from its source. Understanding light attenuation is important, because it controls the LI available to cells within the culture and because light attenuation is partly caused by light-energy absorption of the biomass (Cornet et al., 1995; Pottier et al., 2005).

Light attenuation is most often represented mathematically by the Beer-Lambert Equation, which utilizes an exponential function based on the light path (d, in m), biomass concentration (X, in mg L^{-1}), and an extinction coefficient (ε, in m^2 g^{-1}) to represent the light absorption of the microalgae culture (Béchet et al., 2013; Yun and Park, 2001):

$$LI = LI_0 \exp(-\varepsilon X d) \qquad \text{Equation 3.1}$$

where LI is the local light intensity (μmol m^{-2} s^{-1}), and LI_o is the incident light intensity (μmol m^{-2} s^{-1}). In practice, ε is empirically determined and accounts for the aggregate effect of light scattering and light absorption (Cornet et al., 1995). While in-depth analyses of the radiative properties of microalgae suggest that scattering is an important phenomenon in microalgae LI extinction, they also report that the vast majority (about 99.9%) of scattering occurs in the forward direction (Berberoglu et al., 2008; Berberoglu and Pilon, 2007; Heng et al., 2014; Privoznik et al., 1978). Forward-scattered light can

be absorbed by other biomass; thus, only back-scattered light at the light's entering surface and light scattered out of the edges of the reactor are truly lost to scattering.

Light absorption depends on the pigmentation of the biomass, while light scattering depends on cell morphology and surface properties (Kandilian et al., 2013). It is well established that microalgae change their pigmentation and cell morphology in response to different light conditions as a component of photoacclimation (Kandilian et al., 2013; MacIntyre et al., 2002; Talmy et al., 2013). Microalgae also change their pigmentation in response to adverse growth conditions, such as nutrient limitation, non-optimal salinity, or extreme LI (Mulders et al., 2014). However, the common practice in modeling light attenuation is to assume a constant ε for a given species of microalgae (Béchet et al., 2013; Bosma et al., 2007; Grobbelaar et al., 1990; Kim et al., 2010; Muller-Feuga et al., 2003). Although the phenomena of changing ε with growth conditions has not received much attention, past research with *Chlorella vulgaris* demonstrated that ε depended on culture biomass density (Béchet et al., 2015; Yun and Park, 2001).

A metric that has been used to identify the photoacclimation state in microalgae growth models is the ratio of chlorophyll-to-carbon (MacIntyre et al., 2002; Myers, 1946; Zonneveld, 1997). For most species, however, the biomass contains significant amounts of non-chlorophyll pigments, and the primary pigments in cyanobacteria are phycobilisomes, not chlorophylls (Akimoto et al., 2014; MacIntyre et al., 2002; Morel and Bricaud, 1981). For these reasons, chlorophyll content is not a good metric for absorbance or photoacclimation. Alternatively, I suggest that ε is a better metric than the chlorophyll-to-carbon ratio for identifying the photoacclimation state, as it accounts for the aggregate effect of all pigment and morphological changes.

In this study, I use the cyanobacterium *Synechocystis* sp. PCC6803 (simply *Synechocystis* from here) to test the hypothesis that the LI to which microalgae are

acclimated systematically affects its ability to absorb light. In particular, photoacclimation affects ε such that biomass grown at low LI has a higher ε than biomass grown at high LI. This finding also suggests that ε can be an appropriate parameter to represent photoacclimation.

3.3. Materials and Methods

Synechocystis was grown in a Photobioreactor FMT150 (Photon Systems Instruments, Drásov, Czech Republic; simply FMT from here) with nominal incident light settings from 0 to 6626 μmol m^{-2} s^{-1} of Photosynthetically Active Radiation (PAR), a liquid volume of 370 mL, and a fixed temperature of 30°C. The FMT is described in detail by Nedbal et al. (2008). I replaced the factory-supplied diffusor with an Aquarium Fine Bubble Air Stone (Top Fin®, Phoenix, AZ), and air was supplied by an EcoPlus® aquarium air pump at approximately 0.1 L min^{-1} (Sunlight Supply, Inc., Vancouver, WA) and filtered through a 0.2-μm membrane bacterial air vent (Pall Corporation, Ann Arbor, MI). The FMT took automatic readings of optical density at 735 nm (OD_{735}) and 680 nm (OD_{680}). The operating conditions utilized the Turbidostat Module, which added fresh growth medium using a peristaltic pump when the OD_{735} reached an upper set value, and it stopped delivering medium when it reached a lower set value. I set the OD_{735} range at 0.20 to 0.21. The pH was controlled using an MC122 pH Controller (Milwaukee Instruments, Rocky Mount, NC), which opened a solenoid valve (Milwaukee Instruments, Rocky Mount, NC) to bubble pure CO_2 into the reactor when the pH exceeded 8.5 maintaining a pH between 7.5 and 8.6. Growth medium was autoclaved standard BG-11 as described by Rippka et al. (1979). The FMT cultivation vessel was autoclaved and inoculated from a flask seed culture.

The FMT had nominal light settings ranging from 0 to 6626 μmol m^{-2} s^{-1} PAR. To determine the actual incident light intensities, I used a LI-190 PAR sensor (LI-COR Biosciences, Lincoln, NE) and measured the light entering the cultivation vessel directly behind a piece of glass placed where the inside wall of the FMT cultivation vessel would be. I measured 9 positions equally spaced over the irradiated area (Figure S3.1 in section 3.6) and at 23 different nominal light settings ranging from 0 to 3200 μmol m^{-2} s^{-1} PAR.

The LI was not uniform, with higher light intensity in the center and less intensity towards the top and bottom of the vessel (Figure S3.2). I computed an area-weighted average of the nine points to provide an average incident light reading at each of the light settings tested. The result was a calibration between the nominal FMT light setting (LI_{FMT}) to the actual average incident light intensity (LI_o): $LI_o = 2.06*(LI_{FMT}-81.2)^{0.826}$ (standard error = 8.86 μmol m^{-2} s^{-1}).

Because the biomass concentration was relatively dilute and the OD_{735} range within the FMT narrow, I used the average LI (LI_{ave}) as an approximation of the photoacclimated LI (LI_{acc}) of the culture. LI_{ave} was computed as an area integration of the Beer-Lambert Equation:

$$LI_{ave} = \frac{LI_0(1-\exp(-\varepsilon Xw))}{\varepsilon Xw} \qquad \text{Equation 3.2}$$

where w is the width of the bioreactor (0.024 m for the FMT).

I independently determined ε by taking a 20-ml culture sample and placing it in a 60-mm x 15-mm petri dish (VWR®, Radnor, PA) with a liquid depth of 9 mm. The sample was illuminated from underneath with a 54-W fluorescent lamp (Hydrofarm, Inc., Petaluma, CA), and the light intensity was measured above the sample using the LI-190 PAR sensor. The sample was then diluted and measured again. Once 5 different dilutions (100% sample, 80%, 60%, 40%, and 20%) and a water control were measured, the data were used to determine ε of the sample by fitting the X and LI data to the Beer-Lambert Equation (Equation 3.1), where d was 0.009 m, and LI_o was approximately 320 μmol m^{-2} s^{-1} (the reading for water) (Figure S3.3). Dry weight (X) was measured by taking a 0.7-μm glass microfiber filter (Whatman®, Buckinghamshire, UK) and drying it overnight at 60°C, weighing it, filtering 10 ml of culture through it, drying it at 60°C

overnight again, and subtracting the mass before from the mass after. During this study the biomass dry weight concentration was between 94-177 mg L^{-1}.

All ε values are reported for steady-state operating conditions, which I determined after OD_{680}/OD_{735} and growth (as determined by time between dilutions) were stable. Due to turbidostat operation, the dilution rate was tied to growth rate, which was between 1.5 and 2.5 d^{-1} for $LI_{ave} > 125$ μmol m^{-2} s^{-1} and as low as 0.25 d^{-1} at $LI_{ave} = 13$ μmol m^{-2} s^{-1}. Light acclimation, however, was independent of dilution rate. When the previous LI was lower than the LI being considered, steady-state typically was achieved 2 to 3 days after changing the light, and it took about 1 day when the previous LI was higher. Each measured ε, along with the corresponding X and LI_o, was used to compute LI_{ave} for that point using Equation 3.2.

The reactor vessel periodically had visible biofilm and floc formation, particularly at higher LI_{ave}. When this occurred, I removed the culture from the reactor vessel, scrubbed the vessel with bleach and Alconox® cleaner (Alconox, Inc., White Plains, NY), rinsed it thoroughly, filtered the culture through sterile cheese cloth, and returned the culture to the vessel. I discarded all data collected when the FMT contained visible biofilms or flocculated biomass.

All curve fittings, including the ε determinations described above, and all best-fit parameters in Equation 3.3 (below) were obtained by least-squares fitting between the experimental and modeled results, and standard errors were calculated (Hastie et al., 2009). The plot of residuals was generated by subtracting ε predicted from Equation 3.3 from the measured ε.

3.4. Results and Discussion

Measured ε values for LI_{ave} (assumed to be equal to the photoacclimated LI; LI_{acc}) with dilute biomass concentrations are displayed in Figure 3.1, which clearly shows that ε was not constant. Instead, ε declined from its maximum (ε_{max} = ~0.18 $m^2\ g^{-1}$) at very low LI_{acc} and stabilized at a minimum level of approximately 0.045 $m^2\ g^{-1}$ (ε_{min}) as LI_{acc} becomes very large. I mathematically represent the systematic changes in ε using:

$$\varepsilon = \frac{(\varepsilon_{max}-\varepsilon_{min})k_\varepsilon}{k_\varepsilon+LI_{acc}} + \varepsilon_{min} \qquad \text{Equation 3.3}$$

where k_ε is the half maximum light absorption LI_{acc} (μmol $m^{-2}\ s^{-1}$), ε_{max} is the measured ε value at the smallest LI_{acc} able to sustain net positive growth, and ε_{min} is extrapolated from the ε trend as LI_{acc} approaches infinity. The best-fit values for the experimental data are summarized in Table 3.1 and were used to produce the model line in Figure 3.1.

Table 3.1: Best-Fit Parameters for the Light-Dependent Beer-Lambert Extinction Coefficient (Equation 3.3)

Parameter	Description	value	units
ε_{max}	ε for biomass photoacclimated to the lowest possible LI_{acc}	0.18	$m^2\ g^{-1}$
ε_{min}	ε for biomass without any light absorption, only scattering	0.045	$m^2\ g^{-1}$
k_ε	Half-maximum-absorption LI	380	μmol $m^{-2}\ s^{-1}$

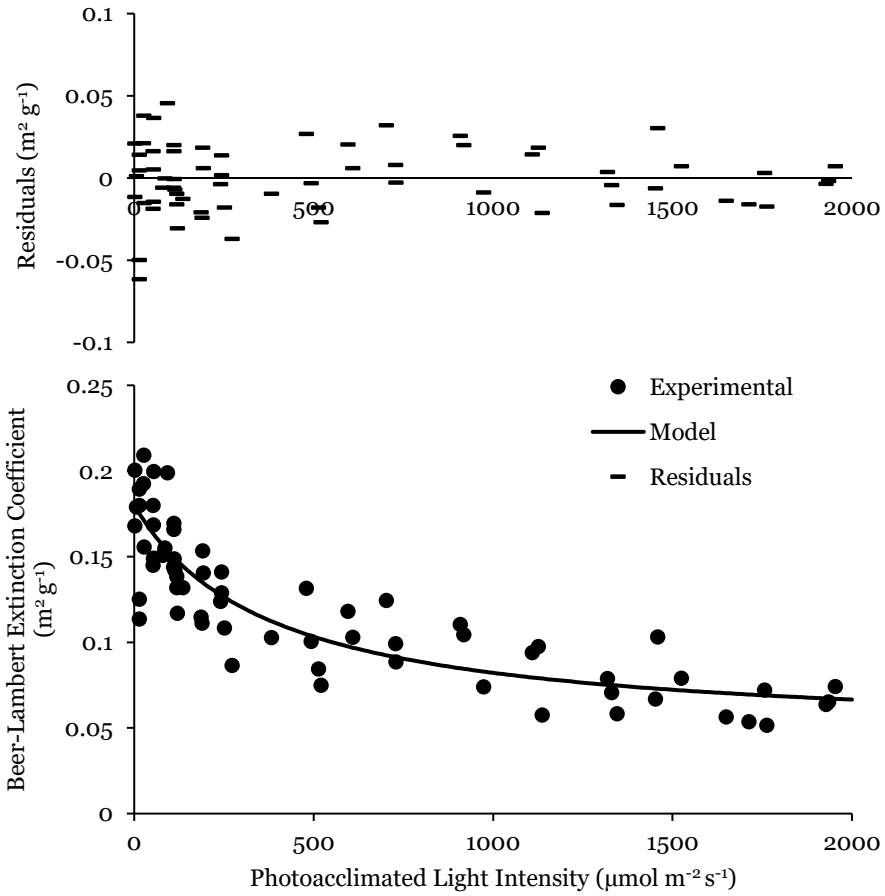

Figure 3.1: Beer-Lambert extinction coefficient (ε; lower plot) as a function of photoacclimated light intensity (LI_{acc}) determined with steady-state dilute cultures of *Synechocystis* in an FMT photobioreactor at different average internal light intensities (assumed to be LI_{acc}). The data are modeled (lower plot) using Equation 3.3 with the parameters in Table 3.1 (standard error for ε = 0.0070 $m^2\ g^{-1}$), and residuals are presented in the upper plot.

The value of ε was most sensitive to LI_{acc} in the region of lower LI_{acc}, where ε increased steadily as LI_{acc} declined. The higher ε at low LI_{acc} also was qualitatively apparent by the culture appearing greener than cultures grown at higher LI. This trend supports that *Synechocystis* maximized light absorption when light was scarce by increasing light-absorbing pigments. At the other end of the LI_{acc} range, the ε value changed proportionally less as LI_{acc} increased to 2000 µmol $m^{-2}\ s^{-1}$. This trend is similar to chlorophyll measurements taken for *Chlorella* (MacIntyre et al., 2002; Myers, 1946)

and for *Synechocystis* (Stramski and Morel, 1990) (although quantitatively quite different for *Synechocystis*, as chlorophyll is only one component of photoacclimation). The residuals plot of Figure 3.1 demonstrates that variability of the measured ε was random throughout the range of LI_{acc} tested, although the magnitude of the variability was slightly larger for lower LI_{acc}. This trend is expected, because ε is more sensitive to changes in LI at lower LI.

Another metric that correlates to pigment content is the ratio of OD_{680}, which accounts for absorption of red light, to OD_{735}, which is beyond the spectrum of light absorbed for photosynthesis and therefore a measure of turbidity or light scattering. An increase in OD_{680}/OD_{735} signifies an increase in light-absorbing pigment. Comparing OD_{680}/OD_{735} to ε in Figure 3.2 makes it apparent that they increase linearly with each other at a slope of approximately 0.16 ε / (OD_{680}/OD_{735}).

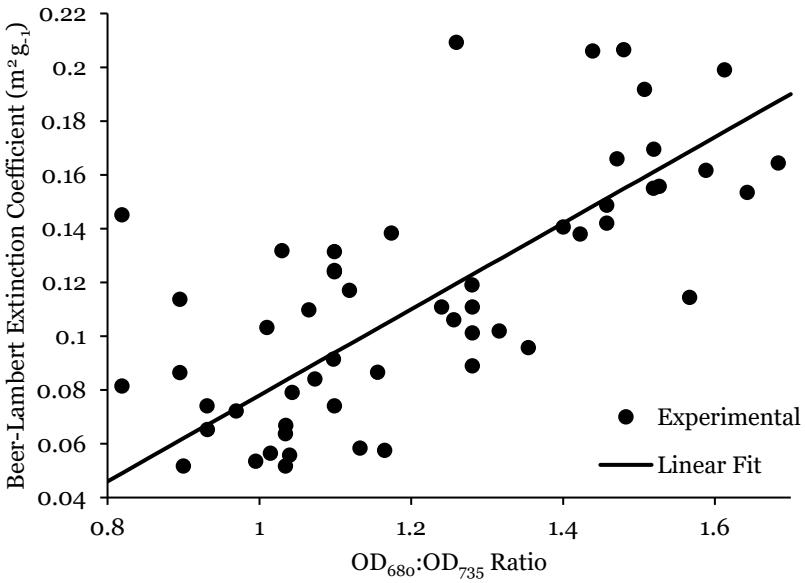

Figure 3.2: Beer-Lambert extinction coefficient (ε) correlated to the ratio of *Synechocystis* OD_{735}/OD_{680}, representing the increase in pigment concentration related to light extinction. The linear regression has a slope of 0.16 and y-intercept of -0.082 (standard error for ε = 0.0044 $m^2 g^{-1}$, R^2 = 0.47).

At very high LI_{acc}, ε_{min} theoretically represents ε for only light scattering. For this condition, the biomass should have minimal light-absorbing pigments, and I consider the fraction of ε due to absorbance negligible. Using light microscopy, I observed minor changes in cell size in response to photoacclimation to the range of LI values (Figure S3.4); changes in cell size would suggest changes in light scattering at changing LI_{acc}. However, the strong trend in Figure 3.2 between ε and OD_{680}/OD_{735} suggests that the changes in ε are dominated by absorbance, and, therefore, ε_{min} (reflecting scattering) can be assumed to be a constant (assuming constant reactor geometry and X). The amount of light absorbed is then given by the difference between total extinction and scattering: $(\varepsilon - \varepsilon_{min})*LI_{ave}$.

The shape of the ε curve with respect to LI_{acc} is roughly inverse to a Michaelis-Menton or Monod-type function, which is sometimes used to represent the effects of LI (or a soluble substrate) on growth kinetics (Béchet et al., 2013; Monod, 1949). The increase in ε supports that *Synechocystis* was mounting a physiological response to counteract the normal decline in growth rate with lowered LI. These countering trends in LI_{acc} and ε suggest that *Synechocystis* growth kinetics may be best modeled based on the light absorbed -- $((\varepsilon - \varepsilon_{min})*LI_{ave})$ -- rather than simply LI_{ave}. While ε may depend on other factors (e.g., nutrient concentrations and light spectrum; my white LEDs differ from sunlight), LI acclimation had a significant and systematic impact on ε. Thus, ε is an appropriate and useful metric for the biomass's photoacclimation state.

3.5. Conclusion

The Beer-Lambert extinction coefficient (ε) of *Synechocystis* sp. PCC6803 changed significantly and systematically in response to photoacclimation to a wide range of light intensities. Specifically, ε was highest for biomass grown at lower LI_{acc} (~0.18 m^2 g^{-1}) and stabilized at a much lower level (~0.045 m^2 g^{-1}) when LI_{acc} was at very high values (up to 2000 μmol m^{-2} s^{-1}). The increase in ε at low LI_{acc} appears to be a physiological response to counteract the normal decline in growth rate with lowered LI_{acc}, and this is supported by the increase in OD_{680}/OD_{735}. Measuring ε may be an appropriate metric to represent the photoacclimated state of the biomass.

3.6. Supplementary Material

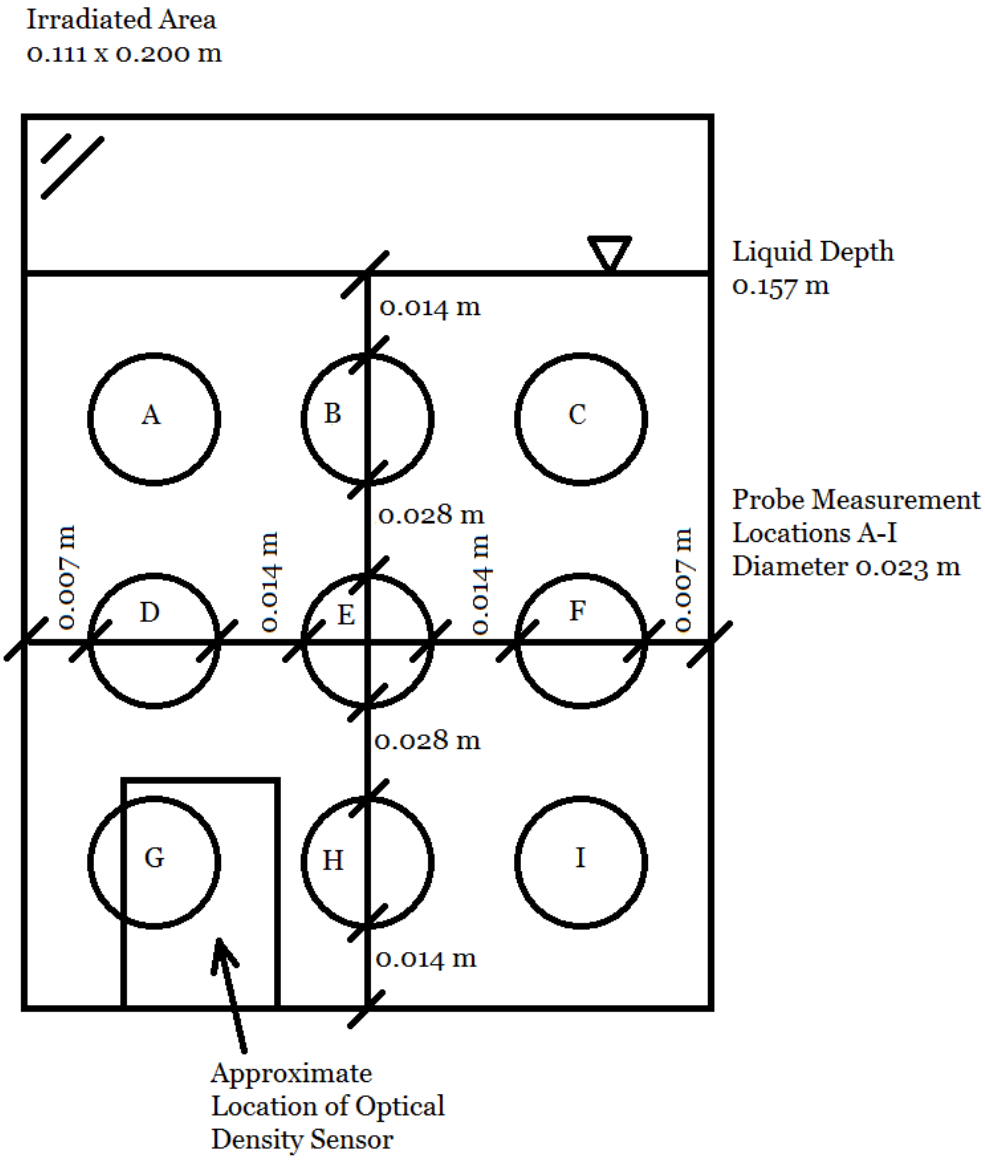

Figure S3.1: Schematic LI-measuring locations in FMT photobioreactor. The probe was a LI-190 PAR sensor

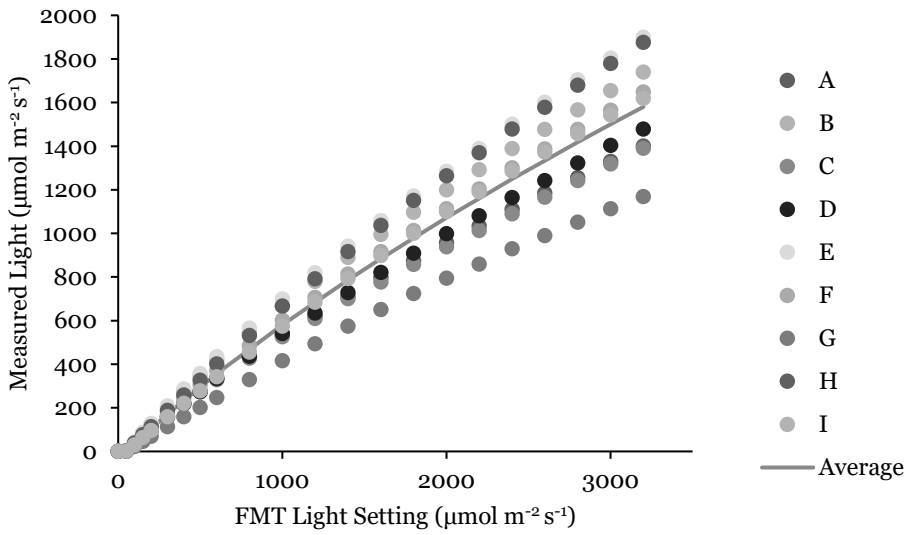

Figure S3.2: Measured LI (LI_o) values at 9 locations inside the FMT photobioreactor at 23 different FMT light settings (LI_{FMT}). Letters correspond to locations in Figure S3.1. The average line follows $LI_o = 2.06*(LI_{FMT}-81.2)^{0.826}$ (standard error = 8.86 µmol m^{-2} s^{-1}).

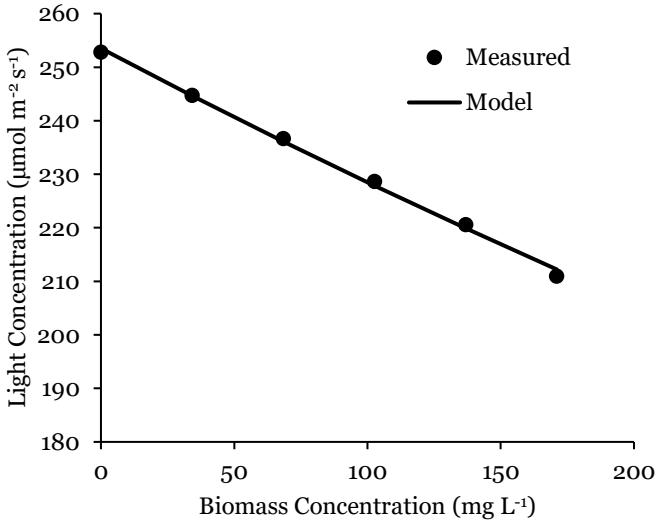

Figure S3.3: Example extinction coefficient (ε) determination for a 171-mg L^{-1} culture diluted to 4 other concentrations, along with a deionized-water sample, with a depth of 9 mm. The modeled curve uses the Beer-Lambert Equation (Equation 3.1) where ε = 0.12 m^2 g^{-1} for this sample.

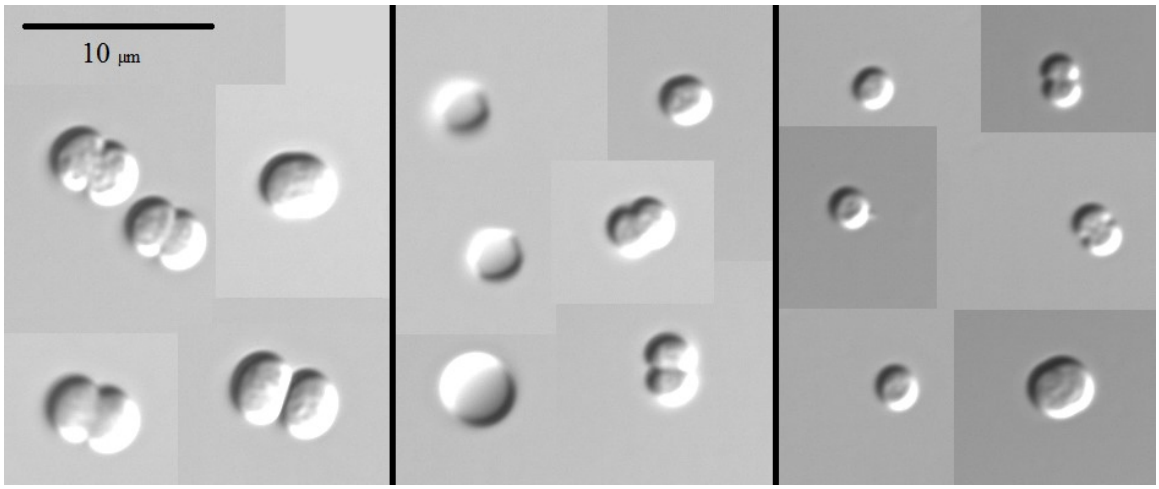

Figure S3.4: Randomly selected light microscopy images of *Synechocystis* cells showing the variation in morphology. Cells on the left were grown under the highest LI_{ave} (LI_{ave} = 1370 μmol m^{-2} s^{-1}), center under a moderate LI_{ave} (LI_{ave} = 317 μmol m^{-2} s^{-1}), and right under the lowest LI_{ave} (LI_{ave} = 27 μmol m^{-2} s^{-1}). All cells are coccus shaped and form conjoined spheres during cell division which makes up the largest particles. Particle diameters range from 2-5 μm, and average cell diameter appears to be larger at higher LI_{ave}. Differences in morphology, however, have little impact on ε compared with changes in pigmentation.

4. LIGHT-DEPENDENT KINETIC MODEL FOR MICROALGAE EXPERIENCING PHOTOACCLIMATION, PHOTODAMAGE, AND PHOTODAMAGE REPAIR

4.1. Abstract

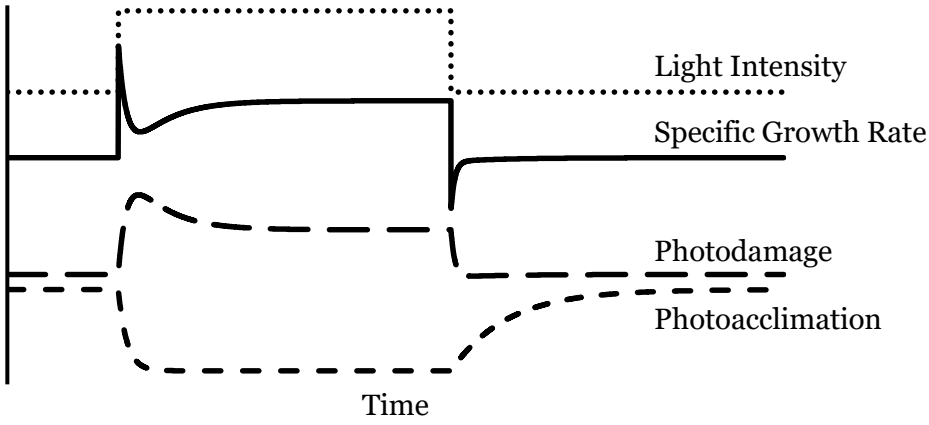

Microalgae naturally are exposed to changing light conditions. While a higher light intensity can promote a faster growth rate, it also can cause photodamage that leads to a temporary or semi-permanent decline in growth rate. I developed a model of photosynthetic growth including photoacclimation, reversible photodamage to photosystem II (PSII), and more severe photodamage to photosystem I (PSI). Phototrophic biomass optimizes its photosynthetic machinery to the light intensity it is experiencing; this is captured in the model by photoacclimation, in which photodamage to PSII caused by absorbed light is balanced by repair. However, repair of PSII photodamage can be overwhelmed by increases of light outside the photoacclimated condition, and this leads to severe PSII photodamage that slows the cells' specific growth rate. Furthermore, very large increases in light intensity can lead to photodamage to PSI, which is semi-permanent in that it can take days to weeks to repair. My model captures all these phenomena. Example model outputs demonstrate the importance of each phenomenon for increases and decreases in light intensity from the photoacclimated state.

4.2. Introduction

In natural conditions, cyanobacteria and single-celled algae (collectively referred to as microalgae) are exposed to constantly changing light conditions due to diurnal and seasonal light patterns, variations in incident light intensity (LI) over time, and mixing in the water column. Because microalgae are photosynthetic, exposing them to greater LI should lead to higher growth rates; however, changing LI also can lead to more complex phenomena, namely photoacclimation, photodamage, and photodamage repair (Falkowski and LaRoche, 1991; García-Camacho et al., 2012; Powles, 1984). Capturing these phenomena in a mathematical model can improve predictions of photosynthetic activity and give further insight to bioreactor design for microalgae cultivation (García-Camacho et al., 2012).

Photoacclimation is a set of changes in macromolecular composition (cell morphology, pigment concentration, and enzymes associated with photosynthesis and respiration) in response to differing light conditions (Falkowski and LaRoche, 1991). Photoacclimation allows microalgae to optimize photosynthetic activity for a given LI. Sudden increases in LI from a photoacclimated state, however, leave biomass susceptible to photoinhibition that alters the capacity of microalgae to harvest light and leads to a decrease in the rate of photosynthesis (MacIntyre et al., 2002). As I document in Chapter 5 with extensive experimental results and has been seen previously (Post, 1987; Tomaselli et al., 1997), a large and sudden step from low LI to high LI gives an initial spike in the rate of photosynthetic growth, but soon the rate declines to a value below the eventual steady-state growth rate of the new LI. The initial spike in growth is due to rapid accumulation of carbohydrates, and the slow down after the spike arises from near complete reduction of the plastoquinone pool, which leads to photodamage (sometimes called photoinactivation) (Post, 1987).

The literature describes two types of photodamage -- to photosystem I (PSI) and to photosystem II (PSII) -- with the later occurring far more frequently (Gururani et al., 2015). It is believed that the primary mechanism of PSII photodamage occurs when antenna complexes enter triplet states during light absorption and create reactive oxygen species (ROS) that damage the photosynthetic machinery (Erickson et al., 2015; Szabó et al., 2005). The main target of these ROS is the D1 protein, the primary electron-accepting protein from the oxygen evolving complex (Blankenship, 2002). The D1 protein has damage and repair mechanisms that are active under all illuminated conditions, but photoinhibition occurs when the rate of damage exceeds the rate of repair, such as after a sudden change of light intensity (Edelman and Mattoo, 2008; Kok, 1956a). While PSII photodamage is thought to be proportional to light intensity, the loss of this balance is primarily caused by an inactivation of the repair function (Gururani et al., 2015; Nishiyama et al., 2011). Repair of PSII photodamage is a complex process involving disassembly of the damaged component, reassembly of a working unit, and its insertion into a PSII complex (Dasgupta et al., 2008; Nath et al., 2013; Vinyard et al., 2013).

PSI is more protected than PSII, but damage still occurs when the flow of electrons from PSII exceeds the capacity of the electron acceptors in PSI (Erickson et al., 2015; Sonoike, 2011; Tikkanen et al., 2014). Because the source of photodamage is electrons from PSII, photodamage to PSII effectively protects PSI under normal fluctuations in LI; however, intense LI can lead to photodamage to PSI (Sonoike, 2011; Tikkanen et al., 2014). Repair to PSI is very slow, on the order of days to weeks, and inhibited PSI can lead to substantial photodamage to PSII because of a lack of electron acceptors from PSI (Scheller and Haldrup, 2005; Sonoike, 2011).

In Chapter 3, I suggested that, for *Synechocystis* sp. PCC 6803 (*Synechocystis* from here) the light extinction coefficient from absorbance (ε_{abs}) is a suitable metric of photoacclimation. Here, I expand upon the ε_{abs} concept by introducing four new state variables: LI_p, representing a pool of absorbed light energy; ε_{nf}, representing PSII photodamage; ζ, representing PSII repair inhibition; and δ, representing PSI photodamage. I develop and illustrate a kinetic model accounting for photoacclimation, PSII photodamage, PSII photodamage repair, and PSI photodamage. PSI photodamage is considered permanent and, therefore, I do not address repair. While a number of light-dependent models of photosynthesis can be found in the literature (reviewed by Béchet et al. (2013)), few account for photoacclimation, photodamage, and photodamage repair, and mine is the first to address PSI photodamage. In Chapter 5, I evaluate my model experimentally using *Synechocystis* and find that my model describes well the effects of sudden light-intensity changes on the specific growth rate. Here, I present a set of modeling experiments that demonstrate the features of the model and why modeling without photoacclimation and photodamage can seriously overestimate the rate of photosynthetic growth during changes in light. These modeling results lay the foundation for understanding the experimental results of Chapter 5.

4.3. Modeling Growth with Photoinhibition Phenomena

The first step in photosynthetic growth is the absorption of light into a pool of absorbed light energy (LI_p; μmol g^{-1}). I describe the accumulation of LI_p with the following relationship:

$$\frac{dLI_p}{dt} = \left(\varepsilon_{abs} LI - \varepsilon_{nf} LI - \left(\frac{k_{LI} LI_p}{k_{LI}+LI_p} + \frac{LI_p^2}{k_{LI}+LI_p}\right) k_{LIp}\right) \frac{86400s}{d} \qquad \text{Equation 4.1}$$

where ε_{abs} (m^2 g^{-1}) is the specific light absorption, LI (μmol m^{-2} s^{-1}) is the light intensity, k_{LI} (μmol g^{-1}) is the half-maximum-rate light absorption, ε_{nf} (m^2 g^{-1}) is PSII photodamage, and K_{LIp} (s^{-1}) is the rate constant of light-pool dissipation. From left to right, Equation 4.1, a mass balance on the pool of absorbed LI, includes terms for light absorption, non-photochemical quenching (NPQ) from damaged biomass, photochemical light quenching (i.e., for photosynthetic growth), and NPQ from other pigments. The conversion factor (86400 s d^{-1}) is necessary to show accumulation per day rather than per second so that Equation 4.1 is consistent with the other rate equations. Equation 4.1 has its greatest importance in situations of rapidly changing LI, such as flashing light or rapid mixing. When changes to LI are more gradual (e.g., light changes > 1 min apart or < 10 μmol m^{-2} s^{-1}), LI_p can be simplified to $LI_p = (\varepsilon_{abs} - \varepsilon_{nf})\ LI/k_{LIp}$ with minimal effect on the growth rate.

To capture all of the phenomena associated with photoinhibition, my model uses four biomass state-variables: photoacclimation (represented by ε_{abs}), PSII photodamage (ε_{nf}), the reduction in PSII repair or repair inhibition (ζ; m^2 g^{-1}), and PSI photodamage (δ; m^2 g^{-1}). Figure 4.1 is a schematic of the interactions of these state variables and how they contribute to phototrophic growth. All four state variables depend on LI, and they sequentially affect each other. Ultimately, the interdependent effects are captured by ε_{nf}, and the specific growth rate (μ, d^{-1}) is given by:

$$\mu = \frac{\mu_{max} LI_p - \varepsilon_{nf} k_b}{k_{LI} + LI_p} - b \qquad \text{Equation 4.2}$$

where μ_{max} (d^{-1}) is the maximum μ, k_b ($\mu mol\ m^{-2}\ d^{-1}$) is the photoinhibition decay constant, and b (d^{-1}) is the endogenous-decay constant. Equation 4.2 is a modified Monod formulation (Monod, 1949) applied to absorbed light similar to that used by Béchet et. al. (2015), except that I utilize (ε_{abs} - ε_{nf}) instead of ε, and I consider photoinhibition decay when they do not. The term LI_p is considered the growth-limiting "substrate" in this model. This model assumes a much higher Monod maximum specific growth rate (represented by μ_{max}) than could be achieved continuously, but this is balanced by the always present level of photoinhibition decay related to ε_{nf}. Changes in ε_{nf} represent the dynamics of growth after changes in LI.

As demonstrated in Chapter 3, ε decreases according to an inverse Monod-type function in LI for steady-state conditions, and ε is composed of light extinction from scattering (ε_{scat}) and from absorption (ε_{abs}). I assume that ε_{scat} is fixed for a given reactor geometry and biomass concentration (X); therefore, the steady-state ε_{abs} ($\varepsilon_{abs,ss}$) follows:

$$\varepsilon_{abs,ss} = \frac{(\varepsilon_{max} - \varepsilon_{scat} - \varepsilon_{abs,min}) k_\varepsilon}{k_\varepsilon + \frac{LI_p k_{LIp}}{\varepsilon_{abs}}} + \varepsilon_{abs,min} \qquad \text{Equation 4.3}$$

where ε_{max} ($m^2\ g^{-1}$) is the maximum light extinction, $\varepsilon_{abs,min}$ ($m^2\ g^{-1}$) is a minimum light extinction from absorption, and k_ε ($\mu mol\ m^{-2}\ s^{-1}$) is the half-maximum light absorption LI. Equation 4.3 depends on LI_p and ε_{abs}; however, LI can be substituted for: $LI_p\, k_{LIp}/\varepsilon_{abs}$ when LI conditions are stable (LI is not rapidly changing; e.g., light changes > 1 min apart, or < 10 $\mu mol\ m^{-2}\ s^{-1}$).

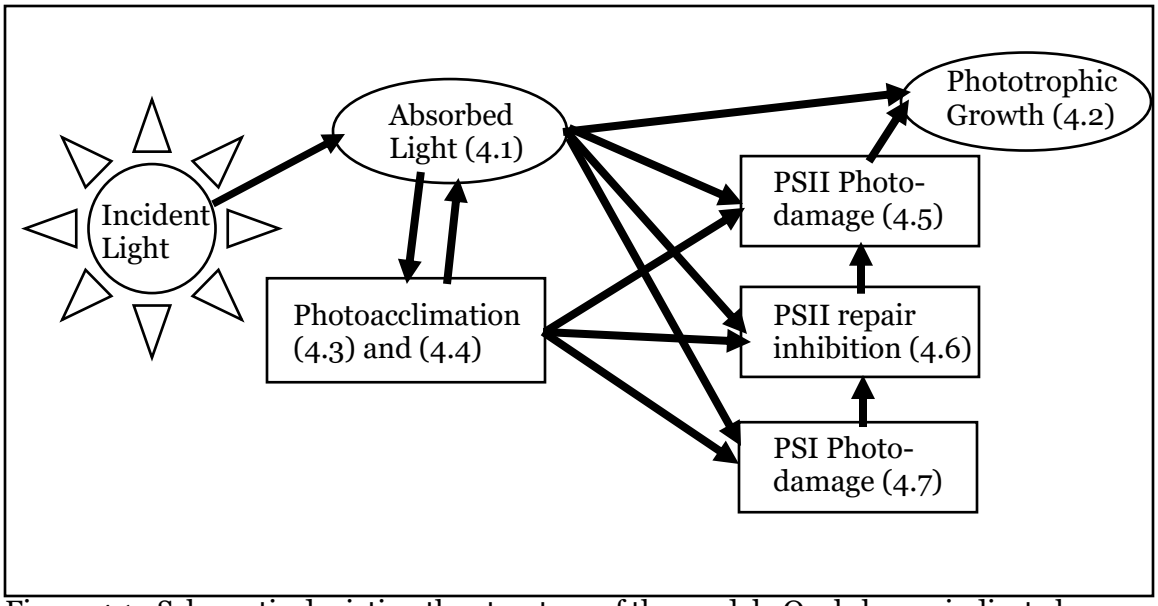

Figure 4.1: Schematic depicting the structure of the model. Oval shapes indicate key processes, and rectangles indicate the state-variables of the biomass with associated equations in parenthesis. The arrows lead from a state variable or process to another state-variable or process that is affected by the originating state variable or process.

With dynamic conditions, photoacclimation occurs at a rate proportional to the difference between ε_{abs} and $\varepsilon_{abs,ss}$:

$$\frac{d\varepsilon_{abs}}{dt} = \left(\varepsilon_{abs,ss} - \varepsilon_{abs}\right)k_{ad} \qquad \text{Equation 4.4}$$

where k_{ad} (d^{-1}) is the rate constant of photoacclimation. It is my observation (described quantitatively in Chapter 5 and previously suggested by García-Camacho et al., (2012)), that k_{ad} is larger with increasing LI than decreasing LI; therefore, $k_{ad,up}$ (k_{ad} when $\varepsilon_{abs,ss} < \varepsilon_{abs}$) is distinguished from $k_{ad,dn}$ (k_{ad} when $\varepsilon_{abs,ss} > \varepsilon_{abs}$). Mechanistically, this difference occurs because acclimating to lower light requires the biomass to generate more photosynthetic pigmentation, which takes more energy than decreasing photosynthetic pigmentation, which occurs under increasing light.

The net rate of PSII photodamage accumulation ($d\varepsilon_{nf}/dt$) occurs according to a balance between photodamage and photodamage repair:

$$\frac{d\varepsilon_{nf}}{dt} = LI_p k_{d1} - \frac{(k_{r1}\varepsilon_{nf} - k_{r2} LI_p \zeta)^*}{k_{LI} + LI_p} \qquad \text{Equation 4.5}$$

* If $k_{r1}\varepsilon_{abs} < k_{r2}LI_p\zeta$, the term is 0

where k_{d1} (m^2 μmol^{-1} d^{-1}) is the rate constant for PSII photodamage, k_{r1} (μmol g^{-1} d^{-1}) is the normal rate constant for PSII photodamage repair, and k_{r2} (d^{-1}) is the rate constant for the reduction in PSII repair occurring in conditions of light in excess of the photoacclimated condition. This relationship captures photodamage occurring proportional to light absorption, light-dependent repair, and reduced repair with sudden changes in light, which is described by ζ:

$$\frac{d\zeta}{dt} = \left(\left(\varepsilon_{abs} - \varepsilon_{abs,ss}\right)^* - (\zeta - \delta)y^{**}\right)\frac{k_{r3}}{\left(k_{r4} + LI_p\right)^2} + k_{d3}(\delta - \zeta)(1 - y^{**}) \qquad \text{Equation 4.6}$$

* If $\varepsilon_{abs} < \varepsilon_{abs,ss}$, the term is 0
** If $\zeta > \delta$, y = 1, else y = 0

where y (unitless) is a switch term, k_{r3} (μmol^2 g^{-2} d^{-1}) is the maximum rate of generation/repair of repair inhibition which is quantitatively equal to k_{r1}, k_{r4} (μmol g^{-1}) is an LI_p constant of repair inhibition, and k_{d3} (d^{-1}) is a rate constant of PSI photodamage. The first term is repair inhibition, and the second and third terms are recovery from repair inhibition; they switch depending on the value of δ. Recovery from repair inhibition can only progress to the level of δ, and if δ exceeds ζ, ζ is brought to the level of δ by the switch. ζ can never be less than δ, and because once δ > 0, it is permanent, this causes a permanent level of ζ.

PSI photodamage (δ) occurs under conditions of extreme increases in LI, which I represent as:

$$\frac{d\delta}{dt} = (\varepsilon_{abs} - \varepsilon_{abs,ss} - \delta - (\varepsilon_{max} - \varepsilon_{scat} - \varepsilon_{abs})k_{d2})^* k_{d3} \qquad \text{Equation 4.7}$$

* If this term is less than 0, the term is 0

where k_{d2} (unitless) is the constant of light absorbance change when PSI photodamage occurs. The onset of PSI photodamage depends on photoacclimation. On the time-scale of the study described in Chapter 5, PSI photodamage can be considered permanent, which means that a term for PSI photodamage repair is not addressed.

For conditions where LI is not changing (assuming $\delta = 0$, and $\zeta = 0$), a steady-state level of ε_{nf}, which I refer to as the steady-state ε_{nf} ($\varepsilon_{nf,ss}$), is established. It can be computed by rearranging Equation 4.5 and assuming $d\varepsilon_{nf}/dt = 0$:

$$\varepsilon_{nf,ss} = \frac{k_{d1}}{k_{r1}}\left(k_{LI}LI_p + LI_p^2\right) \qquad \text{Equation 4.8}$$

Because LI_p depends on ε_{nf}, I simplify $LI_p = \varepsilon_{abs}LI/k_{LIp}$, because $\varepsilon_{abs} >> \varepsilon_{nf}$ at steady-state.

All modeling results presented here use parameter values listed in Table 4. The estimation of these parameters for *Synechocystis* is described in Chapter 5.

Table 4.1: Best-Fit Parameters for Model Equations 4.1-4.8, as Determined in Chapter 5 for *Synechocystis*.

parameter	equations	description	value	units
k_{LI}	4.1, 4.2, 4.5 & 4.8	light-limited half-maximum-rate absorbed light growth constant	50	$\mu mol\ g^{-1}$
k_{LIp}	4.1 & 4.3	rate constant of light-pool dissipation	1	s^{-1}
μ_{max}	4.2	maximum specific growth rate	12	d^{-1}
k_b		photoinhibition decay constant	1400000	$\mu mol\ m^{-2}\ d^{-1}$
b		endogenous-decay constant	0	d^{-1}
ε_{max}	4.3	light extinction for biomass photo-acclimated to the lowest LI	0.18	$m^2\ g^{-1}$
ε_{scat}		light extinction from scattering	0.033	$m^2\ g^{-1}$
k_ε		half-maximum light absorption LI	380	$\mu mol\ m^{-2}\ s^{-1}$
$\varepsilon_{abs,min}$		minimum light extinction from absorbance	0.012	$m^2\ g^{-1}$
$k_{ad,up}$	4.4	rate constant of photoacclimation (ε_{abs}) for increasing light	13	d^{-1}
$k_{ad,dn}$		rate constant of photoacclimation (ε_{abs}) for decreasing light	2	d^{-1}
k_{d1}	4.5 & 4.8	rate constant of PSII photodamage (ε_{nf})	0.000088	$m^2\ \mu mol^{-1}\ d^{-1}$
k_{r1}		rate constant of normal PSII photodamage (ε_{nf}) repair	1600	$\mu mol\ g^{-1}\ d^{-1}$
k_{r2}	4.5	rate constant for the reduction in PSII photodamage (ε_{nf}) repair	1.3	d^{-1}
k_{r3}	4.6	maximum rate of generation/repair of repair inhibition (ζ)	1600	$\mu mol^2\ g^{-2}\ d^{-1}$
k_{r4}		LI_p constant of repair inhibition (ζ)	13	$\mu mol\ g^{-1}$
k_{d2}	4.7	constant of light absorbance where PSI photodamage (δ) occurs	2.6	unitless
k_{d3}	4.6 & 4.7	rate constant of PSI photodamage (δ)	14	d^{-1}

4.4. Modeled Results and Discussion

To illustrate how my model captures light-dependent growth, I show a series of model outputs. First, I show steady-state growth as a function of light, which can be represented by light intensity or light absorption (Figure 4.2). Then, I present several non-steady-state growth responses for biomass experiencing sudden changes in light. Steps in light start with biomass photoacclimated to 75 μmol m^{-2} s^{-1} (Figure 4.3), 25 μmol m^{-2} s^{-1} (Figure 4.4), and 600 μmol m^{-2} s^{-1} (Figure 4.5). In addition to μ, I plot ε_{abs} and ε_{nf}, and, in the times series plots, I plot ζ and δ when it is applicable for capturing the trends in μ.

4.4.1. Steady-state Photoacclimated Growth-Irradiance-Curve

Figure 4.2 shows the modeled steady-state response of specific growth rate to LI (Figure 4.2 C & D) and to light absorbed (LI_p or $\varepsilon_{abs}LI/k_{LIp}$; Figure 4.2 A & B), including ε_{abs} and ε_{nf}. I refer to a relationship in which LI or LI_p is the growth limiting "substrate" as a growth-irradiance-curve. The literature commonly refers to photosynthesis-irradiance curves (PI-curves) (Jassby and Platt, 1976), which typically are snapshots of photosynthetic activity measured by oxygen evolution or carbon fixation (Johnson and Sheldon, 2007). PI-curves can vary widely in their shape, depending on photoacclimation (Platt and Jassby, 1976). Because my model considers steady-state, fully photoacclimated growth, the growth-irradiance-curves in Figure 4.2 are fixed for a particular phototrophic microorganism. My model utilizes LI_p as the "substrate" (reflected in Equation 4.2) based on the fact that absorbed light is what promotes growth. However, the "substrate" can be converted to LI, because the model incorporates a relationship for ε_{abs} based on LI (plotted in Figure 4.2 C & D for *Synechocystis*), and this yields a fixed steady-state growth-irradiance-curve based on LI.

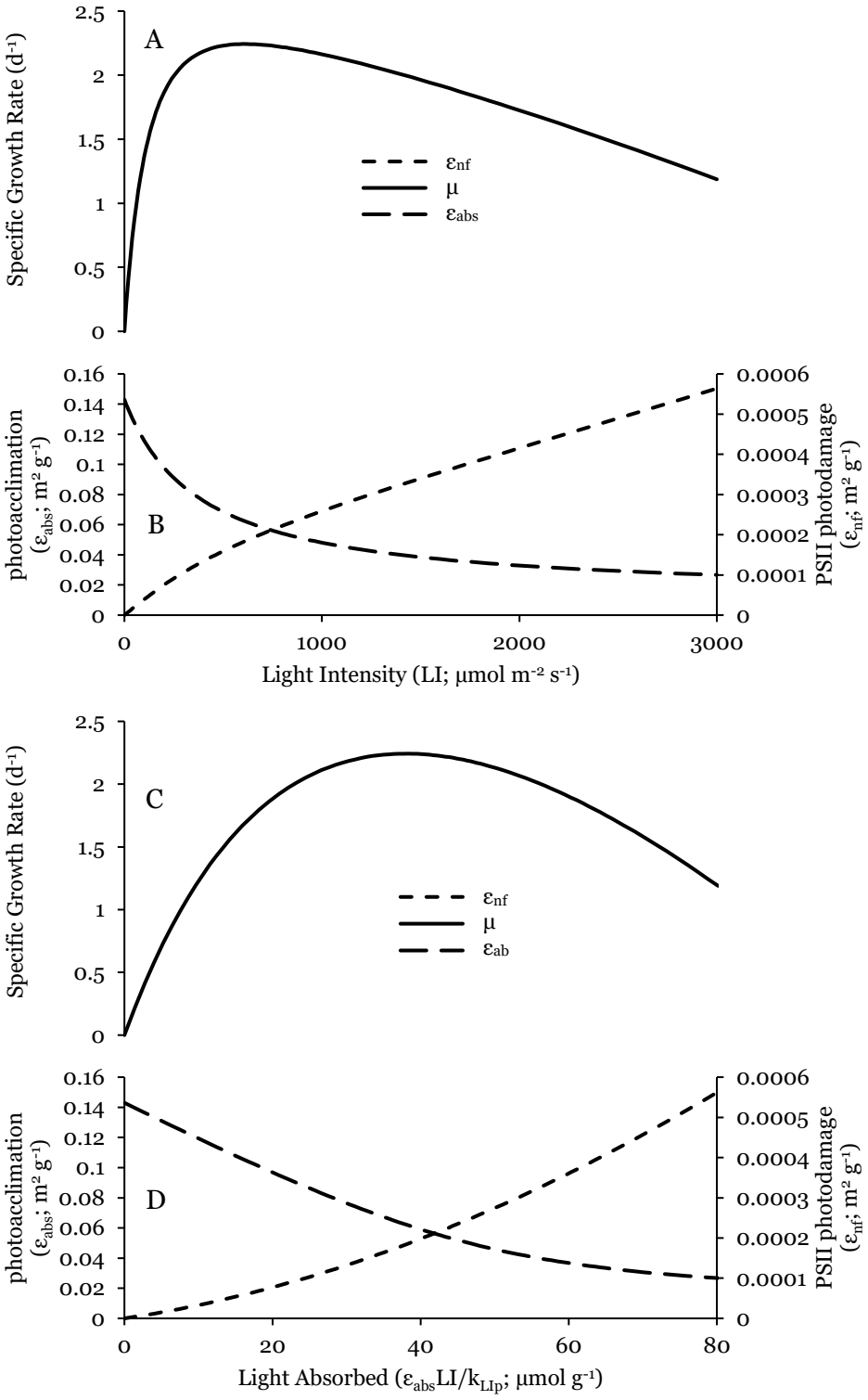

Figure 4.2: Steady-state growth-irradiance-curves for μ and also showing ε_{abs} and ε_{nf}. Plots A and B are plotted against light intensity (LI), and plots C and D are against light absorbed ($\varepsilon_{abs}LI/k_{LIp}$). The model is Equations 4.2, 4.3 and 4.8, and parameters (determined for *Synechocystis* in Chapter 5) are listed in Table 4.1.

For either "substrate," the growth-irradiance-curve shows the typical three regions: light-limitation, where the relationship between LI and photosynthetic activity is relatively linear (up to approximately 300 μmol m^{-2} s^{-1} or 25 μmol g^{-1}); light-saturation, where additional light does not increase photosynthetic activity (from approximately 300-1600 μmol m^{-2} s^{-1} or 25-60 μmol g^{-1}); and photoinhibition, where additional light slows growth (greater than 1600 μmol m^{-2} s^{-1} or 60 μmol g^{-1}) (Béchet et al., 2013).

The region of photoinhibition is characterized by a large accumulation of photodamage (ε_{nf}, plotted in Figure 4.2). Mechanistically, the model shows increasing ε_{nf} with additional light absorption or LI, and μ plateaus and then declines in parallel. As LI increases, ε_{abs} decreases towards $\varepsilon_{abs,min}$, since the phototrophs try to reduce light absorption and photodamage. A unique feature to the shape of my growth-irradiance-curve is that, at high light intensity, its curvature continues to bend down so that it eventually goes negative (happening at 4800 μmol m^{-2} s^{-1}). Most other PI-curve formulations level out, approaching zero, but not becoming negative (Iwakuma and Yasuno, 1983).

4.4.2. Growth Response - Increasing Light Steps from 75 μmol m^{-2} s^{-1}

Figure 4.3 displays light-steps from 75 μmol m^{-2} s^{-1} to 300 or 1000 μmol m^{-2} s^{-1}. Both curves capture the spike in growth immediately after the change in light, followed by the sharp decline and restabilization to a new steady-state. My model predicts a large, but transient spike in μ, up to 8 d^{-1} with the LI of 1000 μmol m^{-2} s^{-1}. This is possible because the value of μ_{max} is 12 d^{-1} (best fit for *Synechocystis* in Chapter 5); although μ_{max} = 12 d^{-1} cannot be sustained (as seen in the growth-irradiance-curves of Figure 4.2), it can be approached transiently before photodamage sets in (Figure 4.3). Thus, the model incorporates the possibility of a very high specific growth rate if photoinhibition could be

completely suppressed. The low level of photodamage at a lower light condition before an increasing light-step allows a brief period following the step where μ approaches more closely to its true μ_{max} before photodamage has time to accumulate.

The light-step from 75 to 1000 μmol m^{-2} s^{-1} shows a larger spike and depression compared to the light step from 75 to 300 μmol m^{-2} s^{-1}; however, the increase in spike height is not proportional to the light increase, since μ follows a Monod-curve that saturates as LI increases. PSI photodamage (δ) also sets in immediately with the light-step from 75 to 1000 μmol m^{-2} s^{-1} due to the excessive absorption of light, whereas the light step from 75 to 300 μmol m^{-2} s^{-1} does not show any δ because the threshold of light absorption increase has not been reached. The onset of δ is fast, because the excess absorption can last for only a brief period before ε_{nf} reduces absorption and ε_{abs} photoacclimates. In both light-steps, excess PSII photodamage (ε_{nf}) occurs after the spike in growth (peaking at about 0.25 days), which is a result of a reduced ability to repair ε_{nf} (represented by ζ) because of the difference between ε_{abs} and $\varepsilon_{abs,ss}$.

Following the spike and depression in μ, μ restabilizes; this is the photoacclimation response based on the ability to repair PSII photodamage (ε_{nf}). Thus, ε_{abs} decreases to $\varepsilon_{abs,ss}$ (taking about 0.25 days), and ε_{nf} is reduced to the new steady-state condition (taking about 2 days). My model represents the effect of PSI photodamage (δ) by contributing to the repair inhibition (ζ) of ε_{nf}, which, therefore, leads to a final ε_{nf} higher than is expected by the steady-state condition in the light-step from 75 to 1000 μmol m^{-2} s^{-1}. It is the semi-permanent increase in ε_{nf} that causes the resulting reduction in μ. Mechanistically, damaged PSI cannot accept electrons from PSII, which causes a "back-up" of electrons, which would normally be used for PSII repair.

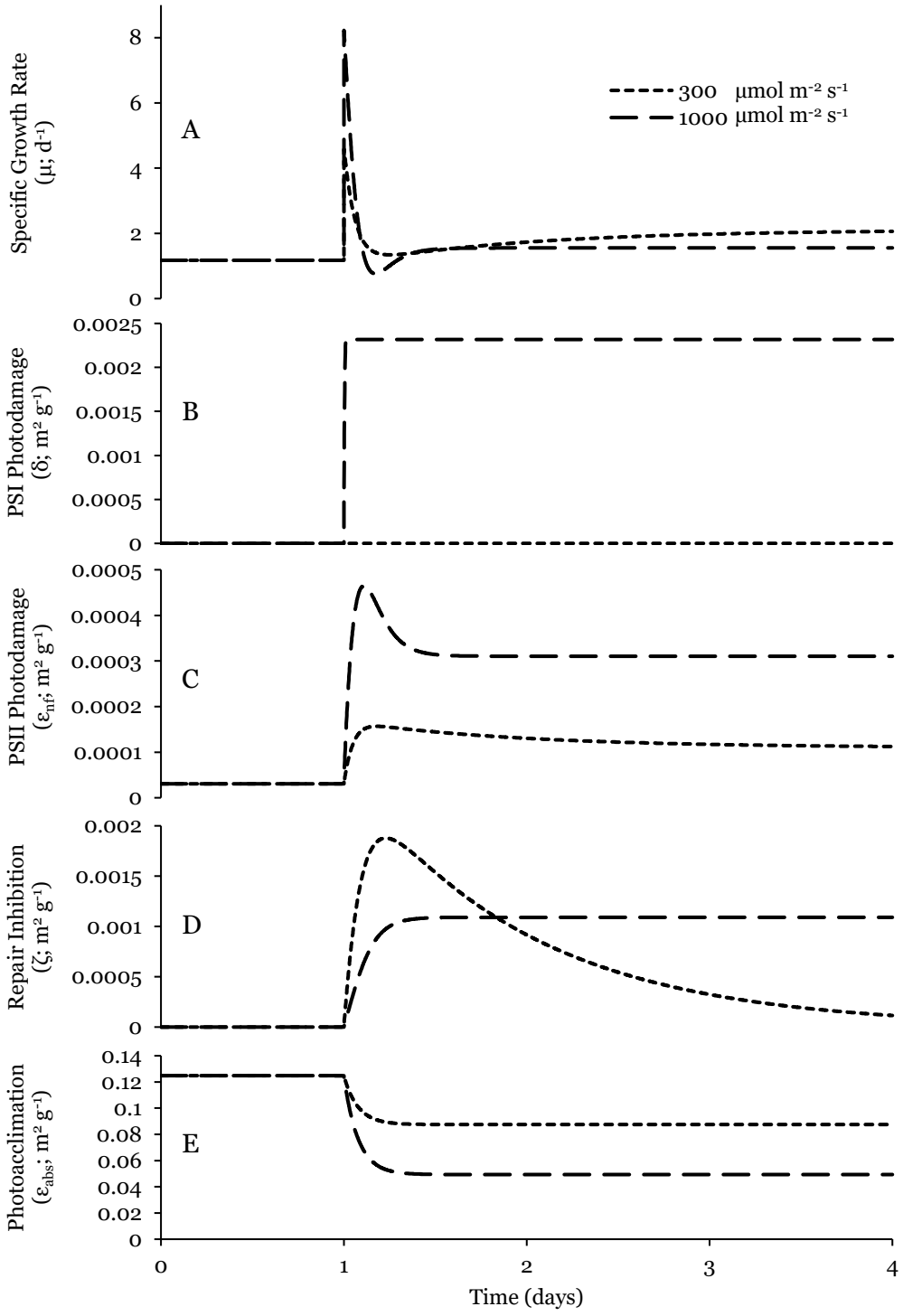

Figure 4.3: Modeled time-series of increasing light-steps for a culture starting at LI_{ave} = 75 μmol m^{-2} s^{-1} and stepping up at time 1 day to 300 and 1000 μmol m^{-2} s^{-1}. Plot A displays the specific growth rate, plot B PSI photodamage, plot C PSII photodamage, plot D PSII repair inhibition, and plot E photoacclimation. The model is Equations 4.1-4.7, and parameters are listed in Table 4.1.

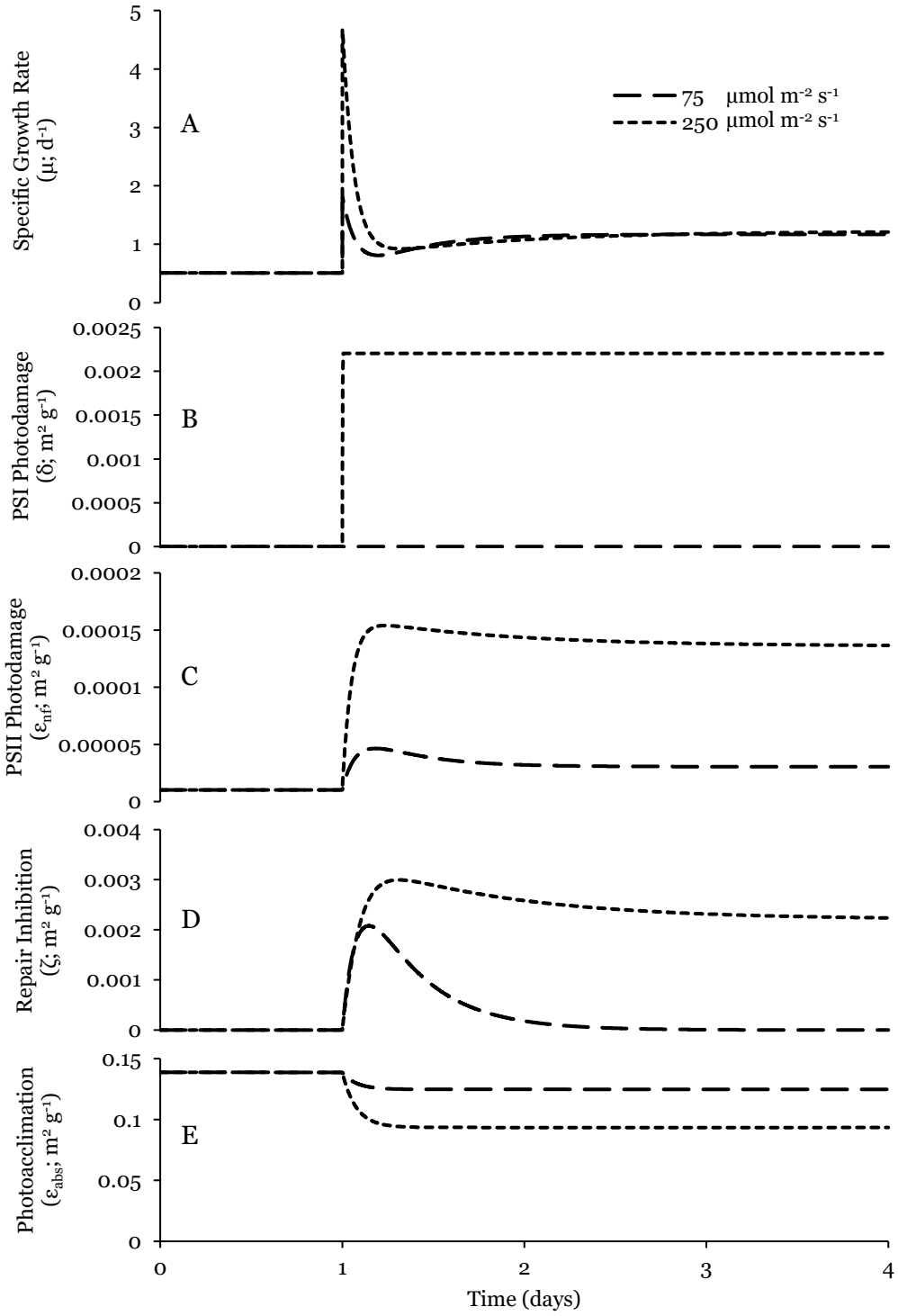

Figure 4.4: Modeled time-series of increasing light-steps for a culture starting at LI_{ave} = 25 μmol m^{-2} s^{-1} and stepping up at time 1 day to 75 and 250 μmol m^{-2} s^{-1}. Plot A displays the specific growth rate, plot B PSI photodamage, plot C PSII photodamage, plot D PSII repair inhibition, and plot E photoacclimation. The model is Equations 4.1-4.7, and parameters are listed in Table 4.1.

4.4.3. Growth Response - Increasing Light Steps from 25 μmol m^{-2} s^{-1}

Figure 4.4 displays light-steps from 25 μmol m^{-2} s^{-1} to 75 and 250 μmol m^{-2} s^{-1}. The trends are qualitatively similar to those described for Figure 4.3, but the resulting quantities are different. Because the starting LI in Figure 4.4 is lower, a smaller increase in LI is needed to see an equally distinct spike in μ and depression following. This is most evident by comparing the light-step from 75 to 300 μmol m^{-2} s^{-1} in Figure 4.3 and 25 to 250 μmol m^{-2} s^{-1} in Figure 4.4. Both have an LI increase of 225 μmol m^{-2} s^{-1}, but a starting LI of 75 μmol m^{-2} s^{-1} causes μ to spike from 1.1 to 4.5 d^{-1}, while the starting LI of 25 μmol m^{-2} s^{-1} has a spike from 0.5 to 4.6 d^{-1}. Modeling experiments with a lower starting LI show even more drastic spikes in μ (not shown here). Biomass acclimated to lower LI has a higher capacity for light-absorption (i.e., higher ε_{abs}), and this is what gives the biomass the capacity for a larger increase in light absorbed per increase in LI. The impact on μ is muted for very high LI, because growth follows a Monod-type function in which increased light absorbed results in a smaller relative increase in μ. This is particularly true for LI absorption greater than k_{LI} (50 μmol g^{-1} which occurs for steady-state growth at 1040 μmol m^{-2} s^{-1}).

Closely following the spike in μ is photoinhibition, which also is accentuated by a lower starting LI. Because the change in $\varepsilon_{abs,ss}$ is much larger with low starting LI, a light-step from a lower LI has a larger increase in ζ (the difference can be seen between Figures 4.3 and 4.4). Thus, biomass with a lower starting LI and subjected to a step increase in LI exhibits a larger spike in μ and a larger depression in μ following the spike.

The trends for PSII damage and repair also extend to PSI photodamage, represented by δ. Biomass photoacclimated to higher LI has lower ε_{abs}, which enables the biomass to withstand a larger increase in LI without causing $\delta > 0$. In Figure 4.4, the

LI increase of 225 μmol m^{-2} s^{-1} (light step from 25 to 250 μmol m^{-2} s^{-1}) caused δ = 0.0022 m^2 g^{-1}, whereas the same light step in Figure 4.3 (75 to 300 μmol m^{-2} s^{-1}) maintained δ = 0. PSI photodamage occurs with extreme light increases, when electron flow from PSII exceeds the capacity of PSI to accept them. A lower value of ε_{abs} and/or higher ε_{nf} reduces the electron flow from PSII, and, thus, protects PSI. In the model, PSI photodamage occurs for > 110 μmol m^{-2} s^{-1} for light steps from 25 μmol m^{-2} s^{-1} and for > 560 μmol m^{-2} s^{-1} for light steps from 75 μmol m^{-2} s^{-1}.

4.4.4. Growth Response - Decreasing Light-Steps from 600 μmol m^{-2} s^{-1}

Figure 4.5 displays light-steps from 600 μmol m^{-2} s^{-1} to 450 and 150 μmol m^{-2} s^{-1}. These step-down light changes show a sharp drop in μ immediately after the light change, but are followed by a rapid rebound as excess ε_{nf} is repaired and finally μ gradual increases as the biomass photoacclimates to the new steady-state. At no point does μ overshoot the new steady-state μ. The PSII photodamage repair only takes about 0.25 days, but the restabilization takes about 2 days due to the relatively slow rate at which photoacclimation occurs. The photoacclimation period is much longer than for increasing light-steps (Figures 4.3 and 4.4). Mechanistically, the slow response occurs because higher LI leads to less light-absorbing pigmentation (represented in the model by a lower ε_{abs}), which needs to be rebuilt as the biomass photoacclimates to the lower LI (higher ε_{abs}). The effect of ε_{nf} is less dramatic than the increasing light steps because the ability to repair ε_{nf} is not reduced (no ζ), and, therefore, the main impact from ε_{nf} is a higher level of ε_{nf} carried over from the previous light condition.

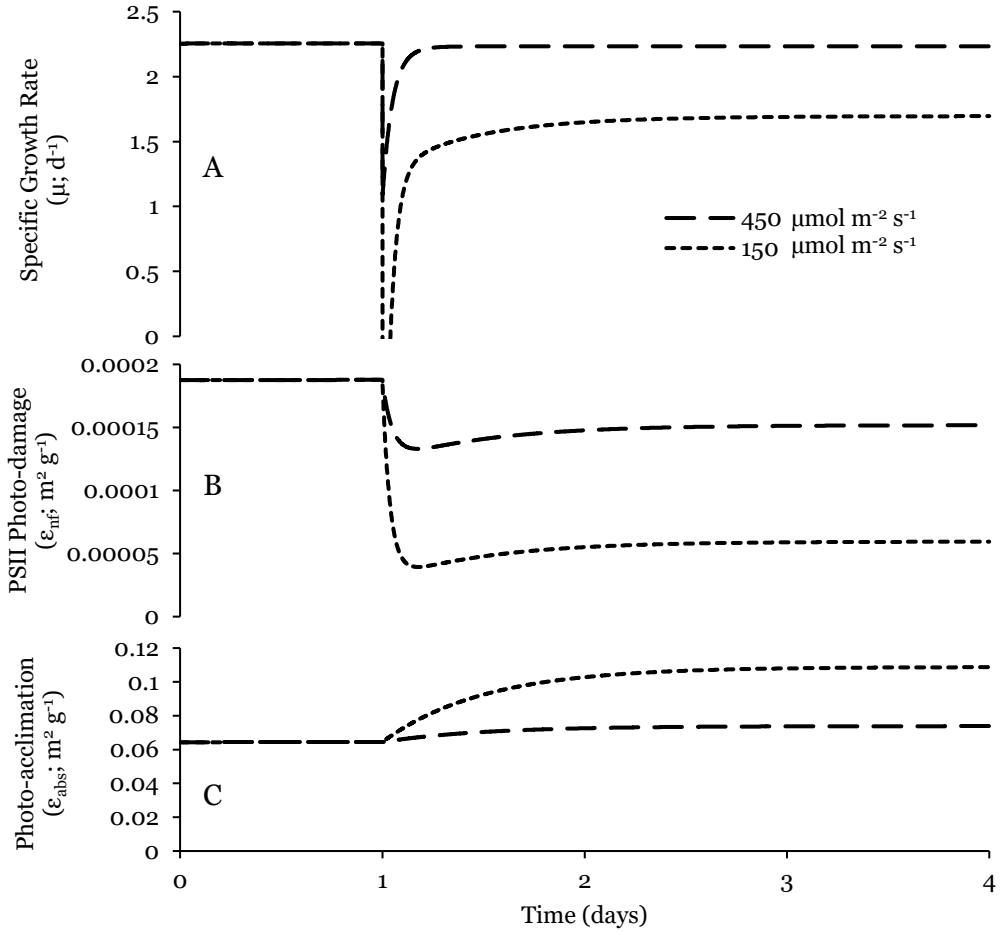

Figure 4.5: Modeled time-series of decreasing light-steps for a culture starting at LI_{ave} = 600 μmol m^{-2} s^{-1} and stepping down at time 1 day to 450 and 150 μmol m^{-2} s^{-1}. Plot A displays the specific growth rate, Plot B PSII photodamage, and Plot C photoacclimation. The model is Equations 4.1-4.5, and parameters are listed in Table 4.1.

4.4.5. Implications

The photodamage and repair model substantially improves our ability to understand and predict biomass production with changing LI. Figure 4.6 illustrates the value by comparing the computed differences between the three-day average μ after a light step using my dynamic model with the steady-state μ at each light condition. The latter is a traditional light-dependent growth model that does not consider the dynamics of changing light. I chose three days because the dynamics described by my model restabilize within that timeframe, except in the case of PSI photodamage. Curves were generated for light-steps from 25, 75, and 600 μmol m^{-2} s^{-1} (corresponding to Figures 4.3-4.5).

The steady-state μ overestimates μ based on the dynamics of μ after the light change in all cases. The difference is particularly pronounced when the light step is an increase that exceeds the threshold for PSI photodamage. PSI photodamage is apparent from the change in slope of the increasing light step curves: the slope changes at around 110 for light steps from 25 μmol m^{-2} s^{-1}, above which PSI photodamage occurred, and about 560 for light steps from 75 μmol m^{-2} s^{-1}. Below these thresholds, PSI is protected.

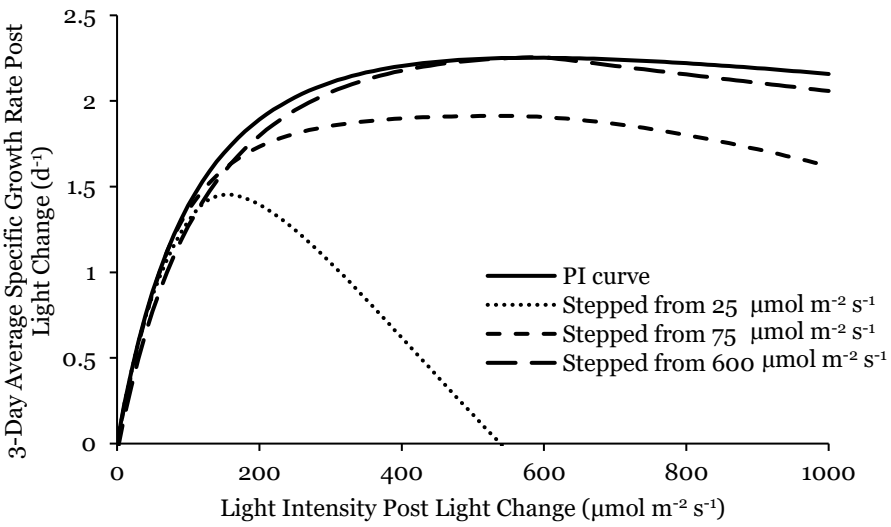

Figure 4.6: Comparison of modeled specific growth rate after a light step (averaged from the light step to 3 days after to capture dynamics of the change) with the steady-state growth-irradiance-curve (PI curve). The three light-step curves indicate the growth rate after a light step from 25, 75, and 600 µmol m^{-2} s^{-1} to the light intensity on the horizontal axis using model Equations 4.1-4.7. The steady-state growth-irradiance-curve is modeled using Equations 4.2, 4.3, and 4.8.

4.5. Conclusions

I present a model that is able to capture important dynamic effects of photoacclimation, photodamage, and photodamage repair following a change in LI. My model relies on four state variables: ε_{abs} for photoacclimation, ε_{nf} for PSII photodamage, ζ for PSII repair inhibition, and δ for PSI photodamage. The model captures these dynamic impacts of a step change in light intensity: 1) Immediately after a step increase in LI, μ spikes up, but then is depressed before a slow recovery to a new steady-state condition. These phenomena are related to photodamage and repair of PSII. 2) An extreme LI step increase leads to a semi-permanent decrease in μ that is related to damage to PSI. 3) The magnitude of decreases in μ after an increasing light step depends on the starting light condition. Lower LI before the step increase means that PSII can immediately absorb more light energy and generate greater electron flow, which causes the μ spike and subsequent photodamage. 4) A decreasing light-step leads to a relatively mild decrease in μ and a relatively slow recovery to the new steady-state. Ignoring the impact of photoacclimation and photodamage overestimates μ for most conditions of changing LI.

5. DYNAMIC RESPONSE OF *SYNECHOCYSTIS* SP. PCC 6803 TO CHANGES IN LIGHT INTENSITY

5.1. Abstract

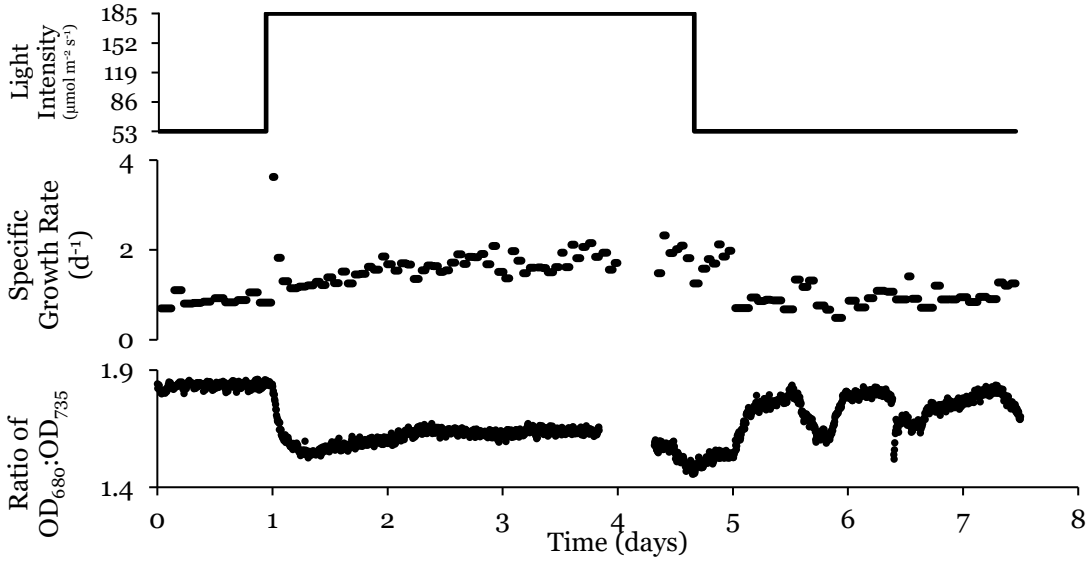

Chapter 4 developed a light-dependent kinetic model for microalgae experiencing photoacclimation, photodamage, and photodamage repair. Here, I experimentally evaluated and parameterized that model using *Synechocystis* sp. PCC 6803 subjected to a series of light-step experiments. In these experiments, the biomass density and average light intensity were held constant (after the step in light), and the dynamic response of the specific growth rate was measured. The dynamic response was captured in the model by the combined effects of light absorption, photoacclimation, and photodamage. The over-arching trend is that an increasing light-step gave a rapid spike in growth rate, followed by a depression and ultimately restabilization of the growth rate for the new light condition. A decreasing light-step led to a small depression in growth rate before a gradual restabilization for the new light condition. Photoacclimation was faster after an increasing light step than a decreasing light step. The model was able to capture and explain all of the experimental trends.

5.2. Introduction

Following a change in light intensity (LI), microalgae (collectively referring to single-celled algae and cyanobacteria) undergo a series of physiological changes that can be grouped into photoacclimation and photodamage to photosystems I and II (PSI and PSII). In Chapter 4, I review the mechanisms underlying these phenomena. Briefly, photoacclimation occurs as microalgae optimize their photosynthetic machinery for the LI they are experiencing (Falkowski and LaRoche, 1991). This includes increasing their light-absorbing pigmentation at lower LI and decreasing it at higher LI. Microalgae experience PSII photodamage under all LI conditions, but it is balanced by PSII photodamage repair with constant LI (Anderson et al., 1998). When microalgae are photoacclimated to low LI and the LI suddenly increases, their ability to repair the PSII photodamage declines, causing a temporary excess of PSII photodamage (Nishiyama et al., 2011). When the light-step increase is extreme, microalgae experience PSI photodamage, which is a semi-permanent decrease in their ability for photosynthetic growth (Sonoike, 2011).

Here, I explore the dynamics of microalgal growth for shifts in light using the cyanobacteria *Synechocystis* sp. PCC 6803 (simply *Synechocystis* from here). As I demonstrate with extensive experimental results and has been noticed before (Post, 1987; Tomaselli et al., 1997), microalgae experiencing an increasing light step show an immediate spike in photosynthetic growth rate, followed by a depression and then a gradual increase to stabilize at the new steady-state condition. The spike in growth is due to an initially low level of PSII photodamage and over-absorption of light energy; however, this spike is quickly overwhelmed by excess PSII photodamage before the microalgae can restabilize to the new steady-state growth rate. In contrast, a decreasing

light step leads to a sharp depression in growth rate that rebounds quickly near the new steady-state and finally slowly restabilizes to the new steady-state.

Using the experimental results obtained in this study, I parameterize the model presented in Chapter 4 and demonstrate its ability to represent all the phenomena of photoacclimation and PSI and PSII photodamage.

5.3. Materials and Methods

5.3.1. *Synechocystis* Growth-rate Experiments

I performed a series of steady-state growth experiments at different LIs and then carried out experiments with LI steps, tracking the specific growth rate (μ, d^{-1}) over time after each step. I used the same growth conditions as Chapter 3. Briefly, *Synechocystis* was received from the laboratory of Dr. Willem Vermaas, School of Life Sciences at Arizona State University and inoculated directly from a plate into a Photobioreactor FMT150 (Photon Systems Instruments, Drásov, Czech Republic; simply FMT form here) having an approximate liquid volume of 370 ml, a fixed temperature of 30°C, and air sparging at approximately 0.1 L min^{-1}. The system was operated in its turbidostat mode at an optical density (OD at 735 nm, or OD_{735}) between 0.20 and 0.21 and with the pH maintained between 7.5 and 8.5 using carbon dioxide sparging. The growth medium was autoclaved standard BG-11 (Rippka et al., 1979). OD_{735} and the ratio of OD at 680 nm (OD_{680}) to OD_{735} (OD_{680}/OD_{735}) were tracked over time.

I measured the photosynthetic growth rate based on the change in OD_{735}, which can be directly correlated to biomass dry weight (DW; mg L^{-1}). I also measured dry weight concentration daily by taking a dry 0.7-µm glass microfiber filter (Whatman®, Buckinghamshire, UK), filtering 10 ml of culture, drying the filter at 60°C overnight, subtracting the final weight from the initial weight, and dividing by 10 ml (Straka and Rittmann, 2017). Biomass concentrations used for computing μ were the OD_{735} multiplied by the DW/OD_{735} ratio taken the same day. Although I observed some variability in the DW/OD_{735} ratio with steady-state growth (an average and standard deviation of 590 ± 95 DW/OD_{735}), the variation was random and not related to the light intensity (LI). Immediately following an increasing light step, however, OD_{735} increased rapidly and did not correspond exactly to an increase in DW, which has a slight delay (5-

10 min.). A comparison of DW to OD_{735} for a representative experiment with a light-step increase is presented in Supplementary Material section 5.6.1. While the lack of synchrony between OD_{735} and DW was minimal on the time scale of the study, it introduced uncertainly in the experimental estimation of μ immediately following a light step. Therefore, I used a theoretical basis -- described in Parameterizing the Model to the Growth Data -- to determine μ_{max}.

The experimental values of μ were determined by fitting Equation 5.1 for the growth periods (not diluting periods) of turbidostat operation:

$$X = X_0 \exp(\mu t) \qquad \text{Equation 5.1}$$

where X_o is the starting biomass concentration (mg L^{-1}), and X is the biomass concentration (converted to mg L^{-1} from OD_{735}) for a time duration t (days) between X_o and X. The μ and X_o values were obtained by minimizing the sum of squares between the measured X values and modeled X values from Equation 5.1 (Hastie et al., 2009).

The spatially averaged light intensity (LI_{ave}) was obtained by integrating the Beer-Lambert equation and dividing by the reactor's width:

$$LI_{ave} = \frac{LI_0(1-\exp(-\varepsilon X w))}{\varepsilon X w} \qquad \text{Equation 5.2}$$

where ε is the Beer-Lambert extinction coefficient ($m^2\ g^{-1}$), LI_o is the incident light intensity (μmol $m^{-2}\ s^{-1}$), and w is the width of the bioreactor (0.024 m for the FMT).

All steady-state μ values were determined after a minimum 1-day acclimation period at the specified light condition when the previous light condition was higher, 2-days when the previous light condition was lower, and never following a light step that photodamaged PSI. As I show later, 1 day or 2 days were sufficient to establish a photoacclimated state. The reactor vessel occasionally had visible biofilms and flocs, especially with the highest LI_{ave} values and after the largest light steps. When this

occurred, I removed the culture, scrubbed the vessel with bleach and detergent, filtered the culture through sterile cheese cloth, and returned the culture to the reactor vessel. All steady-state data for conditions containing biofilms or flocs was discarded. For light-step experiments, biofilms were promptly removed, and data collection was then resumed.

5.3.2. Parameterizing the Model to the Growth Data

Chapter 4 describes a light-dependent kinetic model for microalgae experiencing photoacclimation, photodamage, and photodamage repair. I summarize the model's equations in Table 5.1, and variables and parameters are defined in Table 5.2.

Table 5.1: Model Equations as Described in Chapter 4, with a List of Variables and Parameters in Table 5.2 (Correspond to Equations 4.1-4.8 in Chapter 4)

$\frac{dLI_p}{dt} = \left(\varepsilon_{abs} LI - \varepsilon_{nf} LI - \left(\frac{k_{LI} LI_p}{k_{LI}+LI_p} + \frac{LI_p^2}{k_{LI}+LI_p}\right) k_{LIp}\right) \frac{86400s}{d}$	Equation 5.3
$\mu = \frac{\mu_{max} LI_p - \varepsilon_{nf} k_b}{k_{LI}+LI_p} - b$	Equation 5.4
$\varepsilon_{abs,ss} = \frac{(\varepsilon_{max} - \varepsilon_{scat} - \varepsilon_{abs,min}) k_\varepsilon}{k_\varepsilon + LI} + \varepsilon_{abs,min}$	Equation 5.5
$\frac{d\varepsilon_{abs}}{dt} = \left(\varepsilon_{abs,ss} - \varepsilon_{abs}\right) {k_{ad}}^{\alpha}$	Equation 5.6
$\frac{d\varepsilon_{nf}}{dt} = LI_p k_{d1} - \frac{\left(k_{r1}\varepsilon_{nf} - k_{r2} LI_p \zeta\right)^{\beta}}{k_{LI}+LI_p}$	Equation 5.7
$\frac{d\zeta}{dt} = \left(\left(\varepsilon_{abs} - \varepsilon_{abs,ss}\right)^{\beta} - (\zeta - \delta) y^{\gamma}\right) \frac{k_{r3}}{\left(k_{r4}+LI_p\right)^2} + k_{d3}(\delta - \zeta)(1 - y^{\gamma})$	Equation 5.8
$\frac{d\delta}{dt} = (\varepsilon_{abs} - \varepsilon_{abs,ss} - \delta - (\varepsilon_{max} - \varepsilon_{scat} - \varepsilon_{abs}) k_{d2})^{\beta} k_{d3}$	Equation 5.9
$\varepsilon_{nf,ss} = \frac{k_{d1}}{k_{r1}} \left(k_{LI} LI_p + LI_p^2\right)$	Equation 5.10

α If $\varepsilon_{abs,ss} > \varepsilon_{abs}$, $k_{ad} = k_{ad,dn}$, else $k_{ad} = k_{ad,up}$
β If term is less than 0, the term is 0
γ If $\zeta > \delta$, y = 1, else y = 0

Table 5.2: Model Variables and Best-Fit Parameters for Model Equations 5.3-5.10

variable		description		units
LI_p		Absorbed light energy		μmol g^{-1}
μ		specific growth rate		d^{-1}
ε_{abs}		photoacclimation and light absorption		m^2 g^{-1}
$\varepsilon_{abs,ss}$		steady-state ε_{abs}		m^2 g^{-1}
y		switch term for Equation 5.8		unitless
ε_{nf}		PSII photodamage		m^2 g^{-1}
ζ		PSII repair inhibition		m^2 g^{-1}
δ		PSI photodamage		m^2 g^{-1}
parameter	equations	description	value	units
k_{LI}	5.3, 5.4, 5.7 & 5.10	light-limited half-maximum-rate absorbed light growth constant	50	μmol g^{-1}
k_{LIp}	5.3	rate constant of light-pool dissipation	1	s^{-1}
μ_{max}	5.4	maximum specific growth rate	12	d^{-1}
k_b		photoinhibition decay constant	1400000	μmol m^{-2} d^{-1}
b		endogenous-decay constant	0	d^{-1}
ε_{max}	5.5	light extinction for biomass photoacclimated to the lowest LI	0.18*	m^2 g^{-1}
ε_{scat}		light extinction from scattering	0.033	m^2 g^{-1}
k_ε		half-maximum light absorption LI	380*	μmol m^{-2} s^{-1}
$\varepsilon_{abs,min}$		minimum light extinction from absorbance	0.012	m^2 g^{-1}
$k_{ad,up}$	5.6	rate constant of photoacclimation (ε_{abs}) for increasing light	13	d^{-1}
$k_{ad,dn}$		rate constant of photoacclimation (ε_{abs}) for decreasing light	2	d^{-1}
k_{d1}	5.7 & 5.10	rate constant of PSII photodamage (ε_{nf})	0.000088	m^2 μmol^{-1} d^{-1}
k_{r1}		rate constant of normal PSII photodamage (ε_{nf}) repair	1600	μmol g^{-1} d^{-1}
k_{r2}	5.7	rate constant for the reduction in PSII photodamage (ε_{nf}) repair	1.3	d^{-1}
k_{r3}	5.8	maximum rate of generation/repair of repair inhibition (ζ)	1600	μmol^2 g^{-2} d^{-1}
k_{r4}		LI_p constant of repair inhibition (ζ)	13	μmol g^{-1}
k_{d2}	5.9	constant of light absorbance where PSI photodamage (δ) occurs	2.6	unitless
k_{d3}	5.8 & 5.9	rate constant of PSI photodamage (δ)	14	d^{-1}

* Values Determined in Chapter 3; A brief discussion relating Equation 5.4 to the results in Chapter 3 is discussed in the Supplementary Material 5.6.2.

Here, I describe how I utilized my experimental data to find best-fit parameter values in a four-step process: 1) fit the rate constants of photoacclimation, 2) compute a theoretical μ_{max}, 3) simultaneous fit all parameters related to PSII photodamage, and 4) fit the parameters for PSI photodamage.

The first step was to fit the rate constants of photoacclimation ($k_{ad,up}$ and $k_{ad,dn}$ for increasing light and decreasing light, respectively), which I did by fitting Equation 5.6 to the measured OD_{680}/OD_{735} ratio as a surrogate for ε_{abs} and OD_{680}/OD_{735} two days after the light-step for $\varepsilon_{abs,ss}$. I used OD_{680}/OD_{735} because it was continually measured by the FMT, whereas ε_{abs} had to be manually measured, and because OD_{680}/OD_{735} has a strong relationship to ε_{abs} under the light spectrum from the FMT (Chapter 3). I modeled each light-step as a time series using Equation 5.6 (Table 5.1) and adjusted the k_{ad} value to minimize the sum of squares between the measured and modeled OD_{680}/OD_{735} (Hastie et al., 2009). These values were then fixed for the remaining parameter fittings.

The second step was to compute the maximum μ (μ_{max}) by relating it to the maximum quantity and turnover-rate of RuBisCo (the enzyme responsible for fixing carbon dioxide):

$$\left(\frac{3\%\ RuBisCo}{Biomass}\right)^{*}\left(\frac{1\ mol\ RuBisCo}{65{,}000 g^{**}}\right)\left(\frac{10\ reactions^{***}}{s-RuBisCo}\right)\left(\frac{30\ g\ CH_2O}{reaction}\right)\left(\frac{86400\ s}{d}\right)=12\ d^{-1}$$

* Approximated based on RuBisCo being 5% of total protein (Losh et al., 2013; Young et al., 2016) and 60% of biomass is protein (Touloupakis et al., 2016)
** Molecular mass of one RuBisCo subunit (Morell et al., 1992)
*** Highest reported rate of Rubisco activity (Ellis, 2010)

This μ_{max} parameter represents a theoretical instantaneous maximum μ and is roughly 5 times higher than my observed steady-state maximum μ (presented in Figure 5.7 and discussed later), because photodamage is always present and lowers the measured μ to below μ_{max}.

The third step was simultaneously fitting the parameters related to PSII photodamage (ε_{nf}), PSII repair inhibition (ζ), and photosynthetic growth (μ), including: the photoinhibition decay constant (k_b), half-maximum-rate growth constant (k_{LI}), endogenous-decay constant (b), minimum ε from absorbance ($\varepsilon_{abs,min}$), rate constant of ε_{nf} (k_{d1}), rate constant of normal ε_{nf} repair (k_{r1}), rate constant for the reduction in ε_{nf} repair (k_{r2}), and rate constant for repair inhibition (k_{r3}). I simultaneously minimized the difference between the data for steady-state experiments and light-step experiments and the corresponding model-output values for those conditions by adjusting the eight parameters. Fitting the model to the experiments having step changes in LI was based on fitting modeled changes in μ over time. The modeled light-step experiments involved creating a time-series using the set of non-linear equations (Equations 5.3 – 5.8) with inputs of the computed LI_{ave} values (computed using Equation 5.2 for the experimental data) before and after the light step. The model outputs for μ were compared at the center time point of each experimental growth period (time interval between dilutions from FMT turbidostat operation). As an example, in the experimental light-step from LI_{ave} = 53 to 186 μmol m^{-2} s^{-1} (displayed as Figure 5.1 and discussed later), a growth time interval from t = 1.09 to 1.14 days had μ = 1.31 d^{-1}. This experimental μ was compared to the modeled μ at t = 1.11 days. Because LI_p represents total light absorbed, the value of k_{LIp} was set to 1 s^{-1} so $k_{LIp}LI_p = \varepsilon_{abs}LI$ under steady-state conditions where $\varepsilon_{abs} >> \varepsilon_{nf}$.

Fitting the model to the steady-state experiments involved modeling the steady-state μ for light absorbed (LI_p; $\varepsilon_{abs}LI/k_{LIp}$) ranging from 0 to 80 μmol g^{-1} and LI values ranging from 0 to 2000 μmol m^{-2} s^{-1}. Using Equation 5.4 ($LI_p = \varepsilon_{abs}LI/k_{LIp}$) and Equation 5.10, the experimental μ could be directly compared to the modeled μ using the experimental ε_{abs} and LI_{ave} (where ε_{abs} was the measured ε values as reported in Chapter 3 minus light extinction from scattering (ε_{scat})). For modeling the steady-state curve of μ

vs. LI, I used ε_{abs} determined from Equation 5.5; therefore, the experimental μ could be directly compared to the modeled μ at the experimental LI_{ave}. The experimental data were one-day-averages for μ.

In all cases (including light-step experiments), the experimental LI_{ave} was the modeled LI. Because of the narrow light path and low OD, the effect of attenuation within the culture was minimized so that LI_{ave} was at least ≥75% of the incident LI.

The sum of squared differences for all the light-step experiments (all experiments with an increasing light-step and without PSI photodamage (11 experiments)) and the growth curves (the comparisons of μ to $\varepsilon_{abs}LI/k_{LIp}$ and μ to LI) were simultaneously minimized by adjusting the fitting parameters (k_b, k_{LI}, b, $\varepsilon_{abs,min}$, k_{d1}, k_{r1}, k_{r2}, and k_{r3}) using Microsoft® Excel 2016 and the solver Add-in (Hastie et al., 2009). The steady-state experiments were weighted (x15) for the fitting, because each data point represented a whole day of data (including 6-18 growth periods per data point depending on LI), and some of the stochastic variability was removed by taking the daily average. If the starting values of the parameters before solver was run (the parameter "guess") were too far from the eventual best fit, solver would return a fit with systematic errors (i.e., the peak and depression following the light-step did not show the expected trend). To avoid this, I started by fitting a single "representative" light-step experiment to get initial parameter values to provide a better "guess" for the final fitting. Following this fitting, I was able to find best-fit model parameter values, which make sense and give a model that works well.

The fourth step was to fit the two parameters related to PSI photodamage (δ): the constant of light absorption where δ occurs (k_{d2}) and rate constant of δ (k_{d3}). I did this by adding results from experiments with extreme light steps that led to PSI photodamage not included in the fitting done for the third step. The sum of squared

differences for all the light-step experiments (all experiments with an increasing light-step including extreme light steps; 14 experiments) were simultaneously minimized by adjusting the fitting parameters k_{d2} and k_{d3} using Microsoft® Excel 2016 and the solver Add-in (Hastie et al., 2009). By including the light-step experiments without obvious PSI photodamage, I ensured k_{d2} was large enough that only extreme light steps led to PSI photodamage, and the fittings in the third step were not compromised. A brief discussion on the development of Equation 5.9 is present in Supplementary Material 5.6.3.

5.4. Results and Discussion

Figure 5.1 shows the experimental and modeled values of μ, the measured OD_{680}/OD_{735} ratio, and modeled ε_{abs} for the light-step experiment with LI_{ave} going from 53 to 186 μmol m^{-2} s^{-1}. The model curves were generated using Equations 5.3-5.9 in Table 5.1 and the parameters in Table 5.2. Similarly, Figure 5.2 displays a light-step experiment with LI_{ave} going from 84 to 737 μmol m^{-2} s^{-1}, Figure 5.3 from 186 to 53 μmol m^{-2} s^{-1}, Figure 5.4 from 272 to 27 μmol m^{-2} s^{-1}, Figure 5.5 from 27 to 317 μmol m^{-2} s^{-1}, and Figure 5.6 from 85 to 1452 μmol m^{-2} s^{-1}. The results from 14 additional light-step experiments are presented in Supplementary Material section 5.6.4 as Figure S5.4 and Figure S5.5. In all cases, the standard error for μ was ≤ 0.12 d^{-1}.

Comparing the OD_{680}/OD_{735} data of light-steps of increasing light (Figures 5.1, 5.2, 5.5, and 5.6) to the light-steps of decreasing light (Figures 5.3 and 5.4) makes it apparent that photoacclimation occurred much more slowly with decreasing LI than increasing LI, and this is reflected in the k_{ad} parameters: $k_{ad,dn}$ = 2 d^{-1}, and $k_{ad,up}$ = 13 d^{-1}.

A feature common to Figures 5.1 and 5.2 is the immediate spike increase in μ after the increasing LI_{ave} step. Immediately after the spike, μ precipitously declined to a value close to that of the preceding LI_{ave}. Then, μ gradually increased and stabilized at a condition representing acclimation to the new LI_{ave}. The sharp spike occurred because the biomass was photoacclimated to a lower LI before the LI change, and, therefore, had a relatively high level of pigmentation for light absorption. Immediately after the increase in LI, the biomass was able to absorb an excess of light energy, which caused a spike in growth for a short time. This advantage quickly dissipated, as the absorption of excess light increased the generation of PSII photodamage and reduced the biomass's ability to repair photodamage, thereby creating an excess of PSII photodamage, which

caused photoinhibition (a decline in μ). Finally, the growth rate restabilized to the new LI through gradual photoacclimation that involved PSII photodamage repair.

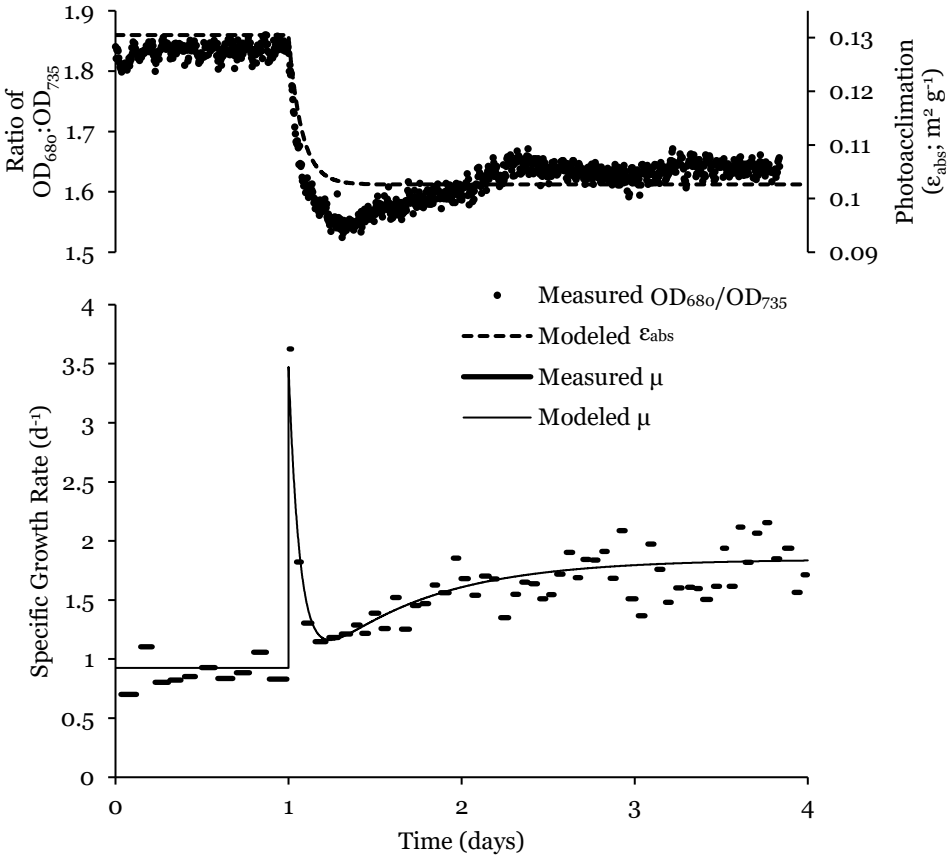

Figure 5.1: Experimental and modeled results of an LI_{ave} step 53 to 186 μmol m^{-2} s^{-1}. The change in LI_{ave} occurred on day 1. The top plot displays the measured OD_{680}/OD_{735} ratio (dots scaled on the left axis) and modeled ε_{abs} (dashed line scaled on the right axis). The bottom plot displays the measured and modeled μ with the wide dashes being measured and narrow line modeled. PSI photodamage did not occur with this light step (δ = 0). Each horizontal dash in the measured μ (bottom panel) represents the average μ over the time period of the dash. The dash for the measured μ immediately after the light-step change is estimated at 3.6 d^{-1}. The model is Equations 5.3-5.8, and its parameters are listed in Table 5.2. The standard error for ε_{abs} was 0.001 OD_{680}/OD_{735} and μ was 0.02 d^{-1}.

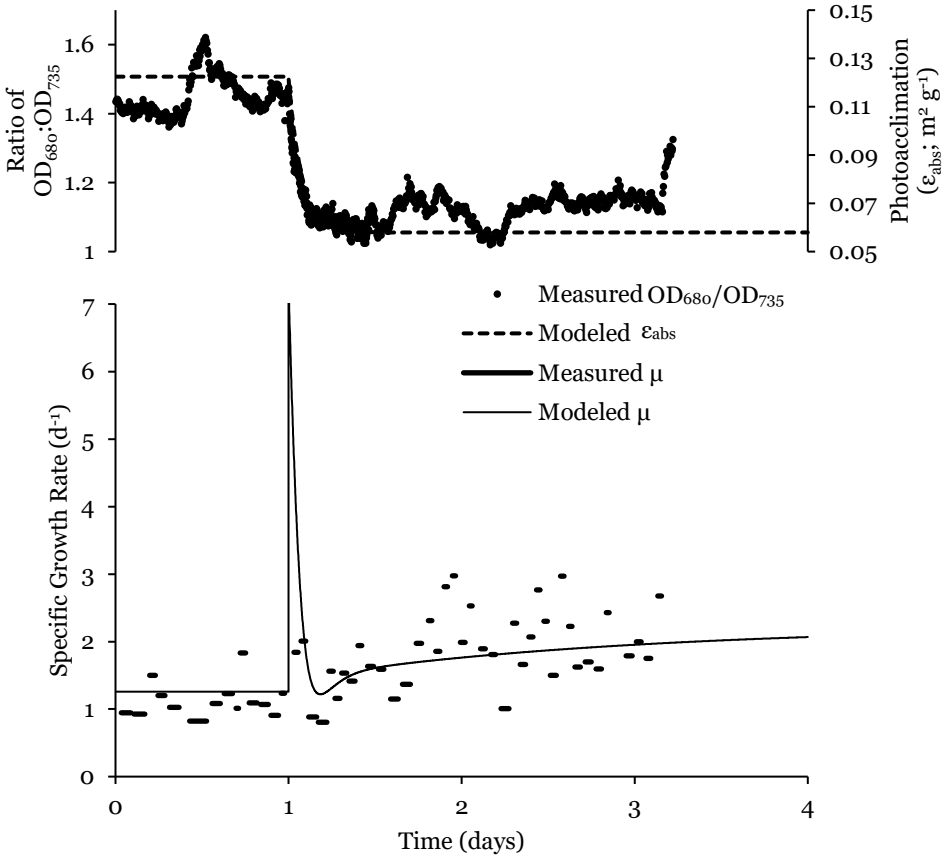

Figure 5.2: Experimental and modeled results of an LI_{ave} step 84 to 737 μmol m^{-2} s^{-1}. The change in LI_{ave} occurred on day 1. The top plot displays the measured OD_{680}/OD_{735} ratio (dots scaled on the left axis) and modeled ε_{abs} (dashed line scaled on the right axis). The bottom plot displays the measured and modeled μ with the wide dashes being measured and narrow line modeled. PSI photodamage was negligible with this light step (modeled at $\delta = 10^{-5}$ at the end of the 4 days). Each horizontal dash in the measured μ (bottom panel) represents the average μ over the time period of the dash. The dash for the measured μ immediately after the light-step change is absent, but was estimated at 20 d^{-1}. The model is Equations 5.3-5.9, and its parameters are listed in Table 5.2. The standard error for ε_{abs} was 0.002 OD_{680}/OD_{735} and μ was 0.09 d^{-1}.

As discussed in section 5.3.2. Parameterizing the Model, the quantification of μ immediately following the light-step changes had a degree of uncertainty; nonetheless, I consistently saw the spike in μ, which ranged from 2 to 25 d^{-1} for all experiments with an increasing light step. Furthermore, the magnitude of the spike in μ was represented well for most experiments by the Monod parameters in Equation 5.4: the theoretically determined μ_{max} = 12 d^{-1}, experimentally determined k_{LI} = 50 μmol g^{-1}, experimentally determined b = 0 d^{-1}, and $\varepsilon_{nf,ss}$ for the initial LI. I could effectively fit all the other growth trends (depression and recovery following the spike in μ) with μ_{max} of 12 d^{-1} and the other parameters. A high μ_{max} value means that, based on C-fixation, *Synechocystis* could grow even faster than I observed, had photodamage been absent. The best-fit k_L value of 50 μmol g^{-1} corresponds to an LI of 1100 μmol m^{-2} s^{-1} (assuming ε_{abs} = 0.046 m^2 g^{-1} based on Equation 5.5), which indicates that the Monod curve does not plateau until well past the LI values tested in this study; therefore, the spike in μ should continue to increase with steps in LI > 2000 μmol m^{-2} s^{-1}. The magnitude of spike, however, also depends on the starting LI and corresponding ε_{nf}.

Because the observed μ dynamics following an increasing light step (the depression and recovery of μ) were captured in the model by changes in ε_{nf}, its value must be mechanistically accurate. The onset of ε_{nf} is proportional to light absorbed, which is represented by k_{d1}. My best fit value of k_{d1} = 0.000088 m^2 μmol^{-1} d^{-1} is consistent with the theory that every photon absorbed has approximately a one-in-a-million chance of causing damage (Anderson et al., 1998). The rate of ε_{nf} repair is proportional to ε_{nf} (at a proportion of k_{r1}; 1600 μmol g^{-1} d^{-1}) and follows an inverse Monod trend to light absorbed. This inverse Monod function utilizes the same half-rate constant as the Monod growth formula (k_{LI} = 50 μmol g^{-1}). At LI = 0, the rate of repair is at its maximum (per ε_{nf}) and is equal to $k_{r1}*\varepsilon_{nf}/k_{LI}$ ($1600*\varepsilon_{nf}/50$ = 32 d^{-1} $*\varepsilon_{nf}$), which is 2.5

times as fast as the rate of photoacclimation for an increasing light-step ($k_{ad,up}$ 13 d^{-1}). The longer depression following the spike in μ, however, is due to a decrease in ε_{nf} repair (repair inhibition; ζ), which occurs proportional to the difference between $\varepsilon_{abs,ss}$ and ε_{abs}. The recovery from ζ lags behind generation, as the rate of generation and recovery are proportional to the level of ζ and a squared inverse-Monod formula with the half rate constant being k_{r3} (k_{r3} = 13 μmol g^{-1} d^{-1}). This relatively low value for k_{r3} indicates that, for higher initial LI light steps (> 200 μmol m^{-2} s^{-1}), ζ has little impact on ε_{nf}. These five parameters (k_{d1}, k_{r1}, k_{LI}, k_{r2}, and k_{r3}) collectively describe the ε_{nf} dynamics following an increasing-light step. Finally, the resulting photoinhibition is proportional to ε_{nf} (at a proportion of k_b; 1400000 μmol m^{-2} d^{-1}) and results in the dip in growth following the spike, and the steady-state growth substantially below μ_{max}.

Comparing Figure 5.1 and Figure 5.2 demonstrates that the impact of the light-step increase was muted for biomass acclimated to a higher LI. The higher initial LI_{ave} in Figure 5.2 (84 vs. 53 μmol m^{-2} s^{-1} in Figure 5.1) had a smaller depression in μ, even though the increase in LI was much greater (653 vs 133 μmol m^{-2} s^{-1}). The muted response in Figure 5.2 occurred because changes in $\varepsilon_{abs,ss}$ can be less with higher initial LI and, therefore, lower ζ.

Figures 5.3 and 5.4 show light steps of decreasing LI. In both cases, μ appeared to decline a modest amount immediately after the light-step, but then gradually increased to the new steady-state. These light-step data cannot explicitly capture the immediate drop and rebound predicted by the model, because the brief negative growth rate would have been averaged with the following positive growth. The growth-rate values were determined only for periods when the turbidostat was not diluting, therefore, once the reactor stopped diluting, the next growth period began. The negative growth would drop the OD_{735}, but this would begin climbing shortly after, and μ would be computed for the entire period between dilutions thereby averaging out the brief negative growth. The depression occurred in part because of the initial (although brief) excess of photodamage and also because the biomass initially could absorb a less-than-optimal amount of light for the new (lower) LI. Thus, the biomass needed to photoacclimate to the lower LI before its new steady-state μ could be reached. Because the biomass needed to rebuild its pigmentation for optimal absorption at the lower LI, photoacclimation, and, thus, recovery of μ, was slow, since $k_{ad,dn}$ is relatively small (2 d^{-1}).

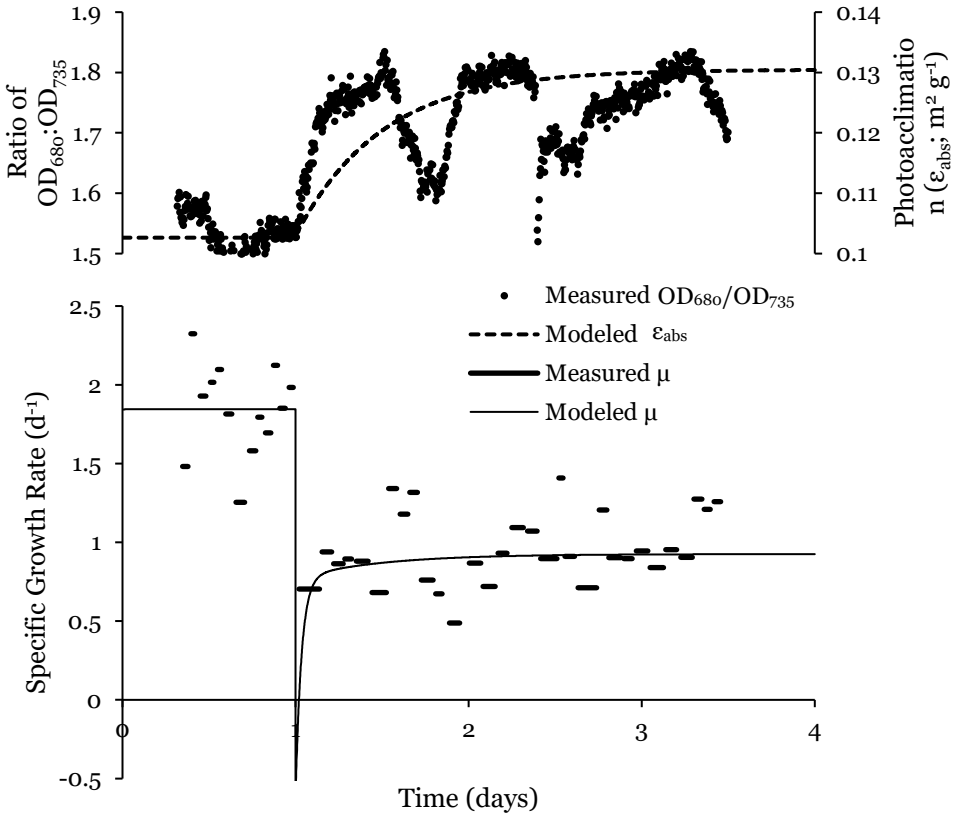

Figure 5.3: Experimental and modeled results of an LI_{ave} step 186 to 53 μmol m^{-2} s^{-1}. The change in LI_{ave} occurred on day 1. The top plot displays the measured OD_{680}/OD_{735} ratio (dots scaled on the left axis) and modeled ε_{abs} (dashed line scaled on the right axis). The bottom plot displays the measured and modeled μ with the wide dashes being measured and narrow line modeled. PSI photodamage did not occur with this light step ($\delta = 0$). Each horizontal dash in the measured μ (bottom panel) represents the average μ over the time period of the dash. The negative growth immediately following the change in light is averaged in with the following measured growth period and therefore not explicitly measured as negative. The model is Equations 5.3-5.7, and its parameters are listed in Table 5.2. The standard error for ε_{abs} was 0.002 OD_{680}/OD_{735} and μ was 0.04 d^{-1}.

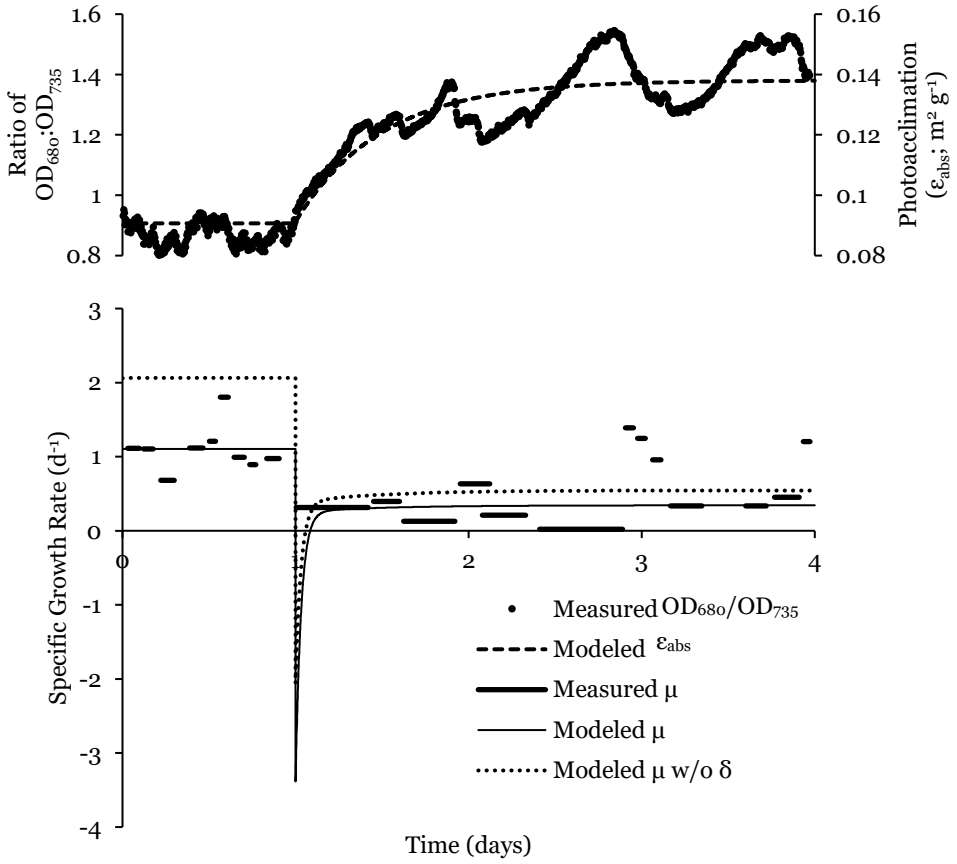

Figure 5.4: Experimental and modeled results of an LI_{ave} step 272 to 27 μmol m^{-2} s^{-1}. The change in LI_{ave} occurred on day 1. The top plot displays the measured OD_{680}/OD_{735} ratio (dots scaled on the left axis) and modeled ε_{abs} (dashed line scaled on the right axis). The bottom plot displays the measured and modeled μ with the wide dashes being measured, narrow line modeled, and dotted line 'Modeled μ w/o δ' where δ is assumed 0. For the first day δ was computed to match the experimental μ. Each horizontal dash in the measured μ (bottom panel) represents the average μ over the time period of the dash. The negative growth immediately following the change in light is averaged in with the following measured growth period and therefore not explicitly measured as negative. The model is Equations 5.3-5.9 (except the 'Modeled μ w/o δ' curve which neglects Equation 5.9), and its parameters are listed in Table 5.2. The standard error for ε_{abs} was 0.002 OD_{680}/OD_{735} and μ was 0.09 d^{-1}.

While the light steps in Figures 5.1 to 5.3 led to no PSI photodamage, the biomass in Figures 5.4 to 5.6 showed obvious signs of PSI photodamage, or $\delta > 0$: μ remained substantially lower than what was predicted for the steady-state condition. The steady-state condition is illustrated by the curve of μ with δ fixed at 0. The effect of PSI photodamage is evident in Figure 5.4 before the light-step, since μ is at around 1.1 d^{-1}, rather than 2.1 d^{-1} as would be expected at steady-state for this LI. After the decreasing light-step, the biomass appears to have a mild decrease of μ compared with the steady-state condition indicative that $\delta > 0$ was still true. For Figures 5.5 and 5.6, signs of $\delta > 0$ occur only after the increasing-light step, and the effects of PSI photodamage persist throughout the 3-day acclimation period.

While Figures 5.5 and 5.6 show generally similar trends to the increasing-light-step experiments in Figures 5.1 and 5.2, except the depression of μ was more severe, and the final steady-state had a lower μ. Comparing Figures 5.5 and 5.6 demonstrates that the impact of the light-step increase remained relatively less severe for biomass acclimated to a higher LI. Even though the light-step in Figure 5.6 was substantially larger than in Figure 5.5 (an increase of 1367 vs 290 μmol m^{-2} s^{-1}), Figure 5.6 shows a proportionally smaller decrease in μ, due to its higher starting LI (85 vs. 27 μmol m^{-2} s^{-1}). This is reflected by the term containing k_{d2} in Equation 5.9 which determines at what point $\delta > 0$ occurs and is dependent on ε_{abs}. Once the onset of $\delta > 0$ starts, as dictated by k_{d3}, it is rapid.

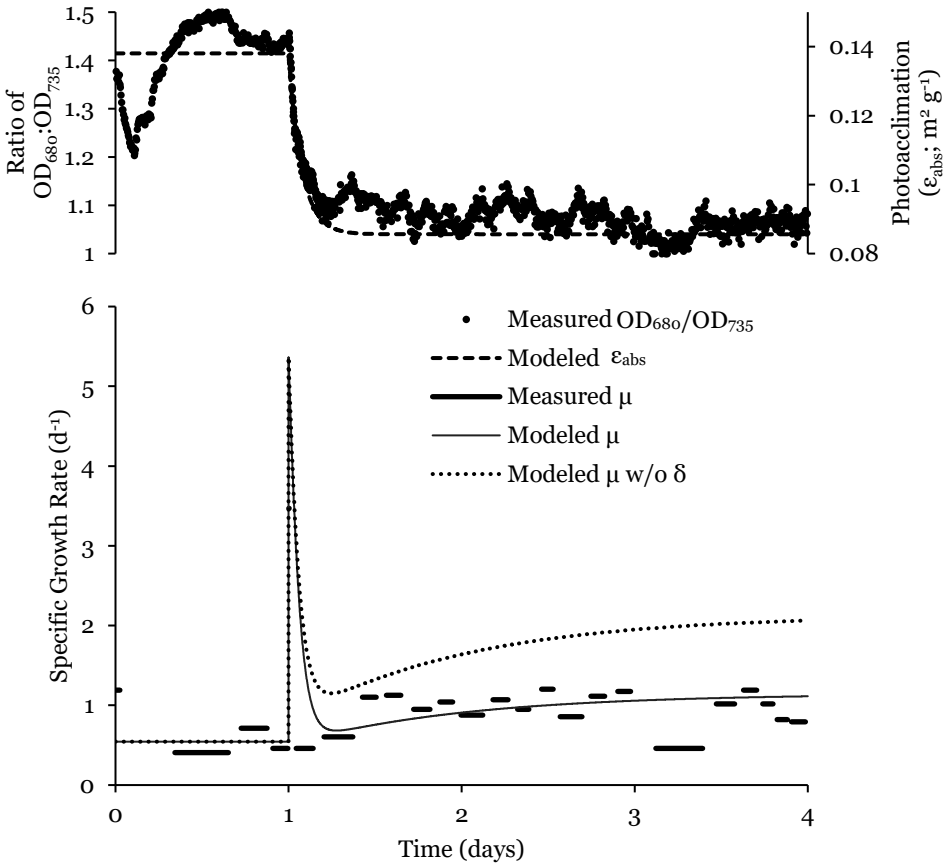

Figure 5.5: Experimental and modeled results of an LI_{ave} step 27 to 317 μmol m^{-2} s^{-1}. The change in LI_{ave} occurred on day 1. The top plot displays the measured OD_{680}/OD_{735} ratio (dots scaled on the left axis) and modeled ε_{abs} (dashed line scaled on the right axis). The bottom plot displays the measured and modeled μ with the wide dashes being measured, narrow line modeled, and dotted line 'Modeled μ w/o δ' where δ is assumed 0. Each horizontal dash in the measured μ (bottom panel) represents the average μ over the time period of the dash. The dash for the measured μ immediately after the light-step change is estimated at 3.5 d^{-1}. The model is Equations 5.3-5.9 (except the 'Modeled μ w/o δ' curve which neglects Equation 5.9), and its parameters are listed in Table 5.2. The standard error for ε_{abs} was 0.001 OD_{680}/OD_{735} and μ was 0.10 d^{-1}.

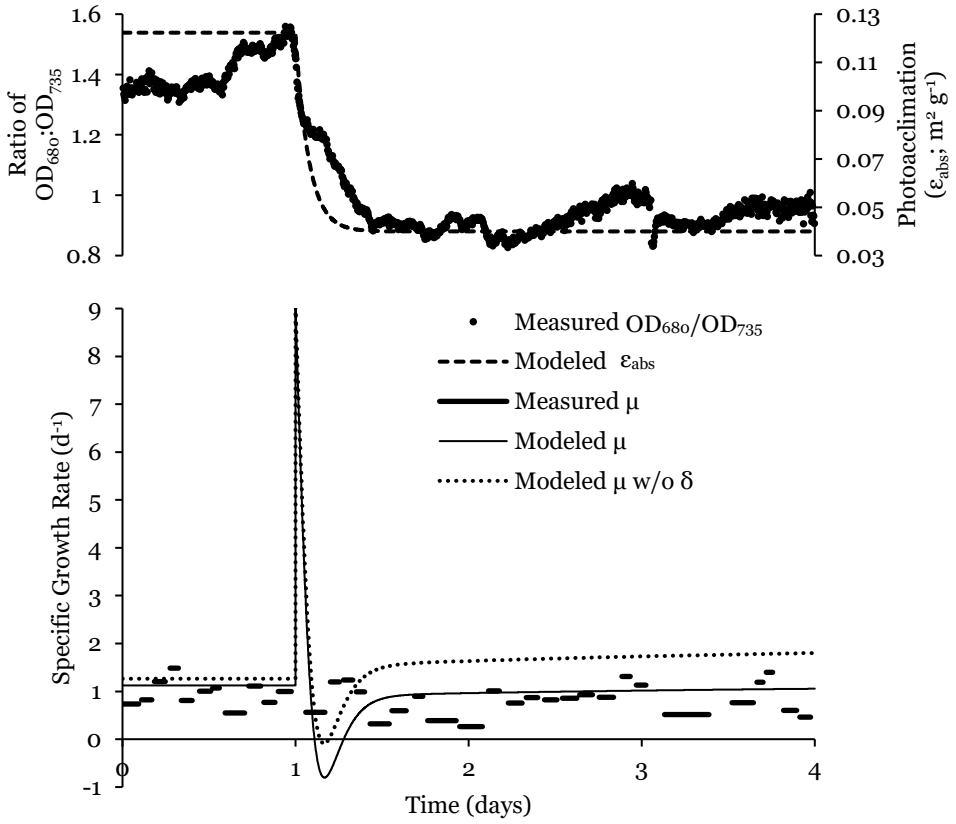

Figure 5.6: Experimental and modeled results of an LI_{ave} step 85 to 1452 μmol m^{-2} s^{-1}. The change in LI_{ave} occurred on day 1. The top plot displays the measured OD_{680}/OD_{735} ratio (dots scaled on the left axis) and modeled ε_{abs} (dashed line scaled on the right axis). The bottom plot displays the measured and modeled μ with the wide dashes being measured, narrow line modeled, and dotted line 'Modeled μ w/o δ' where δ is assumed 0. Each horizontal dash in the measured μ (bottom panel) represents the average μ over the time period of the dash. The dash for the measured μ immediately after the light-step change is absent, but was estimated at 25 d^{-1}. The model is Equations 5.3-5.9 (except the 'Modeled μ w/o δ' curve which neglects Equation 5.9), and its parameters are listed in Table 5.2. The standard error for ε_{abs} was 0.002 OD_{680}/OD_{735} and μ was 0.09 d^{-1}.

Several of the time-series data-sets show an oscillating OD_{680}/OD_{735} ratio and μ, which became pronounced at lower light intensities, such as in Figures 5.3 and 5.4 after the light-step change. Due to the oscillation period of ~24 hours, I hypothesize that this phenomenon was the result of circadian rhythm. Circadian rhythms are well established for *Synechocystis* under diurnal light, but not continuous light (Beck et al., 2014; Saha et al., 2016). However, my results suggest that low light intensity activates some level of circadian effects. The model does not account for circadian effects, but instead smooths out the circadian effects and provides a good approximation of the growth rate over the full 24 hours.

Steady-state growth-irradiance-curves showing μ as a function of $\varepsilon_{abs}LI/k_{LIp}$ and LI are plotted in Figure 5.7. The model considers $\varepsilon_{abs}LI/k_{LIp}$ as the energy-producing "substrate," and Figure 5.7A makes a direct comparison between the measured μ and the measured values of ε ($\varepsilon_{abs} = \varepsilon - \varepsilon_{scat}$) and LI_{ave}. Including the measured ε adds a degree of sensitivity that can have large effects on the total light absorbed, particularly at higher LI, where a small change in ε could mean a substantial increase in $\varepsilon_{abs}LI/k_{LIp}$. An alternate "substrate" is simply LI_{ave} (a more traditional growth-irradiance or photosynthesis-irradiance (PI) curve), where the measured ε is not considered. This is Figure 5.7B. This curve exhibits a steeper increase in μ at low LI because it accounts for the double effects of LI and higher ε at low LI. I used $\varepsilon_{abs}LI/k_{LIp}$ and LI to fit the model parameters, and, therefore, both curves show a good fit to the data. The best fit value for b is 0 because my measured data appears to approach 0 instead of something below 0 as LI_{ave} approaches 0. The observed maximum steady-state μ is about 2.3 d^{-1} (doubling time of ~ 7.2 hours), and it occurs at 38 μmol g^{-1} s^{-1} (Figure 5.7A) or 680 μmol m^{-2} s^{-1} (Figure 5.7B). Yu et al. (2015) cites a 6.6-hour doubling time for *Synechocystis* with incident LI of 300 μmol m^{-2} s^{-1} LI (Yu et al., 2015).

A key parameter for describing the diminishing impact of photoinhibition on μ as LI becomes very large is the minimum attenuation due to absorbance, represented by $\varepsilon_{abs,min}$ (0.012 m^2 g^{-1}). As LI becomes very large, ε_{abs} approaches $\varepsilon_{abs,min}$; therefore, $\varepsilon_{abs,min}$ is the proportional increase in $\varepsilon_{abs}LI/k_{LIp}$ compared to LI at very high LI, and $\varepsilon_{abs}LI/k_{LIp}$ directly impacts ε_{nf}. Thus, a larger $\varepsilon_{abs,min}$ value would indicate higher $\varepsilon_{abs}LI/k_{LIp}$ and higher corresponding photoinhibition at very high LI.

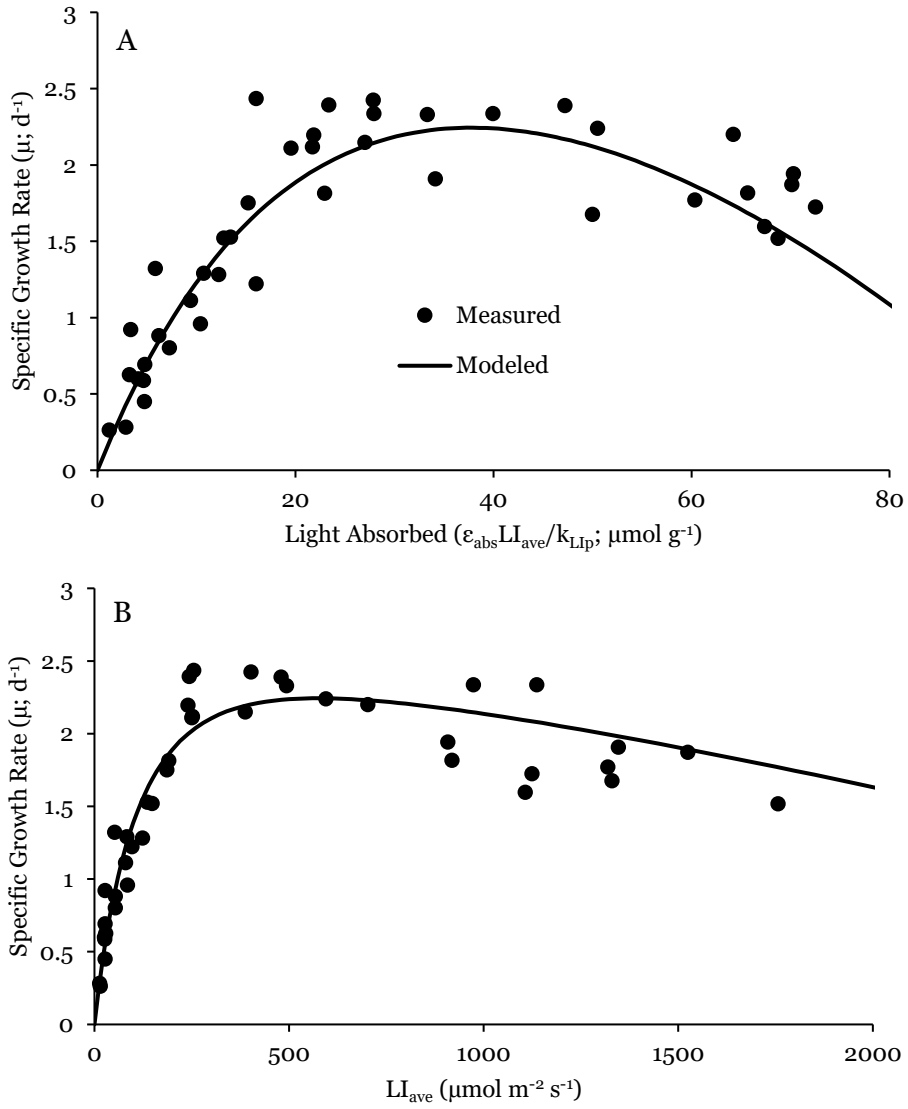

Figure 5.7: Modeled and experimental steady-state growth-irradiance curves across a range of light absorbed (plot A) and LI (plot B). Experimental data are one-day averages taken under non-PSI-damaged conditions ($\delta = 0$). Experimental light absorbed (plot A) is taken as experimental ε minus ε_{scat} multiplied by LI_{ave}. Modeled curves use Equations 5.3-5.5 and 5.10, and parameters listed in Table 5.2. The standard error is 0.04 and 0.03 d^{-1} for the curve in plot A and B respectively.

5.5. Conclusions

I used a series of light-step experiments to parameterize and evaluate the model presented in Chapter 4 (and summarized in Tables 5.1 and 5.2). The model represented all the experimentally observed growth phenomena: the spike and depression in growth rate following an increasing light step, the temporary depression in growth rate following a decreasing light step, and the shape of the steady-state growth-irradiance curve. The parameters I obtained for the model in this study are mechanistically realistic and provide improved insight into modeling microalgae growth under changing light conditions. From numerous light-step experiments, I demonstrated that the photoacclimated light condition plays a large role in susceptibility to photoinhibition. A higher acclimated LI made the biomass less susceptible to photoinhibited phenomena. I also demonstrated that an extreme increasing light step leads to severe photoinhibition, which I suggest is from PSI photodamage.

5.6. Supplementary Material

5.6.1. Comparison of DW to OD_{735} for a light-step increase

Figure S5.1 displays a measured time series of dry weight (DW) measurements and OD_{735} over an LI_{ave} step from 84 to 737 μmol m^{-2} s^{-1}. Before the light step, DW and OD_{735} fluctuate small amounts (roughly ±40 mg L^{-1} and ±0.007 units, respectively). Immediately after the light change, OD_{735} sharply increases, while DW sharply decreases. This lasts 8 minutes before the culture is diluted. During the dilution, OD_{735} declines, but DW increases slightly, which computes to a specific growth rate of 69 d^{-1} when considering the dilution. Following the dilution, DW and OD_{735} show comparable growth rates that are higher than the steady-state μ predicated at this LI, indicative of the tail end of the spike in growth.

The trend represented here occurred in other experiments, with trends in OD_{735} and DW diverging for up to 10 minutes, after which the trends agree again. I do not have a good understanding of what causes the divergence for the short period of time immediately following the step in light. Because of this inconsistency, I attempt to quantify the magnitude of the spike in μ using a combination of the theoretical determination of μ_{max}, and OD_{735} data.

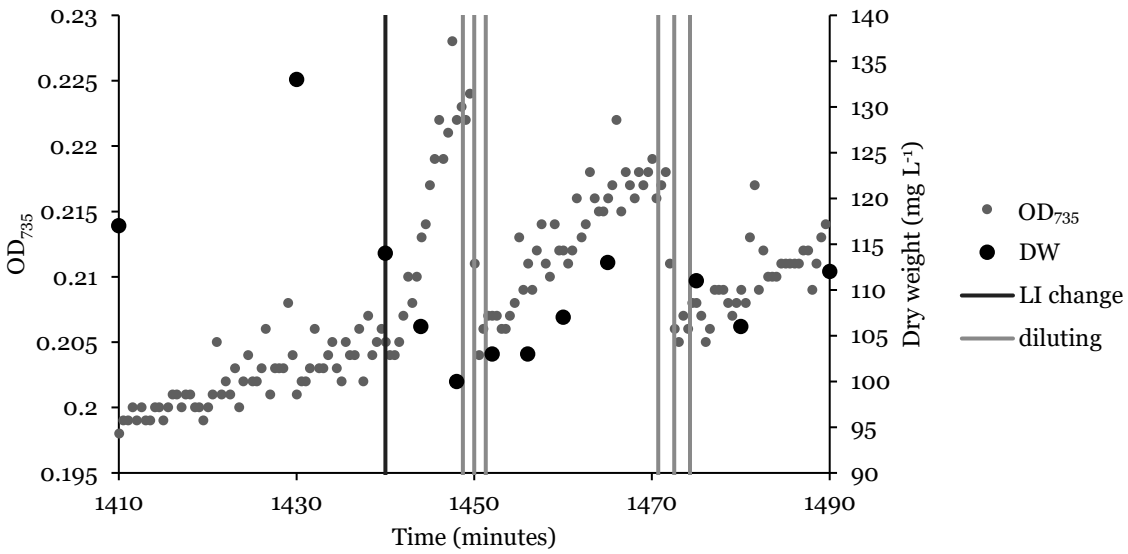

OD_{735} determined μ (d^{-1})	20.5	4.6
DW determined μ (d^{-1})	-23.7	6.4
Modeled (d^{-1})	7.2	6.6

Figure S5.1: Measured DW and OD_{735} during a LI_{ave} step from 84 to 737 μmol m^{-2} s^{-1}. The change in LI_{ave} occurred at 1440 minutes (1 day). The closely spaced horizontal lines denote periods where the culture was manually diluted to maintain the biomass concentration approximately constant (the dilution was done manually to expedite the dilution whereas the FMT typically automatically performed dilutions). Beneath the plot, μ is listed as determined by OD_{735}, DW, and modeled (using the equations and parameters listed in Tables 5.1 and 5.2) for the period after the light change to the first dilution and between the first and second dilution.

5.6.2. ε_{abs} Curve

The values reported in Chapter 3 are ε_{max} = 0.18 $m^2\ g^{-1}$, ε_{min} = 0.045 $m^2\ g^{-1}$, and k_ε = 380 μmol $m^{-2}\ s^{-1}$ for the following equation:

$$\varepsilon = \frac{(\varepsilon_{max}-\varepsilon_{min})k_\varepsilon}{k_\varepsilon+LI_{acc}} + \varepsilon_{min} \qquad \text{Equation 3.3}$$

Relating this to the adjusted formulation I use here, where ε_{abs} (Equation 5.5) + ε_{scat} = ε, gives:

$$\varepsilon = \frac{(\varepsilon_{max}-\varepsilon_{scat}-\varepsilon_{abs,min})k_\varepsilon}{k_\varepsilon+LI} + \varepsilon_{abs,min} + \varepsilon_{scat}$$

The difference is that $\varepsilon_{abs,min}$ + ε_{scat} from this model corresponds to ε_{min} in Chapter 3. In Chapter 3, I considered ε_{min} to be light extinction due only to scattering, making $\varepsilon_{abs,min}$ = 0. Having $\varepsilon_{abs,min}$ = 0 is inconsistent with my experimental results in this Chapter, in which the photoinhibition region of the growth-irradiance curve continues to curve down indicative of additional LI absorption and therefore additional ε_{nf}. Therefore, for the model, I used $\varepsilon_{abs,min}$ + ε_{scat} = 0.012 $m^2\ g^{-1}$ + 0.033 $m^2\ g^{-1}$ = 0.045 $m^2\ g^{-1}$, which divides ε_{min} from Chapter 3 into $\varepsilon_{abs,min}$ and ε_{scat}. Figure S5.2 displays the relation of ε_{abs} to LI using the parameters used in this Chapter.

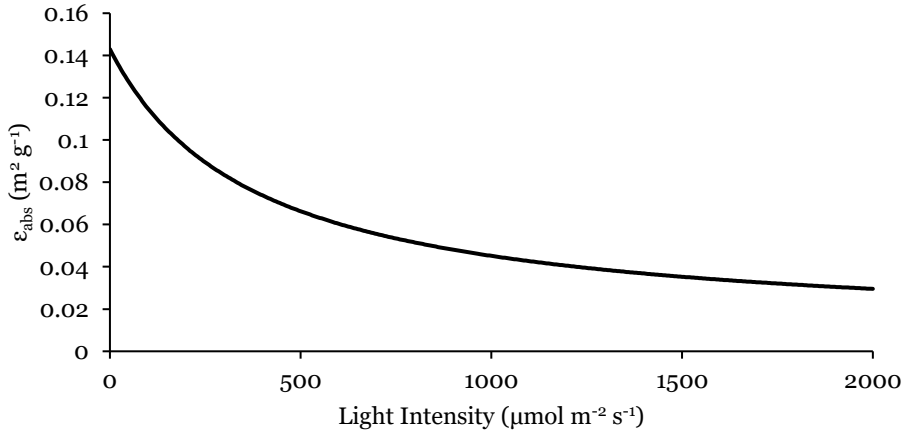

Figure S5.2: Modeled steady-state light absorbance extinction coefficient (ε_{abs}) as a function of light intensity as described by Equation 5.5 and parameters listed in Table 5.2.

5.6.3. Calculating δ from an observed μ (μ_{obs})

I utilized the observed one-day-average-μ values two days after the extreme light step (μ_{obs}) and back-calculated the δ (assuming ζ = δ) caused by that extreme light step by rearranging equations 5.4 and 5.7, while keeping all other parameters constant:

$$\varepsilon_{nf,obs} = \frac{\mu_{max} LI_p - \mu_{obs}(k_{LI} + LI_p)}{k_b}$$

$$\delta_{obs} = \frac{\left(k_{r1}\varepsilon_{nf,obs} - LI_p k_{d1}(k_{LI} + LI_p)\right)}{k_{r2} LI_p}$$

Plotting the calculated δ_{obs} values against the change in ε_{abs} allowed me to visualize the patterns of δ. This is plotted in Figure S5.3.

From this analysis, it is clear that the initial ε_{abs} played a role in the point at which δ > 0 began occurring. I found the relation to ε_{abs} fit the formulation appropriately.

$$\frac{d\delta}{dt} = \left(\varepsilon_{abs} - \varepsilon_{abs,ss} - \delta - (\varepsilon_{max} - \varepsilon_{scat} - \varepsilon_{abs})k_{d2}\right)k_{d3} \qquad \text{Equation 5.9}$$

This is represented by the modeled curves in Figure S5.2, where I modeled time-series results using Equations 5.3-5.9 and plotted the resulting δ three days after (long after δ stopped changing) the light-steps. For δ less than 0.001 $m^2\ g^{-1}$, I considered within reasonable variation and not a reliable indication of PSI photodamage. I would also note that I concluded that the highest point starting from 85 μmol $m^{-2}\ s^{-1}$ (the experiment presented as Figure 5.6) had δ > 0 before the light step in addition to what happened after, making the point appear much higher than the model predicts.

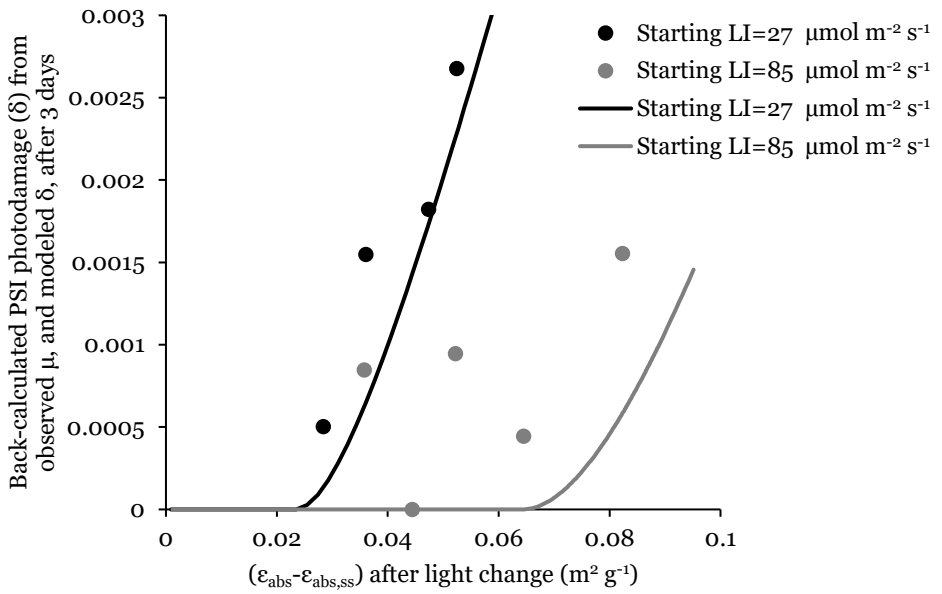

Figure S5.3: PSI photodamaged (δ) calculated from the observed steady-state specific growth rate two days after a light-step using Equations 5.4 and 5.7 as rearranged above and parameters in Table 5.2. The starting LI_{ave} are plotted in different shades and lines are the model and points the data, and the x-axis is the difference between the initial ε_{abs} and $\varepsilon_{abs,ss}$ at the new LI. The curves are modeled δ three days after the light-step using Equations 5.3-5.9.

5.6.4. Results from additional LI_{ave}-step experiments

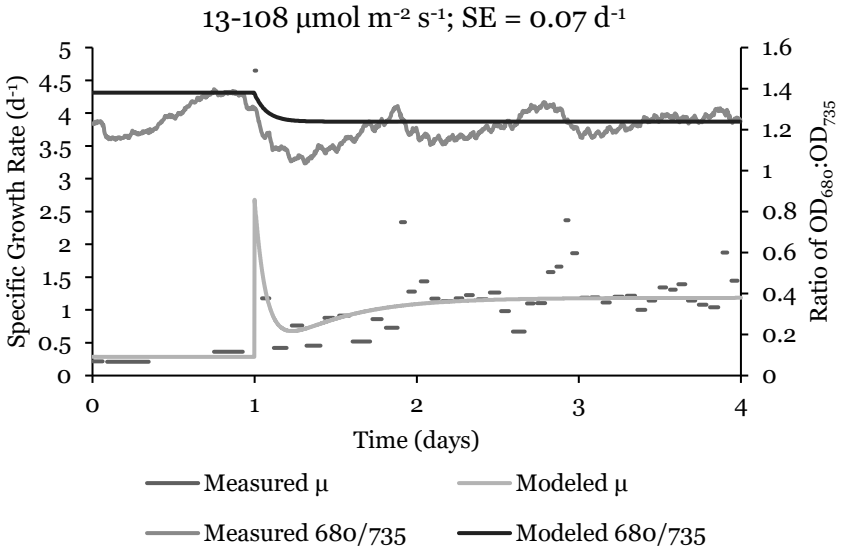

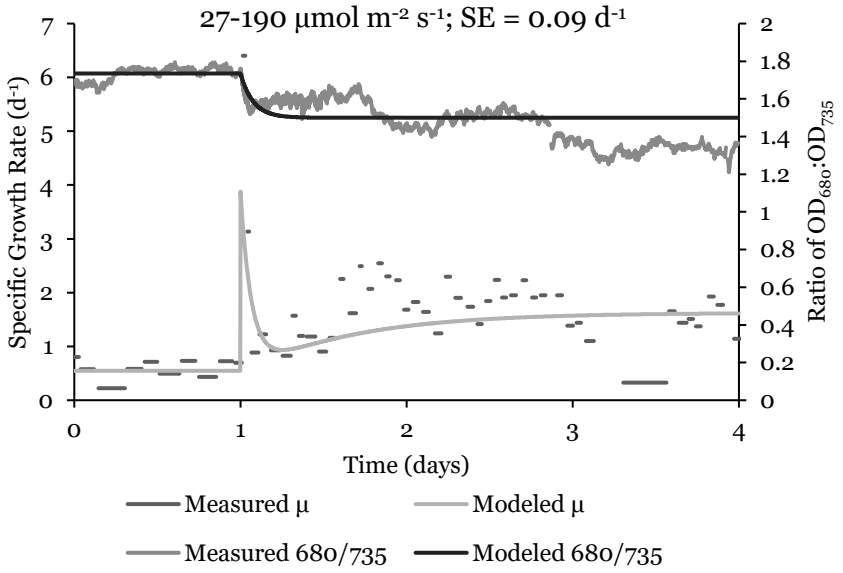

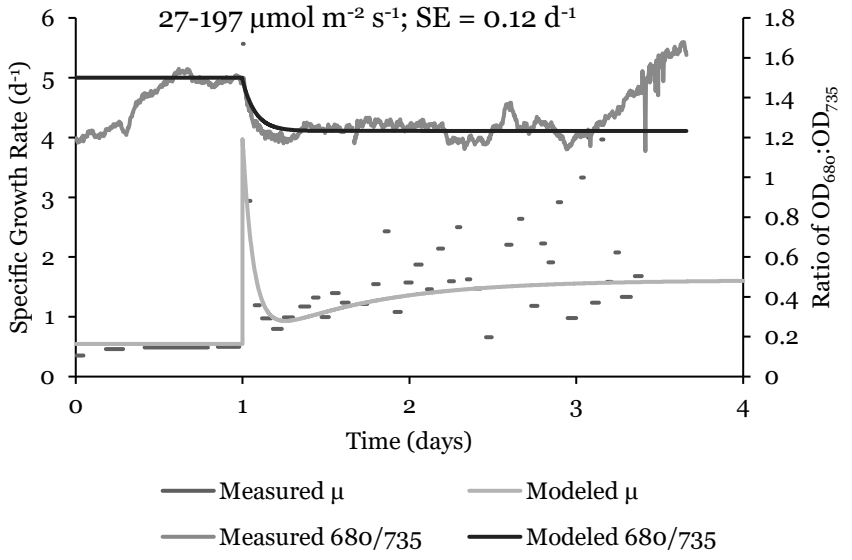
27-197 µmol m-2 s-1; SE = 0.12 d-1
Specific Growth Rate (d-1)
Ratio of OD680:OD735
Time (days)
Measured µ
Modeled µ
Measured 680/735
Modeled 680/735

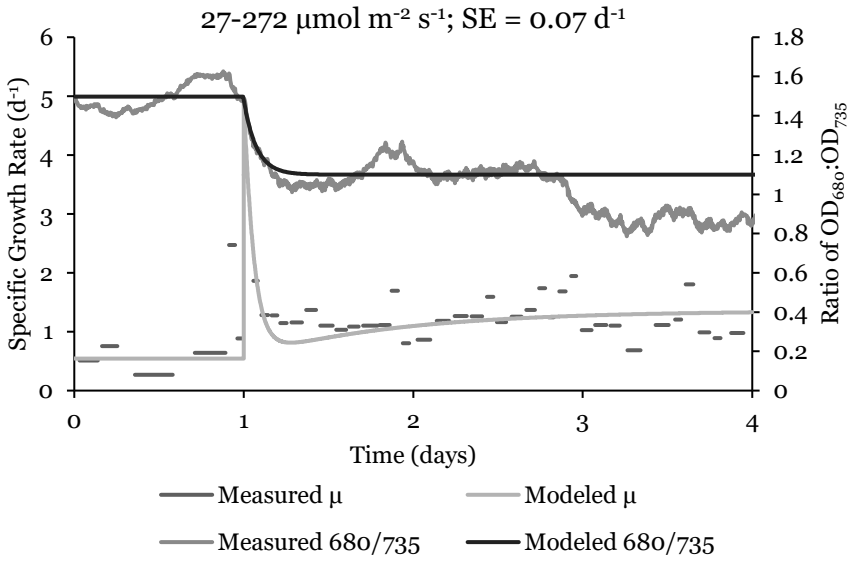
27-272 µmol m-2 s-1; SE = 0.07 d-1
Specific Growth Rate (d-1)
Ratio of OD680:OD735
Time (days)
Measured µ
Modeled µ
Measured 680/735
Modeled 680/735

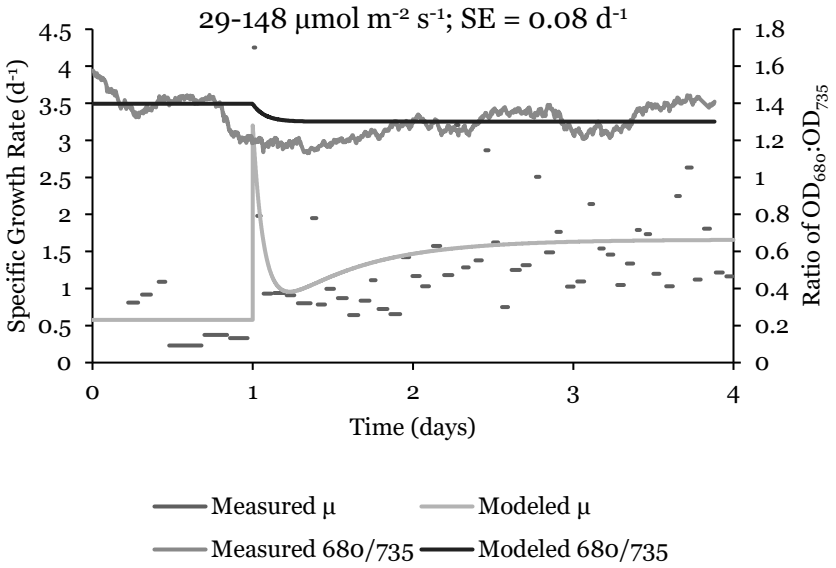
29-148 µmol m-2 s-1; SE = 0.08 d-1
Specific Growth Rate (d-1)
Ratio of OD680:OD735
Time (days)
Measured µ
Modeled µ
Measured 680/735
Modeled 680/735

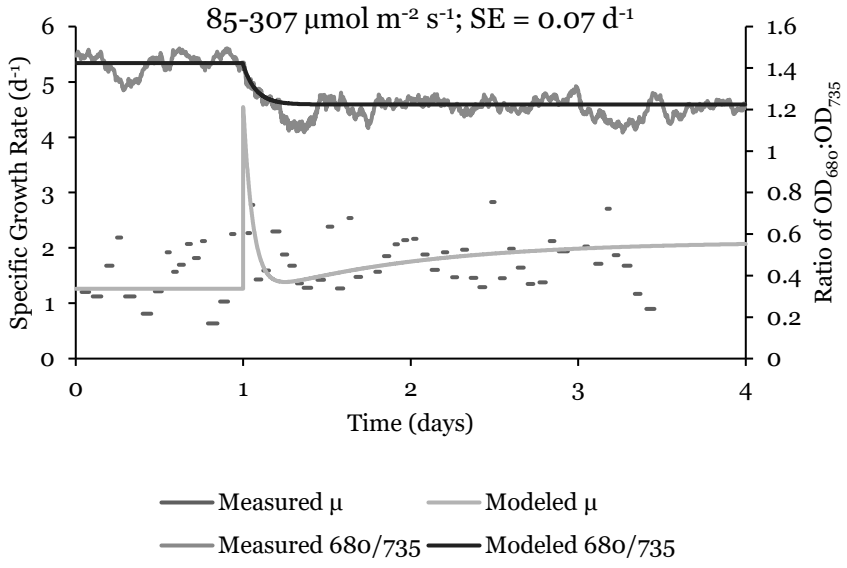
85-307 µmol m-2 s-1; SE = 0.07 d-1
Specific Growth Rate (d-1)
Ratio of OD680:OD735
Time (days)
Measured µ
Modeled µ
Measured 680/735
Modeled 680/735

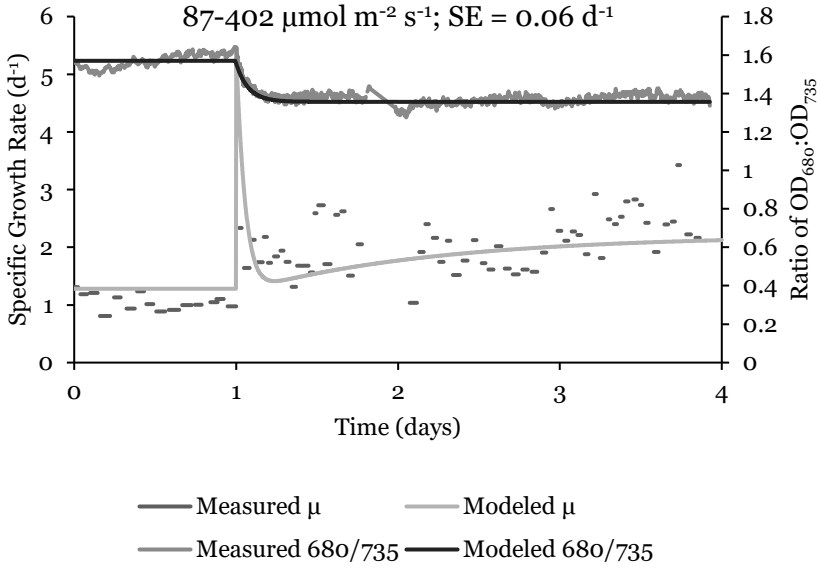
87-402 µmol m-2 s-1; SE = 0.06 d-1
Specific Growth Rate (d-1)
Ratio of OD680:OD735
Time (days)
Measured µ
Modeled µ
Measured 680/735
Modeled 680/735

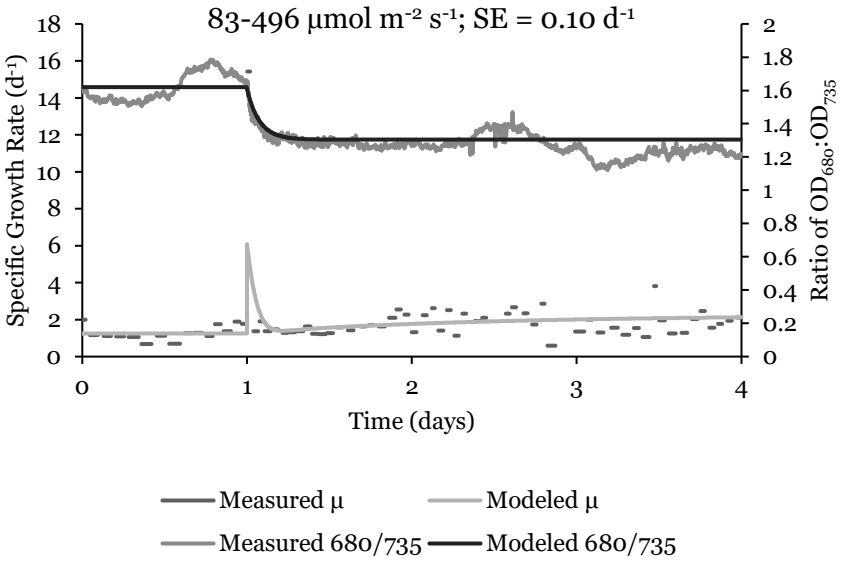
83-496 µmol m-2 s-1; SE = 0.10 d-1
Specific Growth Rate (d-1)
Ratio of OD680:OD735
Time (days)
Measured µ
Modeled µ
Measured 680/735
Modeled 680/735

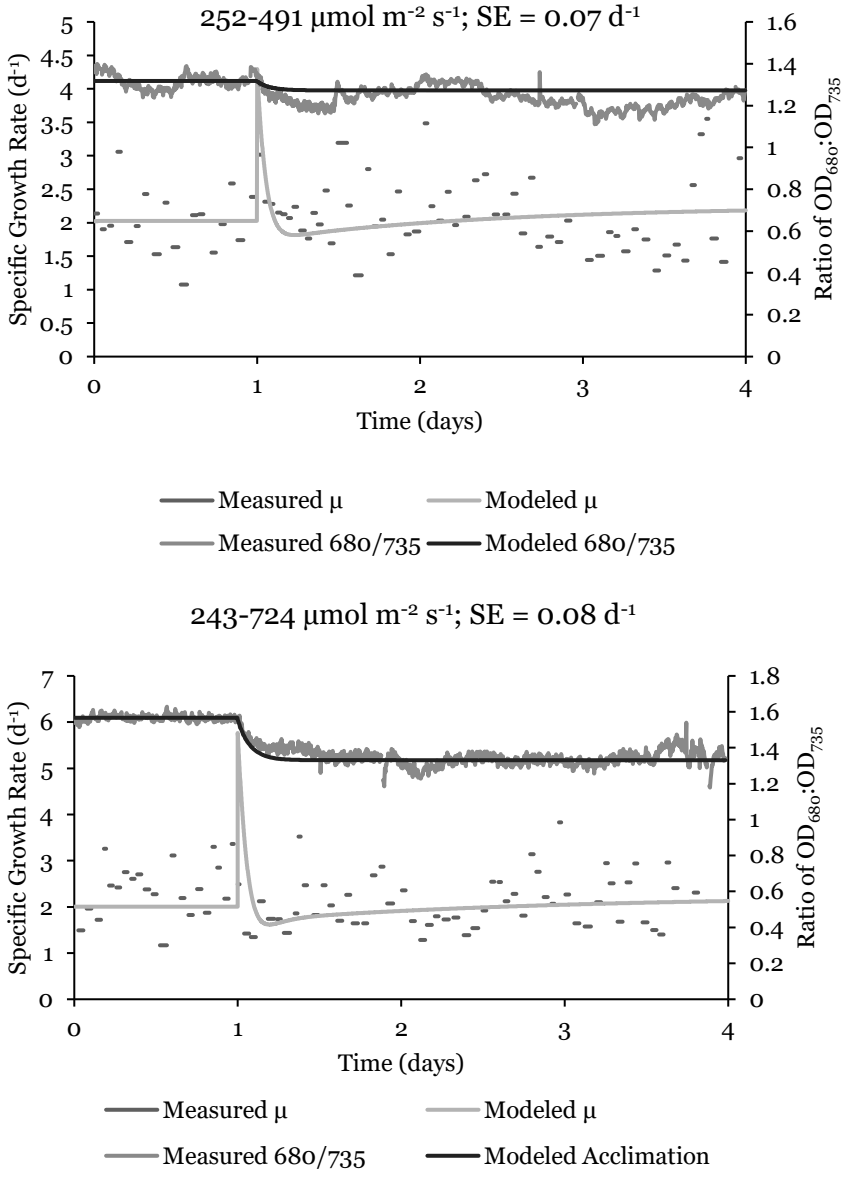

Figure S5.4: Experimental and modeled results for additional increasing LI_{ave} steps with the magnitude of the step (µmol m^{-2} s^{-1}) and standard error (SE; d^{-1}) between the model and experimental µ listed at the top of each plot. Each plot displays modeled and measured OD_{680}/OD_{735} (right axis) and µ (left axis). The change in LI_{ave} occurs on day 1. Each horizontal dash in the measured µ represents the average µ over the time period of the dash. The modeled µ is generated using Equations 5.3-5.9, modeled OD_{680}/OD_{735} using Equation 5.6 (substituting OD_{680}/OD_{735} for ε_{abs}) and parameters are listed in Table 5.2. In order of plots the first recorded µ following the light-step change is: 3.7, 6.4, 5.6, 3.7, 4.3, 5.2, 2.3, 15.4, 3.0, and 2.5 d^{-1}. Only the light step from 13-108, and 27-272 µmol m^{-2} s^{-1} were modeled with $\delta > 0$.

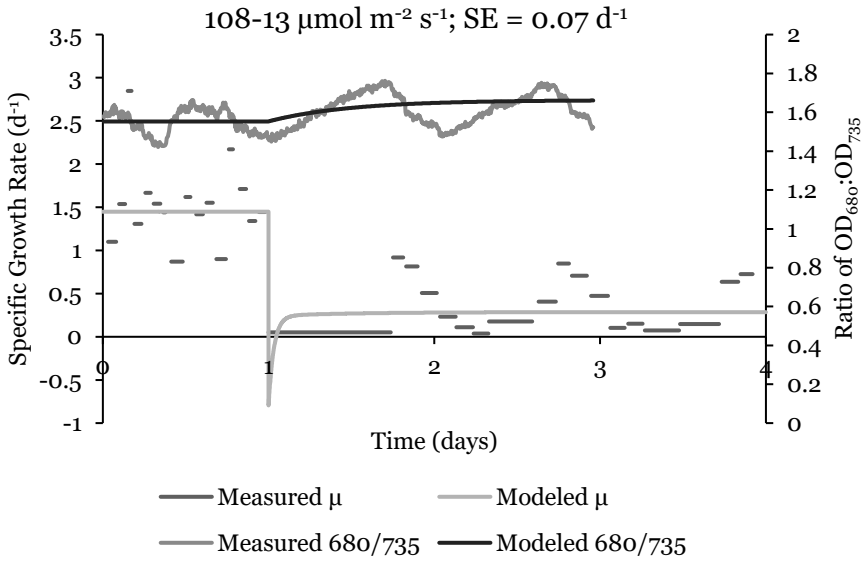
108-13 µmol m-2 s-1; SE = 0.07 d-1
Specific Growth Rate (d-1)
Ratio of OD680:OD735
Time (days)
Measured µ
Modeled µ
Measured 680/735
Modeled 680/735

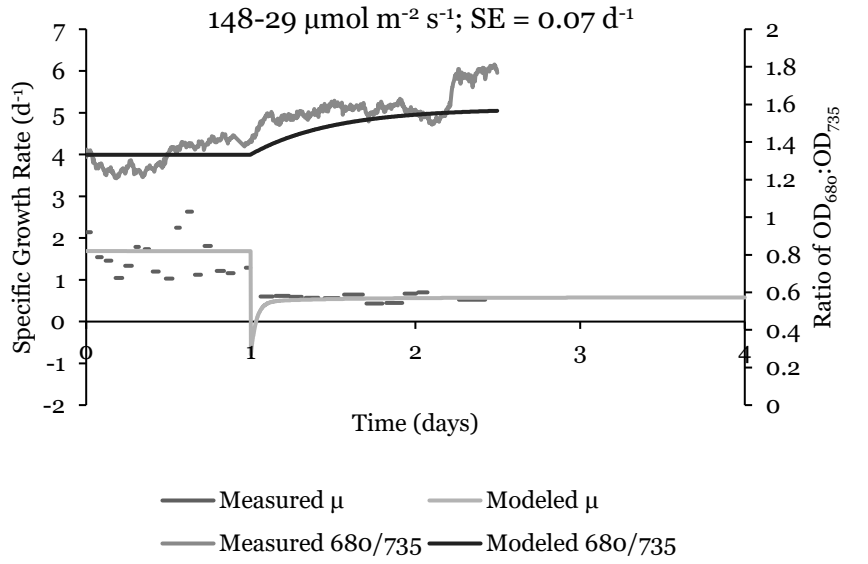
148-29 µmol m-2 s-1; SE = 0.07 d-1
Specific Growth Rate (d-1)
Ratio of OD680:OD735
Time (days)
Measured µ
Modeled µ
Measured 680/735
Modeled 680/735

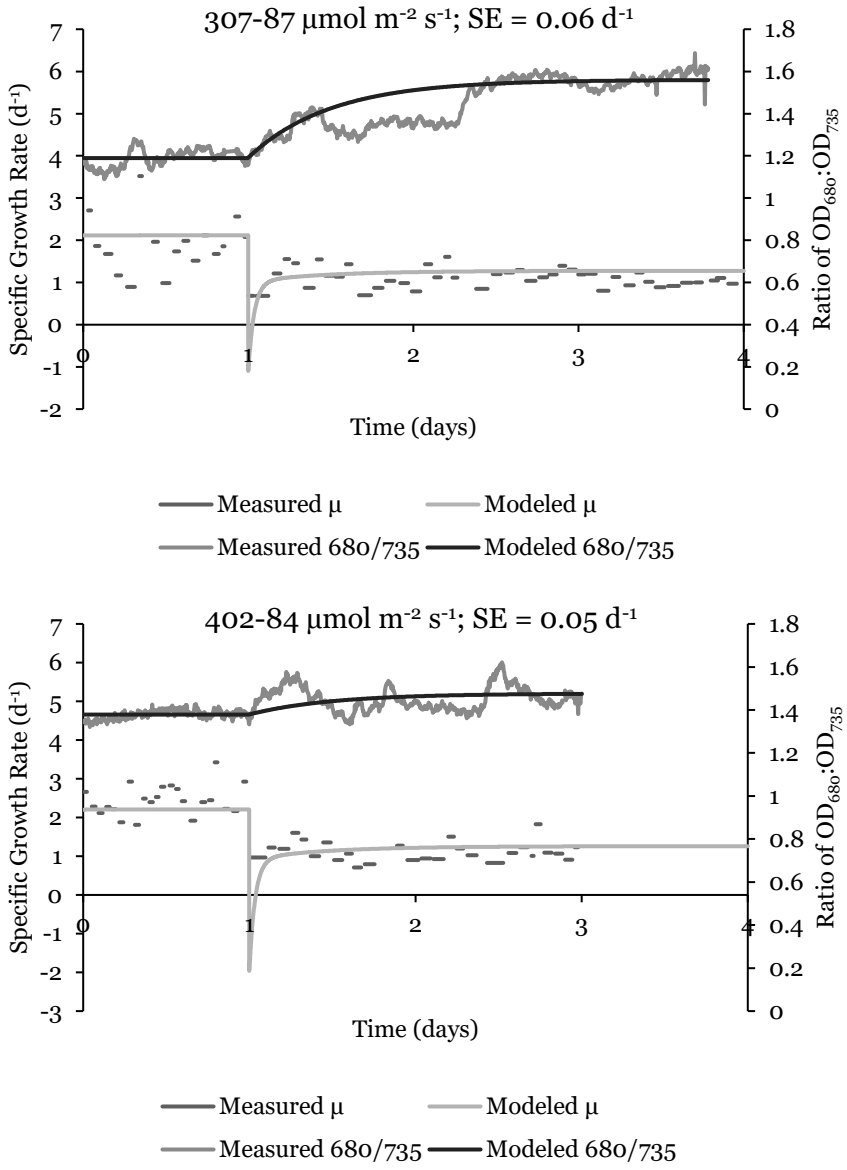

Figure S5.5: Experimental and modeled results for additional decreasing LI_{ave} steps with the magnitude of the step (µmol m^{-2} s^{-1}) and standard error (SE; d^{-1}) between the model and experimental µ listed at the top of each plot. Each plot displays modeled and measured OD_{680}/OD_{735} (right axis) and µ (left axis). The change in LI_{ave} occurs on day 1. Each horizontal dash in the measured µ represents the average µ over the time period of the dash. The modeled µ is generated using Equations 5.3-5.7, modeled OD_{680}/OD_{735} using Equation 5.6 (substituting OD_{680}/OD_{735} for ε_{abs}) and parameters are listed in Table 5.2.

6. GROWTH KINETICS AND MATHEMATICAL MODELING OF *SYNECHOCYSTIS* SP. PCC 6803 EXPOSED TO FLASHING LIGHT

6.1. Abstract

In photobioreactors and natural systems, microalgae are subjected to rapidly changing light intensities (LI) due to light attenuation and mixing. A controlled way to study the effect of rapidly changing LI is to subject cultures to flashing light. In this study, series of flashing-light experiments were conducted using *Synechocystis* sp. PCC6803, and the results were compared to modeled results using a mathematical model that includes an absorbed pool of light energy, photoacclimation, and photoinhibition. In all cases, the overall average LI was ~84 μmol m^{-2} s^{-1}, and the relative times in the light and in the dark were varied. With equal time in light and dark, the specific growth rate (μ) systematically decreased with increasing light duration, and μ decreased further when the ratio of light to dark was decreased. The model captured both trends and provided a mechanistic explanation for them. When the light duration was very short, the changes in the pool of absorbed LI were smoothed out across the light and dark periods, whereas longer durations caused the biomass to experience discrete light and dark conditions that lead to reduced light absorption, more energy loss to non-photochemical quenching, and more photodamage. These growth effects were accentuated as the ratio of light to dark decreased, because this further increased the range of the absorbed light pool that *Synechocystis* experienced. The experimental data and model results had some systematic discrepancies that can be attributed to multiple rate-limiting pools of electron-carrying intermediates during photosynthesis.

6.2. Introduction

As the concentration of a culture of microalgae (collectively referring to single-celled algae and cyanobacteria) increases, the biomass is subject to larger swings in local light intensity (LI) as it moves from areas of high LI (near the light source) to low or no LI (in the interior of a photobioreactor or depths of a lake) (Janssen et al., 2001; Straka and Rittmann, 2017). The effect that rapid changes in local LI have on the microalgae's phototrophic growth rate is not obvious, because the cells' statuses in terms of photoacclimation and photodamage are continually changing (reviewed in Chapter 4). While it has been documented for certain circumstances that higher photosynthetic efficiencies can be achieved using fluctuating light, compared with constant light, the effectiveness of fluctuating LI depends on the rate at which LI is changing and on LI itself (Abu-Ghosh et al., 2016; Grobbelaar, 2010).

One approach for studying the effects of LI swings on microalgae is to subject the biomass to short periods of illumination with dark periods between, known as flashing light (Abu-Ghosh et al., 2016; Kok, 1956b; Vejrazka et al., 2011). The LI flashes represent the movement between the front of the reactor (fully illuminated area) and the back of a reactor (shaded dark area). When the biomass concentration is dilute so that LI is nearly uniform within the culture, the entire biomass can be studied for the effects of fluctuating LI.

A flashing-light experiment can be characterized by three parameters: intensity of the flash (LI_o), the flash time (t_l), and the dark time (t_d). From them, one can derive the duty cycle (fraction of time in light; $\phi = t_l/(t_l+t_d)$), the average incident light intensity ($LI_{aveo} = LI_o*\phi$), and the flash frequency ($f = 1/(t_l+t_d)$) (Abu-Ghosh et al., 2016; Grobbelaar, 2010; Vejrazka et al., 2011). Previous work has shown that flashes having sub-second light-dark cycles ($f > 1\ s^{-1}$) led to higher photosynthetic efficiency than

constant light of the same LI, as long as LI was saturating, or in the section of the growth-irradiance curve where additional light did not accelerate the growth rate (Janssen et al., 2001; Vejrazka et al., 2011). However, similar studies found that longer flashes ($f < 0.2\ s^{-1}$) gave lower photosynthetic efficiency (Janssen et al., 1999, 2000).

In addressing rapidly changing light for mathematical modeling, what becomes important is capturing the rates of the photosynthetic reactions. Light absorption takes on the order of 10^{-15} to 10^{-9} s, electron transport is on the order of 10^{-9} to 10^{-4}s, CO_2 fixation is on the order of 10^{-4} to 1 s, and cell division takes 1 to 10^3 s (Kamen, 1963). While these reactions are sufficiently fast to be neglected for diurnal or continuous light, flashing light or rapidly changing light due to intense mixing needs to consider a mechanism that "pools" the key intermediates that drive the physiological reactions. The model developed by Vejrazka et al., (2015) accounted for flashing light by including a pool of reduced electron equivalents. My model, presented in Chapter 4, included a pool of absorbed light energy (LI_p), which then drives phototrophic growth.

In this study, I conducted a series of flashing-light experiments using the cyanobacterium *Synechocystis* sp. PCC 6803 (simply *Synechocystis* from here). I also modeled the flashing-light experiments using the mechanistic model presented in Chapter 4, which represents a pooling of light energy, photoinhibition, and photoacclimation. By comparing the experimental and modeling results, I found that the model could represent the flashing light data trends well and could provide a mechanistic explanation for why fluctuating light often leads to a decreased rate of phototrophic growth. Some inconsistencies between the model and experimental results also lead us to the hypothesis that *Synechocystis* could be better represented with more than one pool of light intermediates.

6.3. Materials and Methods

6.3.1. *Synechocystis* Growth-rate Experiments

Synechocystis was received from Dr. Willem Vermaas's laboratory at Arizona State University and cultivated in an FMT150 Photobioreactor (Photon Systems Instruments, Drásov, Czech Republic; simply FMT from here). The FMT was illuminated from one side by an LED light panel which I set to flashing light conditions with the length of the flash and dark period varied. The culture's liquid volume was maintained at 370 ml with a light path of 2.4 cm. I utilized a V-200 magnetic stirrer (from Photon Systems Instruments) that rotated a 3.5-cm stir bar against the back wall of the reactor vessel, and I set its rotation rate at approximately 480 rpm. The FMT took automatic readings of optical density at 735nm (OD_{735}), and to maintain a constant biomass density I used the turbidostat module (also from Photon Systems Instruments), which diluted the culture with autoclaved BG-11 (Rippka et al., 1979) when it reached an OD_{735} set-point of 0.21 and stopped diluting when a lower OD_{735} set-point of 0.20 was reached. By maintaining a dilute culture, light attenuation was minimized. The FMT temperature was set at 30°C. pH was maintained between 7.5 and 8.5 by bubbling carbon dioxide when the upper set point (pH = 8.5) was reached using an MC122 pH Controller (Milwaukee Instruments, Rocky Mount, NC) and a solenoid valve (Milwaukee Instruments, Rocky Mount, NC).

The specific growth rate (μ; d^{-1}) was determined for the growth periods (non-diluting times of turbidostat operation) by fitting Equation 6.1 to the measured OD_{735}:

$$X = X_0 \exp(\mu t) \qquad \text{Equation 6.1}$$

where X_o is the initial biomass concentration at the beginning of the growth period (OD_{735}), and X is the biomass concentration (OD_{735}) after the time t (days) between X_o and X. The μ and X_o values were determined by minimizing the sum of squares between

the measured X values and modeled X values from Equation 6.1 (Hastie et al., 2009). Assuming that the relationship between OD_{735} and biomass dry weight (DW; mg L^{-1}) was stable over the course of one day, I measured DW once a day to establish the calibration between DW and OD_{735}. I measured DW by filtering 10 ml of culture through a dry 0.7-µm glass microfiber filter (Whatman®, Buckinghamshire, UK), drying the filter again (60°C overnight), subtracting the final mass from the initial mass, and dividing by 10 ml (Straka and Rittmann, 2017). For operation with longer flashes, I chose a period of 1 hour to determine µ during the dark periods. Steady-state reported µ values are taken as an average of 1 day of measurements, with the culture grown at the reported light conditions a minimum of 2 days before the reported data were taken.

I determined the spatially averaged light intensity (LI_{ave}) by dividing the integrated Beer-Lambert equation by the depth of the reactor:

$$LI_{ave} = \frac{LI_0(1-\exp(-\varepsilon DWw))}{\varepsilon DWw} \qquad \text{Equation 6.2}$$

where ε is the Beer-Lambert extinction coefficient ($m^2\ g^{-1}$), LI_o is the incident light intensity (µmol $m^{-2}\ s^{-1}$), and w is the depth of the FMT (0.024 m). The extinction coefficient (ε) was measured daily by the method reported by Straka and Rittmann (2017). Briefly, a petri dish with culture was suspended above a light source. The light was measured above the culture using a LI-190 PAR sensor (LI-COR Biosciences, Lincoln, NE). The culture in the petri dish was diluted and light measured again, until 5 readings and a deionized (DI) water reading were taken. The six data points were then fit to the beer-lambert equation with DW changing with the subsequent dilutions:

$$\varepsilon = \frac{\ln\left(\frac{LI_0}{LI}\right)}{DWd} \qquad \text{Equation 6.3}$$

where d is the depth of sample in the petri dish (0.009 m for 20ml of sample), LI_o is the light measurement for DI water, and LI is the light measurement with sample of DW biomass concentration. In all cases the LI_{ave} during illumination was ≥ 79% of the incident LI (LI_o).

6.3.2. Model Simulations

I performed flashing-light simulations with input light intensity (LI) that changed between the incident light intensity (LI_o) and complete darkness (LI = 0) in a step function with the time between depending on the set time in the light (t_l) and time in the dark (t_d). The LI_{aveo} value was then computed by taking the average, or $LI_{aveo} = LI_o * \phi = LI_o * t_l/(t_l+t_d)$. All modeling simulations were conducted using the model presented in Chapter 4, which considers: a pool of light energy (LI_p), photoacclimation (ε_{abs}), PSII photodamage (ε_{nf}), PSII repair inhibition (ζ), and PSI photodamage (δ). Of particular interest to this work is the equation for accumulation of LI_p (Equation 4.1 in Chapter 4):

$$\frac{dLI_p}{dt} = \left(\varepsilon_{abs} LI - \varepsilon_{nf} LI \ - \left(\frac{k_{LI} LI_p}{k_{LI}+LI_p} + \frac{LI_p^2}{k_{LI}+LI_p}\right) k_{LIp}\right) \frac{86400s}{d} \qquad \text{Equation 6.4}$$

where k_{LI} (μmol g^{-1}) is the half-maximum-rate light absorption, and k_{LIp} is the rate constant of light-pool dissipation. From left to right, the four terms in Equation 6.4 represent light absorption, non-photochemical quenching (NPQ) from damaged biomass, photochemical light quenching, and NPQ from other pigments.

I modeled the state variables (LI_p, ε_{abs}, ε_{nf}, ζ, and δ) dynamically over time using forward integration from initial conditions set at $\varepsilon_{abs} = \varepsilon_{abs,ss}(LI_{ave})$, $LI_p = \varepsilon_{abs} LI_{ave}/k_{LIp}$, $\varepsilon_{nf} = \varepsilon_{nf}(LI_{ave}, \varepsilon_{abs})$, $\zeta = 0$, and $\delta = 0$. The time step of the model simulation was set to $t_l/1000$ or $t_l/100000$ if $t_l \geq 1000s$. The model was run for $345600 * t_l$ (e.g., 4 days for t_l =

1 s); the first half of the output was discarded, as it represented acclimation, and steady-state results were given by the second half of the output data.

6.4. Results and Discussion

Figure 6.1 displays time-series model outputs for t_l = 6 hours with equal periods of dark ($t_l = t_d$; $\phi = 0.5$), along with measured μ. The model captures the μ trends in the experimental data well. It clearly shows the sharp change in μ immediately after a shift in LI, followed by the gradual acclimation to a steady-state μ for the given LI. The values of μ swing between -3 and 4 d^{-1}. The negative μ values reflect that LI_p had time to go to zero in the six hours of darkness, but it became very high once the light exposure was resumed.

Quite different patterns are present in Figure 6.2, which displays the time-series model outputs for t_l = 1 s with equal periods of dark ($t_l = t_d$; $\phi = 0.5$). Measured μ is not included for t_l = 1 s, because μ data could not be collected on a time scale fast enough to accurately capture changes with $t_l < 1$ hours. In the t_l = 1 s trial, light absorbed did not accrue or dissipate fast enough to see the full swing in LI_p present in Figure 6.1. This lead to μ swings between from slightly greater than 0 d^{-1} to almost 2 d^{-1}, but never to a negative μ.

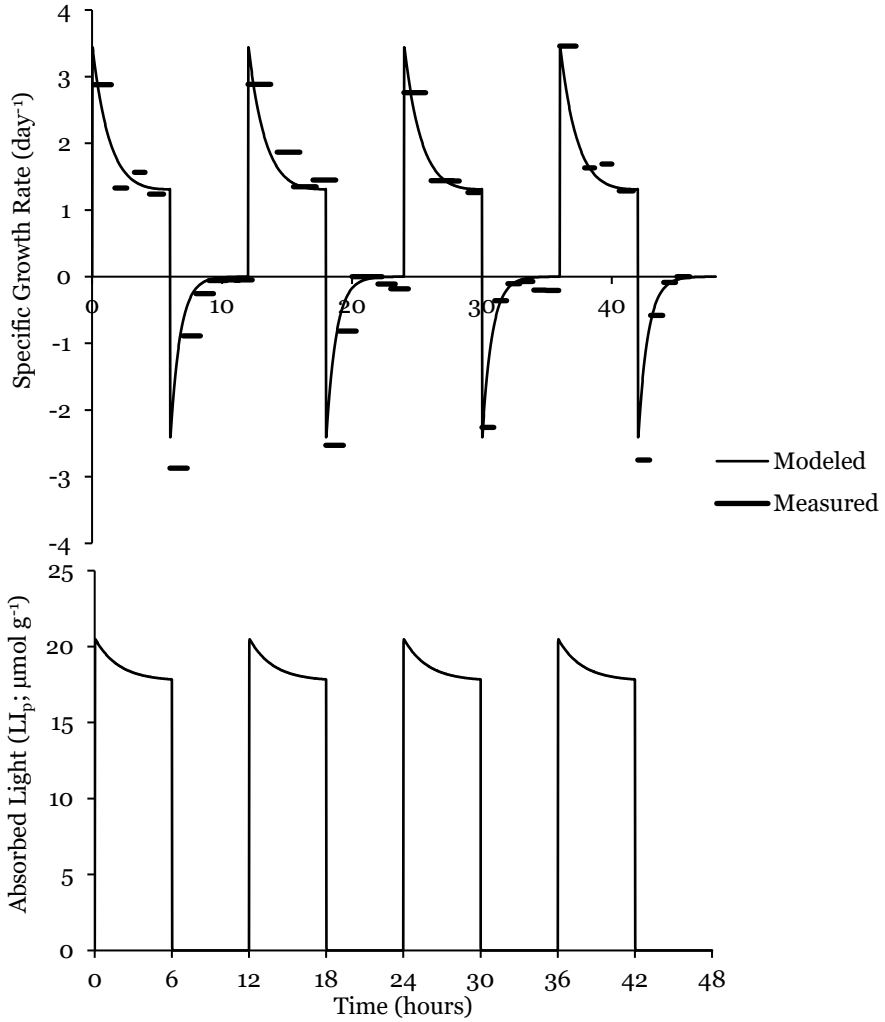

Figure 6.1: Modeled and measured specific growth rate (μ; top plot; day^{-1}) and modeled absorbed light (LI_p; bottom plot; μmol g^{-1}) for equal periods of light (LI = 168 μmol m^{-2} s^{-1}) and dark (LI = 0 μmol m^{-2} s^{-1}) with the light period (t_l) of 6 hours.

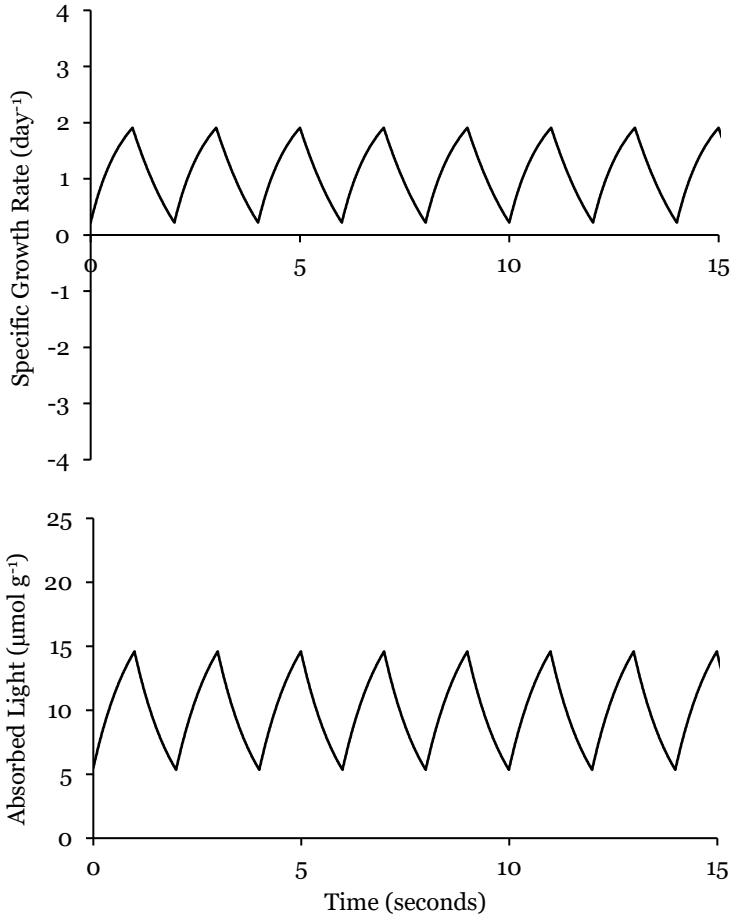

Figure 6.2: Modeled specific growth rate (μ; top plot; day^{-1}) and absorbed light (LI_p; bottom plot; μmol g^{-1}) for equal periods of light (LI = 168 μmol m^{-2} s^{-1}) and dark (LI = 0 μmol m^{-2} s^{-1}) with the light period (t_l) of 1 second.

Plot A of Figure 6.3 displays μ results from all the steady-state flashing-light experiments with equal time in light and dark ($t_l = t_d$; $\phi = 0.5$); plots A-E display corresponding model outputs. The duration of the flash spans more than 6 orders of magnitude, from 0.01 to 21,600 s (6 h). The modeling results show a two-stage curve with plateaus for $t_l <$ ~ 0.1 sec and > ~ 10 sec, although μ again declines for t_l above 15 min. (10^4 s). As the flash duration (t_l) became shorter, μ approached the level predicted for continuous light ($\mu = 1.25$ d^{-1}; shown as the horizontal line in plot A of Figure 6.3). As illustrated by the much narrower range of LI_p in Figure 6.2 ($t_l = 1$ s) compared to Figure 6.1 ($t_l = 6$ h), very fast flashes "blended" the light and dark conditions such that LI_p stayed in a narrow range, and the biomass had LI_p that was almost the same as if it were experiencing continuous light. This stabilization of LI_p at small t_l is further illustrated by the range of LI_p shown in plot E of Figure 6.3. However, as t_l became longer, LI_p spanned from 0 to around 20 μmol g^{-1}, and this led to μ gradually decreasing until it approached the lower plateau of ~ 0.8 d^{-1} at t_l ~ 10 s.

The modeled results illustrate several related effects contributing to the decline in μ with increasing t_l (and corresponding range of LI_p). While the second plateau ($t_l >$ 10 s) does not have light and dark periods long enough to show a range in photoacclimation (ε_{abs}; plot D of Figure 6.3), a net decrease in ε_{abs} occurs because the rate of acclimation to higher light is faster than to lower light. In addition, more energy is lost to NPQ (represented by $LI_p^2/(k_{LI} + LI_p)$ in Equation 6.4). Both factors contribute to a slight decrease in the average LI_p (plot E of Figure 6.3), which is what is used for growth. Furthermore, PSII photodamage (ε_{nf}; plot B of Figure 6.3) increases, primarily because of an increased level of PSII-repair inhibition (ζ; plot C of Figure 6.3). Repair inhibition occurs when LI_p exceeds the optimal photoacclimated LI_p, and, therefore, an increase in

ζ is expected as the range of LI_p increases. During the time of the spike in LI_p after the light is turned on, ε_{abs} corresponds to a lower LI_p.

The gradual decline in μ between t_l = 0.1 and 10 s corresponds to a transition in the behavior of LI_p: from invariant at very low t_l to the maximum swing by about t_l = 10 s. As the flashes become even longer (t_l > 15 min = 20000 s), the biomass begins to experience large swings in photoacclimation between the light and dark periods. This then results in more severe photodamage to PSII after longer periods of LI = 0, which is consistent with my findings in Chapter 5, that photodamage was more severe for *Synechocystis* that had been acclimated to lower LI.

Although the experimental and modeled μ results in Figure 6.3 have similar trends with t_l, the model's μ values are about 0.1 d^{-1} greater for the highest and lowest t_l values. The experimental data also appear to have a more gradual decline in μ, while the model has more of a step change in the range of 0.1 < t_l < 10 s. I hypothesize that the more gradual decline in μ is the result of *Synechocystis* having multiple electron pools, not just one, as the model represents with LI_p. For example, electrons moving through the electron-transport chain pass through numerous intermediates that could be built up or depleted at different rates. This could lead to a continuum of changing rate-limiting steps and a more gradual effect of increasing t_l on μ. Nonetheless, the single pool (LI_p) captured the major trend of t_l.

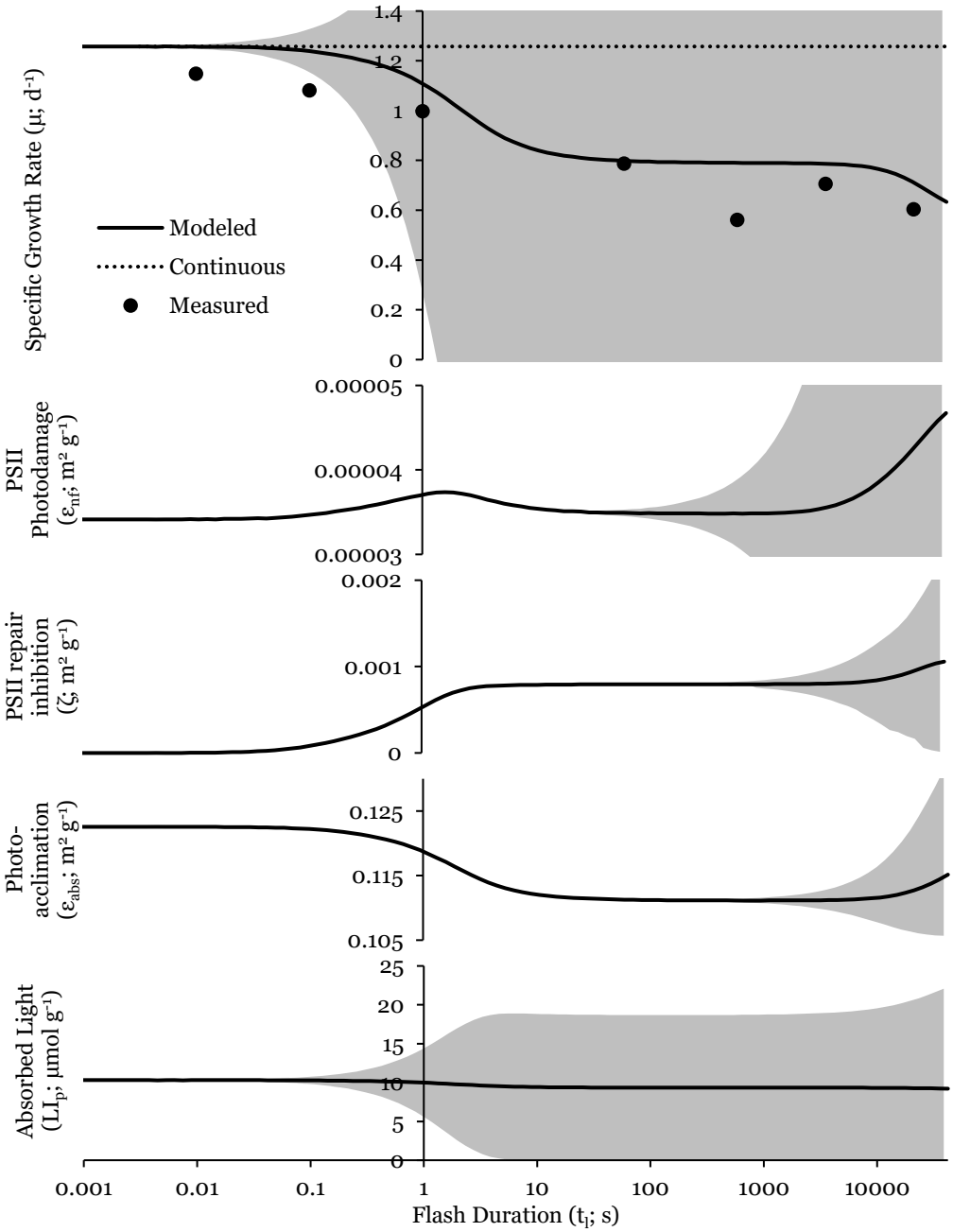

Figure 6.3: Measured steady-state 1-day average μ (A) and modeled steady-state μ (A), ε_{nf} (B), ζ (C), ε_{abs} (D), and LI_p (E) for *Synechocystis* cultures subjected to flashing light with the length of the flash (t_l) ranging from 0.01s to 21600s (6 h), equal duration of light and dark ($\phi = 0.5$), and $LI_{aveo} = 84$ μmol m^{-2} s^{-1}. For the experimental data, the incident light (LI_o) was 208 μmol m^{-2} s^{-1}, and OD_{735} was maintained between 0.2 and 0.21 (giving $LI_{ave} \approx 168$ μmol m^{-2} s^{-1}). The trials with larger t_l showed significant decay during the dark period, which means that OD_{735} dropped to as low as 0.175, but OD_{735} quickly rebounded once the light period started. For the modeled data, $LI_o = 168$ μmol m^{-2} s^{-1}, and the gray field represents the ranges of modeled values between the light and dark periods.

Plot A in Figure 6.4 displays μ results from a set of steady-state flashing light experiments in which the relative durations of the light and dark periods were varied; this is represented by changes in the duty cycle (ϕ; proportion of time in the light). The experiments with lower ϕ had higher LI_o to maintain the same LI_{aveo} = 84 μmol m^{-2} s^{-1}. On the one hand, the data for the shortest t_l (0.01s) show only a modest decrease in μ even as ϕ declined to as low as 0.1, which had LI_o = 1040 μmol m^{-2} s^{-1}. On the other hand, μ declined almost to zero for ϕ = 0.1 when t_l was 60 sec. For all values of t_l, μ decreased with smaller ϕ, which as seen in plot B in Figure 6.4 the average LI_p also trends down. Similar to Figure 6.3, lower average LI_p compared to the continuous light condition (ϕ = 1) corresponds to a larger range of LI_p values between the light and dark periods. These trends underscore the impact of large swings in LI_p, which causes reduced light absorption, more energy lose to NPQ and more PSII photodamage.

Again, the experimental and modeled results show similar trends, although the model over-estimated μ for the smallest values of t_l. The discrepancy was largest for t_l = 0.01s, for which the model predicted an almost complete blending effect even for ϕ = 0.1. While the energy pool represented in this model matched the results for t_l = 60 s very well, I speculate that the energy pool that controls kinetics at the shorter t_l differs from the rate-controlling pool for long t_l.

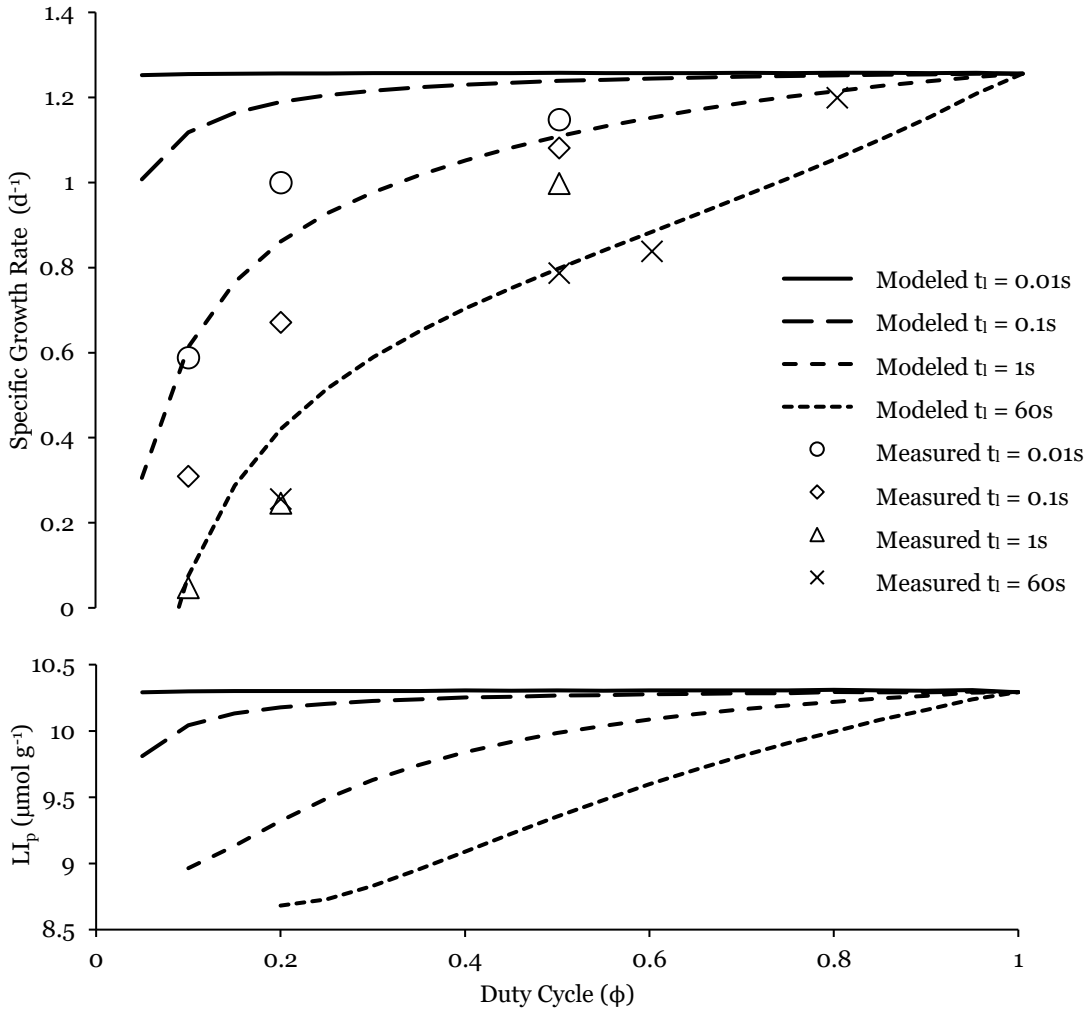

Figure 6.4: Measured steady-state 1-day average μ (A) and modeled steady-state μ (A) and average LI_p (B) for *Synechocystis* cultures subjected to flashing light with the length of the flash (t_l) equal to 0.01s, 0.1s, 1s, or 60s and the duty cycles (ϕ; $t_l/(t_l+t_d)$) ranging from 0.1 to 1. The incident light (LI_o) was adjusted to maintain an $LI_{aveo} \approx 84$ μmol m^{-2} s^{-1}. For the measured data, OD_{735} was maintained between 0.2 and 0.21 for all trials; therefore, LI_o = 130, 174, 208, 520, and 1040 μmol m^{-2} s^{-1}, for ϕ = 0.8, 0.6, 0.5, 0.2, and 0.1, respectively. For the modeled data LI_o was set to 84 μmol m^{-2} s^{-1}/ ϕ.

6.5. Conclusion

A series of flashing-light experiments using *Synechocystis* demonstrated that μ decreased with increasing t_l and decreased further with decreasing ϕ. A model that represents a pool of light energy (LI_p) captured and helped explain these trends in μ: very short flashes do not allow LI_p to change much from its value in continuous light, and this "blending" minimizes photodamage, maximizes LI_p, and gives a higher μ. In contrast, long flashes show large ranges in LI_p, corresponding higher energy loses to NPQ, more PSII repair inhibition, and depressed μ. The model tended to over-estimate μ for the highest and lowest t_l, giving a sharper step transition from the blended condition to the condition with large ranges in LI_p. I attribute these discrepancies to multiple pools of electron-containing intermediates instead of the one pool (LI_p) in the model.

7. APPLYING A LIGHT-DEPENDENT KINETIC MODEL TO *SYNECHOCYSTIS* SP. PCC 6803 CULTURES OF DIFFERENT CONCENTRATIONS

7.1. Introduction

In Chapters 3, and 6 I established that microalgae in photobioreactors or natural ecosystems are subjected to changing light, sometimes rapidly. While I learned much from the flashing light experiments of Chapter 6, they do not account for the gradual change in LI as the biomass moves from high LI to low LI due to mixing (Brindley et al., 2011). Therefore, another approach is to assume that the biomass cycles throughout the light profile in the culture medium (Merchuk et al., 2007; Talmy et al., 2013). In this chapter, I apply a simple mixing regime to my light-depend model from Chapter 4, and I compare the results to measured growth rates of more concentrated cultures. I find that the model captures large-scale trends of the experimental data, but quantitative accuracy is poor, which means that some phenomenon is not represented well enough.

7.2. Materials and Methods

7.2.1. Model Simulations

I ran a series of model simulations to represent the effects of biomass mixing in a dense culture that gives a large change in LI from the front of the culture to the back. In this mixing pattern, I assumed the biomass started at one side of an illuminated reactor and travelled to the other side of the reactor at a speed V (m s^{-1}). Once it reached the other side of the reactor, it travelled at speed V back to the other side. This cycle was repeated. LI at any point in the reactor was computed using the Beer-Lambert equation:

$$LI = LI_0 \exp(-\varepsilon X d) \qquad \text{Equation 7.1}$$

where d is the distance from the illuminated side of the reactor (m), ε is the modeled extinction coefficient, and X is the input for how concentrated the culture in the simulation is. For these simulations, the maximum depth was 0.024m to match the depth of the FMT.

A sample mixing pattern is plot A of

Figure 7.1, and plot B is the corresponding LI that the biomass experienced. LI at the front side is LI_0, and LI declines (according to Equation 7.1) to the back side. The time-dependent LI values were then input into the model equations presented in Chapter 4.

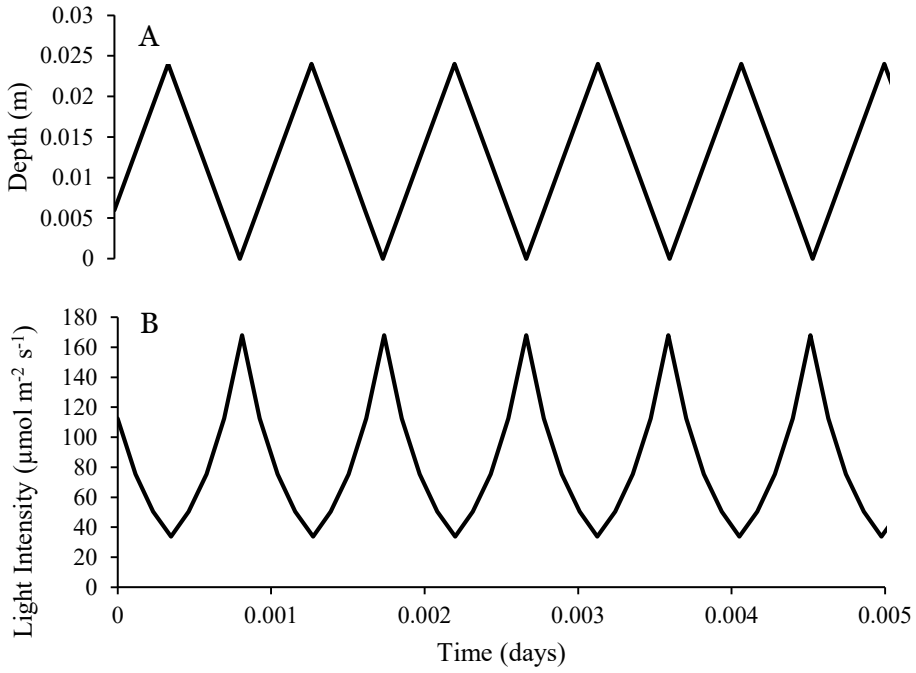

Figure 7.1: Example saw-toothed patterns of (A) the depth of the biomass from the front of the reactor and (B) the corresponding LI. For this example, the incident light intensity (LI_o) was 168 μmol m^{-2} s^{-1}, the biomass concentration (X) was 430 mg L^{-1}, the extinction coefficient (ε) was 0.15, and the mixing speed (V) was 0.015 m s^{-1}.

I performed two different simulations: The first had constant LI_o, X, and LI_{ave}, but changing V, and the second had a constant LI_{ave} and V, but changing LI_o and X. In the second case, when X changed, LI_o was changed in parallel to maintain a constant LI_{ave}. As described in Chapter 6, all simulations were conducted using forward integration in which the state variables (LI_p, ε_{abs}, ε_{nf}, ζ, and δ) were adjusted for each time step. The initial conditions were set at $LI_p = LI_{ave}$, $\varepsilon_{abs} = \varepsilon_{abs,ss}(LI_{ave})$, $\varepsilon_{nf} = \varepsilon_{nf}(LI_{ave}, \varepsilon_{abs,ss}(LI_{ave}))$, $\zeta = 0$, and $\delta = 0$. The time step of the model simulation was set to 0.01s, the model was run for two days for acclimation, and steady-state taken as the average of the next 2 days.

In order to compare these mixing simulations to the flashing-light simulations from Chapter 6, I normalize them by cycle time. I define the cycle time as the time it

takes to travel from the back of the reactor to the front of the reactor and back again in the mixing simulations: 2d/V. This is related to the time for the light and dark period in the flashing-light simulations ($t_l + t_d = t_l/ \phi$). Therefore, for a given V and ϕ, an apparent t_l can be computed, $t_l = \phi 2d/V$.

7.2.2. *Synechocystis* Growth Conditions

I grew *Synechocystis* sp. PCC 6803 in the FMT operated with the magnetic stirrer used in Chapter 6 and the turbidostat set to different ranges of OD_{735} (0.4 to 0.42, 0.8 to 0.84, and 1.0 to 1.04). The mixer was set to either approximately 120 or 480 rpm, and the light was constant. The specific growth rate and the average internal LI (LI_{ave}) were determined as described in Chapter 6, and all reported specific growth rates (μ) are 1-day average values obtained after a minimum of 2 days of acclimation. In order to compare the mixing effects of these dense cultures to the flashing-light work presented in Chapter 6, I equate the flashing light duty cycle (ϕ) to LI_{ave}/LI_o, (under flashing light $\phi = LI_{ave}/LI_o$).

7.3. Results and Discussion

Figure 7.2 displays the modeled steady-state μ results for a mixed culture with X = 430 mg L^{-1}, LI_o = 168 μmol m^{-2} s^{-1}, and changing mixing speeds (V; plotted as the apparent t_l = 0.024m/V). LI_o and X were chosen to match the LI_o and ϕ of the flashing light results displayed in Figure 6.3, which is also included as Figure 7.2. Similar to the flashing-light results, the model predicts a step change in μ described by the transition between the complete blending of LI_p (so the biomass responds as if they are growing under continuous light at LI_{ave}) and experiencing discrete light conditions. The step change in μ in the case of mixing is less severe: stepping down from 1.25 to 1.0 d^{-1}, as opposed to flashing light, which stepped down from 1.25 to 0.8 d^{-1}. The less-dramatic step down occurs because LI does not go all the way to 0, but to the minimum LI (LI_{min}) of 34 μmol m^{-2} s^{-1} or LI_p = 3.9 μmol g^{-1}. The step occurs between mixing speeds of 0.1 and 0.003 m s^{-1} (apparent t_l = 0.24 to 8 s), which is approximately the same as the flashing light which occurs between t_l = 0.1 to 10 s flashes.

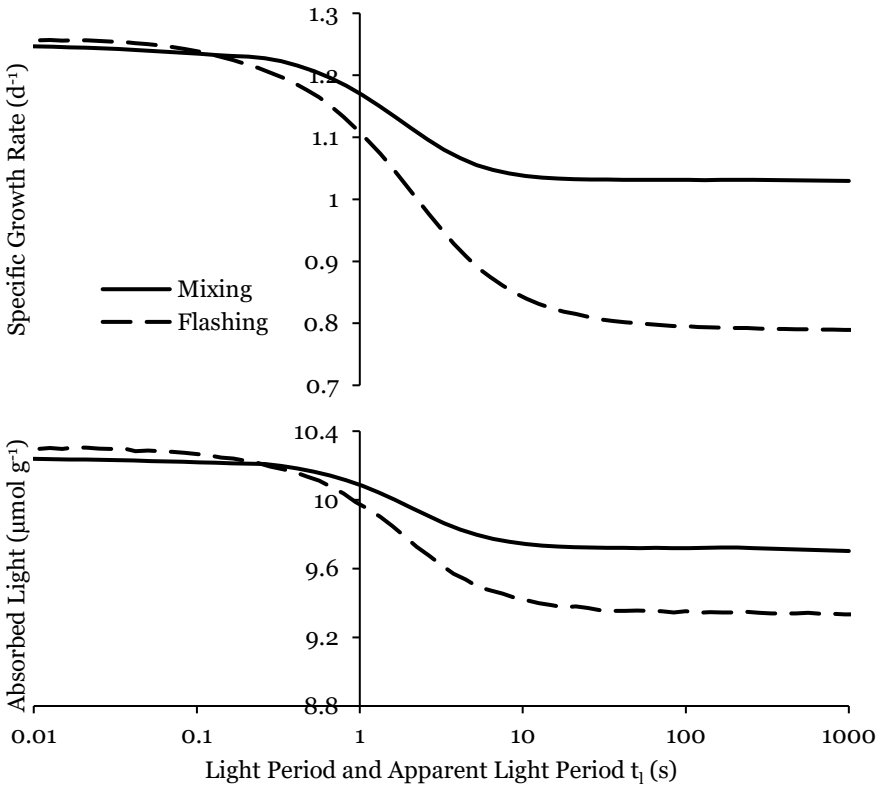

Figure 7.2: Modeled steady-state μ and average LI_p for mixed and flashing light simulations for different apparent light periods (t_l) and t_l respectively. For both simulations the duty cycle ($\phi = LI_{ave}/LI_o$) was 0.5 and incident light (LI_o) 168 μmol m^{-2} s^{-1}, making LI_{ave} 84 μmol m^{-2} s^{-1}. For the mixing simulation, the apparent light period was determined as t_l = 0.024 m/ mixing speeds (V; m s^{-1}), and the biomass concentration (X) was 430 mg L^{-1}. The mixing was a saw-toothed mixing pattern in a reactor illuminated from one side and a depth of 0.024m. The model equations are presented in Chapter 4. Flashing light results are also presented in Figure 6.3.

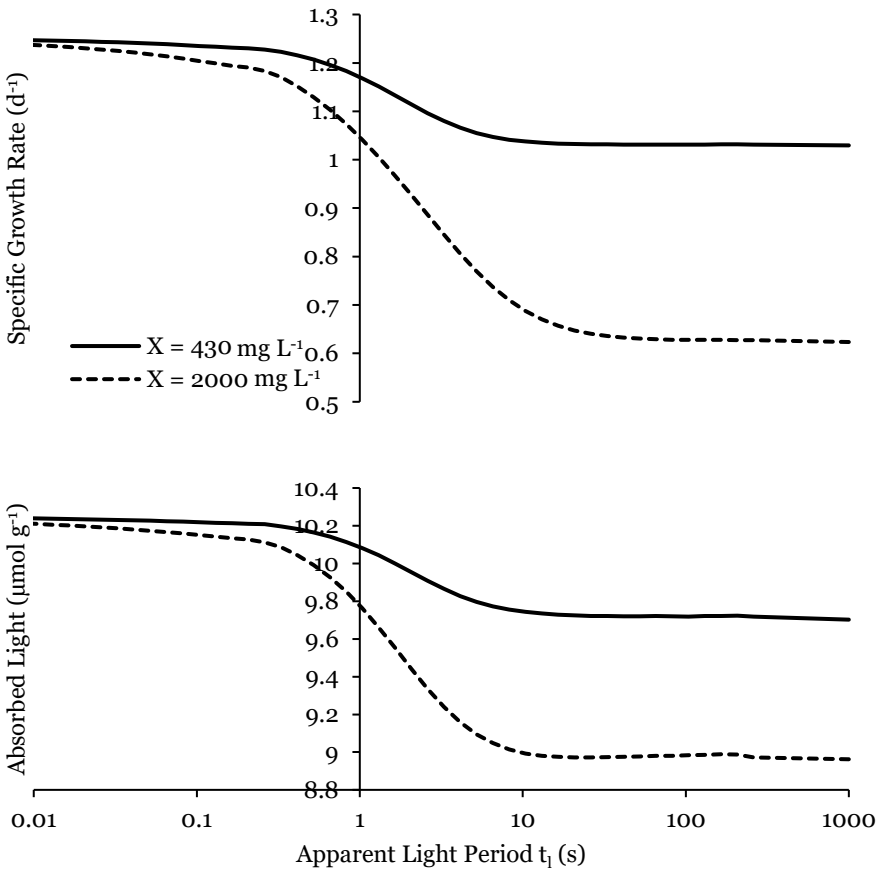

Figure 7.3: Modeled steady-state μ and average LI_p for mixed simulations of biomass concentration (X) of 430 and 2000 mg L^{-1} for different apparent t_l (0.024 m/ mixing speeds (V; m s^{-1})). For both simulations LI_{ave} was 84 μmol m^{-2} s^{-1}, but the incident light (LI_o) was 168 and 625 μmol m^{-2} s^{-1} for X = 430 and 2000 mg L^{-1} respectively making the duty cycle ($\phi = LI_{ave}/LI_o$) 0.5 and 0.13 respectively. The mixing was a saw-toothed mixing pattern in a reactor illuminated from one side and a depth of 0.024m. The model equations are presented in Chapter 4.

Figure 7.3 compares the same mixing condition from Figure 7.2 (X = 430 mg L^{-1}, LI_o = 168 μmol m^{-2} s^{-1}, and changing V) with a mixing condition with the same LI_{ave} (84 μmol m^{-2} s^{-1}), but where LI_{min} approaches 0 (X = 2000 mg L^{-1}, LI_o = 625 μmol m^{-2} s^{-1}, LI_{min} = 0.4 μmol m^{-2} s^{-1}). The trial with the higher biomass concentration shows the same step-function as the less-concentrated culture and the flashing light curve from Figure 7.2. The step change in μ in the case of the more concentrated mixing is more severe: stepping down from 1.25 to 0.6 d^{-1}, although this also corresponds to a lower ϕ (0.13).

As I discuss in Chapter 6, the decrease in μ as t_l increases (V decreases) is related to the range in LI_p. The lower plot of Figure 7.2 and lower plot of Figure 7.3 shows a step change in the average LI_p as mixing or flashing gets slower. In both figures, it is clear that a larger step in LI_p corresponds to the larger step in μ. This decrease in LI_p indicates a larger range in LI_p, which I illustrate in Chapter 6 as being due to slightly less light absorbance and more LI_p lost to non-photochemical quenching (NPQ). With rapid mixing, or rapid flashing, the "blending" effect eliminated the range in LI_p, whereas with the slower mixing, or longer flashes, the biomass experienced the light extremes, and, therefore, showed an overall lower light absorbance and increase NPQ at high light condition. In addition to less LI_p, slower mixing or longer flashes increased inhibition of PSII repair, which is caused by more intense light than the photoacclimated condition and occurs on the illuminated side of the reactor or during the flash. Also as discussed in Chapter 6, I believe the curves in Figures 7.2 and 7.3 may have too-sharp of a step change, since multiple electron pooling intermediates likely exist.

Figure 7.4 shows modeled results that summarize how biomass concentration affects μ. As the biomass concentration increases, μ declines. A higher biomass concentration causes the biomass to spend more time exposed to lower LI, which leads

to more light loss to NPQ and PSII repair inhibition when the biomass travels to the surface with the most intense LI. The model predicts that this affect can be mitigated by rapid mixing: The simulation with V = 0.1 m s^{-1} shows very little effect from biomass concentration. This trend is consistent with light flashing, because, when transitions are fast enough, the blending effect keeps LI_p nearly constant. Slow mixing and a dense culture concentration accentuate the negative impacts of NPQ and photodamage.

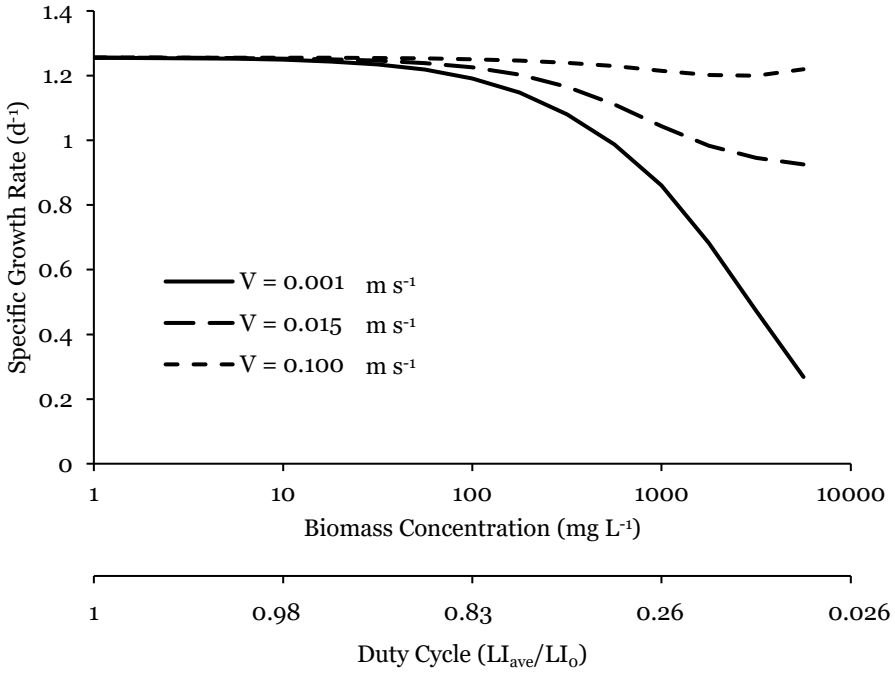

Figure 7.4: Modeled steady-state μ for 3 different mixing speeds (V; m s^{-1}) with a saw-toothed mixing pattern in a reactor illuminated from one side and a depth of 0.024m. The biomass concentration (X; mg L^{-1}) was varied and incident light (LI_o) adjusted accordingly to maintain an LI_{ave} of 84 μmol m^{-2} s^{-1}. The model equations are presented in Chapter 4.

An increase in X corresponds to a decrease in ϕ (ϕ = LI_{ave}/LI_o, and LI_{ave} decreases relative to LI_o with increasing X (Equation 6.2)). Therefore, the second horizontal axis in Figure 7.4 expressing the corresponding ϕ. In Chapter 6, I established that decreasing ϕ results in lower μ, which is in further agreement to these results.

All experimental μ results are summarized in Table 7.1. Each OD_{735} and LI_o setting has a trial with the mixing speed at 120 or 480 rpm.

Table 7.1: Specific Growth Rate (μ) of *Synechocystis* Cultures Grown at Different Concentrations and Incident Light Intensities (LI_o)

Mixing Speed (rpm)	Biomass Conc. (mg L^{-1})	LI_o	LI_{ave}	LI_{min}	Equated ϕ	measured steady-state μ (d^{-1})
		($\mu mol\ m^{-2}\ s^{-1}$)				
480	274	208	137	77	0.66	1.06
120	275	208	151	103	0.72	0.63
480	579	416	205	75	0.49	0.35
120	616	416	207	70	0.50	0.14
480	597	170	78	21	0.46	0.17
120	630	170	84	28	0.49	0.09
480	843	331	127	21	0.38	0.13
120	901	331	125	19	0.38	0.09

Several aspects of the experimental results in Table 7.1 agree with the modeling trends. First, all trials with the slower mixing speed showed a lower μ than the corresponding μ with the higher mixing speed. For example, for the biomass concentration of ~ 275 mg L^{-1}, μ was 1.06 d^{-1} for 480 rpm and 0.63 d^{-1} for 120 rpm. This trend agrees with the results modeled in Figures 7.2 and 7.3. Second, as the biomass concentration (X) increased (and ϕ decreased), μ became lower. For example, for 480 rpm, μ went from 1.06 d^{-1} to 0.35 d^{-1} as X increased from ~275 to 579 mg L^{-1}. This was true for the slower mixing speed and the faster mixing speed trials, and it agrees with the modeling trends in Figure 7.4. Finally, we do not see a direct relationship between LI_{ave} and μ, which is very important, because LI_{ave} often is used for modeling concentrated cultures (Béchet et al., 2013). I note that none of these cultures were dense enough that they experienced total darkness, as the smallest LI_{min} was 19 $\mu mol\ m^{-2}\ s^{-1}$ with X ≈ 900 mg L^{-1}.

Table 7.2 quantitatively compares the experimental μ and modeled μ valued with the fastest mixing (V = 1 m s^{-1}; i.e. μ at LI_{ave}) and slowest (V = 0.001 m s^{-1}). These mixing speeds put μ on either side of the step illustrated in Figures 7.2 and 7.3. While the modeled μ values agree with the experimental μ values in terms of all the trends with mixing speed and biomass concentration, the experimental μ values are noticeably lower than the modeled μ values with either V. One possible explanation is that the mixer, even set at 480 rpm, did not do an effective job of mixing the culture. Another possibility is that the actual mixing patterns were not well represented by the saw-tooth pattern of Figure 7.1. More importantly, however, is that the model has no mechanism that could allow it to predict μ values close to the low measured μ values using the X and LI_os tested. I note that these cultures qualitatively looked healthy (deep green with no hint of brown or yellow), the growth curves showed the usual trend, and I have no reason to suspect nutrient limitation. Therefore, the LI model may be missing a mechanism that becomes important only when evaluating effects of more concentrated cultures.

Table 7.2: Modeled and Measured Specific Growth Rate (μ) of *Synechocystis* Cultures Grown at Different Concentrations and Incident Light Intensities (LI_o)

Mixing Speed (rpm)	Biomass (mg L^{-1})	LI_o (μmol m^{-2} s^{-1})	Measured steady-state μ (d^{-1})	Modeled μ V = 1 m s^{-1}	Modeled μ V = 0.001 m s^{-1}
480	274	208	1.06	1.63	1.38
120	275	208	0.63	1.7	1.39
480	579	416	0.35	1.91	1.40
120	616	416	0.14	1.92	1.37
480	597	170	0.17	1.2	0.87
120	630	170	0.09	1.25	0.85
480	843	331	0.13	1.57	1.02
120	901	331	0.09	1.56	0.98

7.4. Conclusions and Future Work

In this chapter, I illustrated how the model presented in Chapter 4 predicts trends observed in concentrated cultures including: slow mixing and decreased ϕ result in depressed μ. This is in agreement with the trends I found for the flashing light work presented in Chapter 6. Additionally, this work underscores that modeling μ using LI_{ave} is not an appropriate simplification for a concentrated culture.

It is not clear what is missing in the model to cause the mismatch in values between modeled and experimental μ value (Table 7.2). An improved experimental protocol may be needed to address the reliability of the experimental data and to uncover a mechanistic explanation. A good approach would be to employ bioreactors of different depths and X values such that LI_o and LI_{ave} can be set the same, but achieved with different biomass concentrations. This could isolate an effect of X. A complication, however, would be adjusting the mixing speeds so that the reactors would experience approximately equal LI changes as they mix. Clearly, such experiments would be a major undertaking and one that demands systematic planning.

8. SYNTHETIC SUMMARY AND FUTURE WORK

8.1. Synthesis

The goal of the photobioreactor team, on which I have worked for the past six years, is to create sustainable fuels with microalgae. A key aspect to this is understanding the mechanisms that control productivity so that growth conditions can be optimized to maximize production. Although the best path to sustainable fuel is not clear (reviewed in section 1.2), in all cases healthy cells need to be cultivated; thus, my focus has been on what controls biomass production. A useful tool for understanding and optimization is a mathematical model. Well-developed mathematical models have the power to simulate real situations in a fraction of the time it would take to run the experiments. They also represent our understanding of the important processes in a systematic and quantitative manner.

In this work, I focused most on light-dependent growth. Light is the energy source we desire to capture. As I discuss throughout this dissertation, biomass concentration, mixing, photoacclimation, and photodamage are light-related effects that always are present. Therefore, when studying other mechanisms that control productivity, it is necessary to have an understanding of light-dependent growth, rather than trying (and typically failing) to remove all effects of light. An example of this is in Chapter 2, where my main goal was investigating phosphorus stress, but in doing so, I employed a simple empirical light model to account for the decreasing growth as the culture grew more concentrated.

The light-dependent mathematical model I developed in Chapter 4 has important quantifiable implications for microalgae cultivation: e.g., the intensity of the Arizona sun will likely cause substantial photodamage to biomass cultured indoors and moved outdoors, photosynthetic efficiency drops precipitously over exposures of 300 μmol m^{-2}

s^{-1}, and mixing is very important to optimizing the growth of concentrated cultures. Before building a pilot system or an algae production system, running model simulations can identify design and operation conditions that minimize negative effects of photodamage and maximize light utilization.

Development of the model I present in Chapter 4 started with my attempt to fit a growth-irradiance curve that I could use to model *Synechocystis* growth. During these initial experiments, however, I realized that the incident light intensity could not represent all the phenomena affecting growth rate. Other factors were related to the history of the culture, but previous attempts to include "history" in light-dependent growth models could not describe what I was observing. Therefore, my focus had to move from model fitting and simulation to model development. The outcome was most satisfying, as the model in Chapter 4 is by far the most complete microalgal model to date. It has allowed me to understand how LI and changes in LI affect photosynthesis, photodamage, and photoacclimation.

The power and complexity of the model stems from it having a set of state-variables: a pool of light energy (LI_p), photoacclimation (ε_{abs}), PSII photodamage (ε_{nf}), PSII repair inhibition (ζ), and PSI photodamage (δ). The latter two have not been included in any other model. The chapters and how they relate to these variables are:

Chapter 3: I show that photoacclimation correlates with two easily quantified values: light attenuation (ε), measured through a method I developed, and the ratio of optical density at 680 nm to 735 nm (OD_{680}/OD_{735}). As *Synechocystis* is exposed to lower LI, it increases its light absorbing pigments, and this causes ε and OD_{680}/OD_{735} to increase.

Chapter 4: I present the complete light-limited growth model, including definitions of the state variables and the theory behind them.

Chapter 5: I present the experimental growth and OD_{680}/OD_{735} results that I need to evaluate the model and fit its parameters. Using step-changes in light intensity, I quantify the rate of change for ε_{abs}, ε_{nf}, ζ, and δ. The model is able to explain all observed changes in growth rate. For example, biomass exposed to lower LI is able to absorb more light energy upon a step up in LI, but this quickly leads to ζ and excess ε_{nf}. The trend in specific growth rate (μ) after an increasing step in light is, therefore, initially high, followed by a depression as ζ sets in, and finally slowly recovers to the new steady-state μ at that light condition as ζ is repaired. Alternatively, the response to a step down in LI shows a sharp drop in μ which quickly rebounds to near the new steady-state and then slowly increases as the biomass photoacclimates.

Chapter 6: I apply the model to understand the impacts of flashing light. While LI_p hardly changes when the flash rate is fast (< 0.1 sec), it experiences large swings with long-duration flashes that lower μ. Some deviations between model predictions and experimental results lead me to suggest that the model could be further improved through the use of multiple energy pools.

Chapter 7: I apply the model to understand the effects of mixing in dense cultures. Mixing, incident light, and biomass concentration show complex interactions for controlling the growth rate. The interactions are only partly explained by phenomena identified by flashing light.

Taken together, these chapters provide a comprehensive description and validation of the light-dependent mathematical model I developed.

Light-based mechanisms are not the only ones that control photosynthesis of *Synechocystis*. In addition to light, in Chapter 2 I present work investigating how phosphorus affects *Synechocystis* growth, and how phosphorus-stress depends heavily

on the microbial community. While nutrients (primarily carbon, nitrogen, and phosphorus) should be easy to control, in an effort to minimize input, we need an understanding of their growth requirements/effects. Additionally, the work in Chapter 2 exemplifies the potential of compounding mechanisms (in this case community structure and phosphorus-stress).

8.2. Future Directions

While my model for light-limited microalgal growth is by far the most complete to date, some aspects can be improved. Here, I offer some ideas on how to improve understanding of light-dependent growth and the model I present:

- In my work, PSII photodamage, PSII repair inhibition, and PSI photodamage were not measured directly, but were conceptual variables that allowed me to depict complex growth trends. Interactions among these variables could be improved by direct measurements. For example, techniques in photosynthesis research allow quantification of photodamage based on fluorescence (Krause and Weis, 1991). Applying these techniques will not be easy, but could give deeper insights of the model formulation and parameterization.
- In Chapter 6, I propose that the model could be improved by including several pools of light energy. This could be addressed computationally by explicitly adding mass balances for electron (e^-) carrier intermediates such as plastoquinone, plastocyanin, and NADH/NADPH. This should smooth out the observed step function in the μ-t_l curve. Taking this a step further, a pool of ATP also can be included as an energy carrier. The inclusion of energy and e^- carriers would require an additional variable for photoacclimation, which is a term for the ratio of PSI to PSII (higher PSI/PSII would mean more ATP/e^-). I suspect that including ATP could make the model substantially more mechanistic. For example, photodamage repair could have an e^- and ATP cost rather than simply a reduced photosynthetic growth.
- Chapter 7 contains an unresolved discrepancy between the modeled and experimental results. Further experimental work could help reveal what is not being captured by the model. One idea I have, is to compare reactors with different depths

and different biomass concentration, but the same incident LI and average LI. This may tease out if biomass concentration is itself a factor.

- Temperature is an important factor that requires further understanding. In laboratory systems, it is very easy to control temperature, but outdoor cultivation typically experiences large temperature swings. The optimal growth rate of *Synechocystis* has been reported between 30 and 35°C, with active photosynthesis occurring between 18-44°C (Sheng et al., 2011; Zavřel et al., 2015). Adding temperature effects to the light model would be a very beneficial next step, and identifying what processes are affected would be of paramount importance. Others have suggested that photochemical processes (light capture and photo-damage) will not be (or will be very weakly) temperature dependent, but biochemical processes (photodamage repair and growth) will be strongly temperature dependent (Eilers and Peeters, 1988; Kok, 1956a). I would, therefore, apply temperature dependency to photosynthetic growth and repair of photosystem II photodamage.
- In addition to light and nutrients, our team has had an on-going discussion about how microbial community affects *Synechocystis*, including the growth effect of heterotrophic bacteria, how to minimize grazer related reactor crashes, and how to control or prevent biofilm formation. I review some of the community interactions in section 1.7, but understanding catastrophic crashes due to grazers, which I have observed in the benchtop photobioreactor, is an area of high importance. Finding an effective control strategy would be a huge benefit, and one control strategy that I believe is worth investigating is inducing periodic pH swings within the tolerance of *Synechocystis* (Montemezzani et al., 2015). This can be done simply by allowing *Synechocystis* to deplete C_i and raise the pH to 11, followed by adding CO_2 and

dropping the pH to 7. If implemented effectively, the pH strategy will severely impede the growth of the grazers, but with minimal consequences to *Synechocystis*.

REFERENCES

Abu-Ghosh, S., Fixler, D., Dubinsky, Z., Iluz, D., 2016. Flashing light in microalgae biotechnology. Bioresour. Technol. 203, 357–363. doi:10.1016/j.biortech.2015.12.057

Akimoto, S., Yokono, M., Yokono, E., Aikawa, S., Kondo, A., 2014. Short-term light adaptation of a cyanobacterium, Synechocystis sp. PCC 6803, probed by time-resolved fluorescence spectroscopy. Plant Physiol. Biochem. 81, 149–154. doi:10.1016/j.plaphy.2014.01.007

Allen, C.D., Macalady, A.K., Chenchouni, H., Bachelet, D., McDowell, N., Vennetier, M., Kitzberger, T., Rigling, A., Breshears, D.D., Hogg, E.H. (Ted), Gonzalez, P., Fensham, R., Zhang, Z., Castro, J., Demidova, N., Lim, J.H., Allard, G., Running, S.W., Semerci, A., Cobb, N., 2010. A global overview of drought and heat-induced tree mortality reveals emerging climate change risks for forests. For. Ecol. Manage. 259, 660–684. doi:10.1016/j.foreco.2009.09.001

Anderson, J.M., Park, Y.I., Chow, W.S., 1998. Unifying model for the photoinactivation of Photosystem II in vivo under steady-state photosynthesis. Photosynth. Res. 56, 1–13. doi:10.1023/A:1005946808488

Arrhenius, S., 1896. On the Influence of Carbonic Acid in the Air upon the Temperature of the Earth. Philos. Mag. J. Sci. 41, 237–276. doi:10.1086/121158

Bahadar, A., Bilal Khan, M., 2013. Progress in energy from microalgae: A review. Renew. Sustain. Energy Rev. 27, 128–148. doi:10.1016/j.rser.2013.06.029

Baker, A.C., Glynn, P.W., Riegl, B., 2008. Climate change and coral reef bleaching: An ecological assessment of long-term impacts, recovery trends and future outlook. Estuar. Coast. Shelf Sci. 80, 435–471. doi:10.1016/j.ecss.2008.09.003

Béchet, Q., Chambonnière, P., Shilton, A., Guizard, G., Guieysse, B., 2015. Algal productivity modeling: A step toward accurate assessments of full-scale algal cultivation. Biotechnol. Bioeng. 112, 987–96. doi:10.1002/bit.25517

Béchet, Q., Shilton, A., Guieysse, B., 2013. Modeling the effects of light and temperature on algae growth: state of the art and critical assessment for productivity prediction during outdoor cultivation. Biotechnol. Adv. 31, 1648–63. doi:10.1016/j.biotechadv.2013.08.014

Beck, C., Hertel, S., Rediger, A., Lehmann, R., Wiegard, A., Kölsch, A., Heilmann, B., Georg, J., Hess, W.R., Axmann, I.M., 2014. Daily expression pattern of protein-encoding genes and small noncoding RNAs in synechocystis sp. strain PCC 6803. Appl. Environ. Microbiol. 80, 5195–5206. doi:10.1128/AEM.01086-14

Berberoglu, H., Pilon, L., 2007. Experimental measurements of the radiation characteristics of Anabaena variabilis ATCC 29413-U and Rhodobacter sphaeroides ATCC 49419. Int. J. Hydrogen Energy 32, 4772–4785. doi:10.1016/j.ijhydene.2007.08.018

Berberoglu, H., Pilon, L., Melis, A., 2008. Radiation characteristics of Chlamydomonas reinhardtii CC125 and its truncated chlorophyll antenna transformants tla1, tlaX and tla1-CW+. Int. J. Hydrogen Energy 33, 6467–6483. doi:10.1016/j.ijhydene.2008.07.071

Berg, K. a, Lyra, C., Sivonen, K., Paulin, L., Suomalainen, S., Tuomi, P., Rapala, J., 2009. High diversity of cultivable heterotrophic bacteria in association with cyanobacterial water blooms. ISME J. 3, 314–325. doi:10.1038/ismej.2008.110

Blankenship, R.E., 2002. Molecular Mechanisms of Photosynthesis. Blackwell Publishing, Williston, VT.

Bosma, R., van Zessen, E., Reith, J.H., Tramper, J., Wijffels, R.H., 2007. Prediction of Volumetric Productivity of an Outdoor Photobioreactor. Biotechnol. Bioeng. 97, 1108–1120. doi:10.1002/bit

Bratbak, G., Thingstad, T.F., 1985. Phytoplankton-Bacteria Interactions - an Apparent Paradox - Analysis of a Model System With Both Competition and Commensalism. Mar. Ecol. Prog. Ser. doi:10.3354/meps025023

Brindley, C., Acién Fernández, F.G., Fernández-Sevilla, J.M., 2011. Analysis of light regime in continuous light distributions in photobioreactors. Bioresour. Technol. 102, 3138–3148. doi:10.1016/j.biortech.2010.10.088

Britannica, 2017. Sunlight. Encycl. Br. Inc.

Chambers, E.G., 2017. Light Radiation Conversion [WWW Document]. URL http://www.egc.com/useful_info_lighting.php

Chen, I., Hill, J.K., Ohlemüller, R., Roy, D.B., Thomas, C.D., 2011. Rapid range shifts of species of climate warming. Science (80-.). 333, 1024–1026. doi:10.1126/science.1206432

Chisti, Y., 2007. Biodiesel from microalgae. Biotechnol. Adv. 25, 294–306. doi:10.1016/j.biotechadv.2007.02.001

Cook, J., Nuccitelli, D., Green, S., Richardson, M., Winkler, B., Painting, R., Way, R., Jacobs, P., Skuce, A., 2013. Quantifying the consensus on anthropogenic global warming in the scientific literature. Environ. Res. Lett. 8.

Cordell, D., Neset, T.-S.S., Prior, T., 2012. The phosphorus mass balance: identifying “hotspots” in the food system as a roadmap to phosphorus security. Curr. Opin. Biotechnol. 23, 839–45. doi:10.1016/j.copbio.2012.03.010

Cornet, J.-F., Dussap, C.G., Gros, J.-B., Binois, C., Lasseur, C., 1995. A simplified monodimensional approach for modeling coupling between radiant light transfer and growth kinetics in photobioreactors. Chem. Eng. Sci. 50, 1489–1500. doi:10.1016/0009-2509(95)00022-W

Danger, M., Oumarou, C., Benest, D., Lacroix, G., 2007. Bacteria can control

stoichiometry and nutrient limitation of phytoplankton. Funct. Ecol. 21, 202–210. doi:10.1111/j.1365-2435.2006.01222.x

Daroch, M., Geng, S., Wang, G., 2013. Recent advances in liquid biofuel production from algal feedstocks. Appl. Energy 102, 1371–1381. doi:10.1016/j.apenergy.2012.07.031

Dasgupta, J., Ananyev, G.M., Dismukes, G.C., 2008. Photoassembly of the Water-Oxidizing Complex in Photosystem II. Coord. Chem. Rev. 252, 347–360. doi:10.1016/j.ccr.2007.08.022

Davis, R., Aden, A., Pienkos, P.T., 2011. Techno-economic analysis of autotrophic microalgae for fuel production. Appl. Energy 88, 3524–3531. doi:10.1016/j.apenergy.2011.04.018

Dillon, A., Parry, J.D., 2008. Characterization of temperate cyanophages active against freshwater phycocyanin-rich Synechococcus species. Freshw. Biol. 53, 1253–1261. doi:doi:10.1111/j.1365-2427.2007.01938.x

DOE, U.S., 2010. National Algal Biofuels Technology Roadmap, in: U.S. Department of Energy. p. 140. doi:Public Law No. 106-554

Droop, M.R., 1973. Some Thoughts on Nutrient Limitation in Algae. J. Phycol. 9, 264–272. doi:10.1111/j.0022-3646.1973.00264.x

Edelman, M., Mattoo, A.K., 2008. D1-protein dynamics in photosystem II: the lingering enigma. Photosynth. Res. 98, 609–620. doi:10.1007/s11120-008-9342-x

Eilers, P., Peeters, J., 1988. A model for the relationship between light intensity and the rate of photosynthesis in phytoplankton. Ecol. Modell. 42, 199–215.

Ellis, R.J., 2010. Tackling Unintelligent Design. Nature 463, 164–165. doi:10.1029/2008GL036500

Erickson, E., Wakao, S., Niyogi, K.K., 2015. Light stress and photoprotection in *Chlamydomonas reinhardtii*. Plant J. 82, 449–465. doi:10.1111/tpj.12825

Falkowski, P.G., LaRoche, J., 1991. Acclimation to Spectral Irradiance in Algae. J. Phycol. 27, 8–14. doi:10.1111/j.0022-3646.1991.00008.x

Feller, U., Anders, I., Mae, T., 2008. Rubiscolytics: Fate of Rubisco after its enzymatic function in a cell is terminated. J. Exp. Bot. 59, 1615–1624. doi:10.1093/jxb/erm242

Fogg, G.E., 1983. The Ecological Significance of Extracellular Products of Phytoplankton Photosynthesis. Bot. Mar. 26, 3–14. doi:10.1515/botm.1983.26.1.3

Fuhs, G., 1969. Phosphorus content and rate of growth in the diatoms Cyclotella nana and Thalassiosira fluviatilis. J. Phycol. 5, 312–321.

García-Camacho, F., Sánchez-Mirón, a, Molina-Grima, E., Camacho-Rubio, F., Merchuck, J.C., 2012. A mechanistic model of photosynthesis in microalgae

including photoacclimation dynamics. J. Theor. Biol. 304, 1–15. doi:10.1016/j.jtbi.2012.03.021

Gillis, J., 2017. For Third Year, the Earth in 2016 Set Heat Record. New York Times A1.

Girard, J.M., Roy, M.L., Hafsa, M. Ben, Gagnon, J., Faucheux, N., Heitz, M., Tremblay, R., Deschênes, J.S., 2014. Mixotrophic cultivation of green microalgae Scenedesmus obliquus on cheese whey permeate for biodiesel production. Algal Res. 5, 241–248. doi:10.1016/j.algal.2014.03.002

Grobbelaar, J.U., 2010. Microalgal biomass production: challenges and realities. Photosynth. Res. 106, 135–144. doi:10.1007/s11120-010-9573-5

Grobbelaar, J.U., Soeder, C.J., Stengel, E., 1990. Modeling algal productivity in large outdoor cultures and waste treatment systems. Biomass 21, 297–314. doi:10.1016/0144-4565(90)90079-Y

Gururani, M.A., Venkatesh, J., Tran, L.S.P., 2015. Regulation of photosynthesis during abiotic stress-induced photoinhibition. Mol. Plant 8, 1304–1320. doi:10.1016/j.molp.2015.05.005

Hastie, T., Tibshirani, R., Friedman, J., 2009. The Elements of Statistical Learning: Data Mining, Inference, and Prediction, 2nd ed. Springer. doi:10.1007/b94608

Hay, C.C., Morrow, E., Kopp, R.E., Mitrovica, J.X., 2015. Probabilistic reanalysis of twentieth-century sea-level rise. Nature 517, 481–484. doi:10.1038/nature14093

Henderson, R.K., Baker, A., Parsons, S. a., Jefferson, B., 2008. Characterisation of algogenic organic matter extracted from cyanobacteria, green algae and diatoms. Water Res. 42, 3435–3445. doi:10.1016/j.watres.2007.10.032

Henderson, T., 2017. Light Absorption, Reflection, and Transmission [WWW Document]. Phys. Classr. URL http://www.physicsclassroom.com/class/light/Lesson-2/Light-Absorption,-Reflection,-and-Transmission

Heng, R.-L., Lee, E., Pilon, L., 2014. Radiation characteristics and optical properties of filamentous cyanobacterium Anabaena cylindrica. J. Opt. Soc. Am. A. Opt. Image Sci. Vis. 31, 836–45.

Huntington, T.G., 2006. Evidence for intensification of the global water cycle: Review and synthesis. J. Hydrol. 319, 83–95. doi:10.1016/j.jhydrol.2005.07.003

IEA, 2014. Key World Energy Statistics 2014. Chirat, France. doi:10.1787/key_energ_stat-2014-en

IPCC, 2014. Climate Change 2014 Synthesis Report. doi:10.1017/CBO9781107415324

Iwakuma, T., Yasuno, M., 1983. A comparison of several mathematical equations describing photosynthesis-light curve for natural phytoplankton populations. Arch.

fur Hydrobiol. Stuttgart 97, 208–226.

Janssen, M., Janssen, M., De Winter, M., Tramper, J., Mur, L.R., Snel, J., Wijffels, R.H., 2000. Efficiency of light utilization of Chlamydomonas reinhardtii under medium-duration light/dark cycles. J. Biotechnol. 78, 123–137. doi:10.1016/S0168-1656(99)00233-3

Janssen, M., Kuijpers, T.C., Veldhoen, B., Ternbach, M.B., Tramper, J., Mur, L.R., Wijffels, R.H., 1999. Specific growth rate of Chlamydomonas reinhardtii and Chlorella sorokiniana under medium duration light/dark cycles: 13-87 s. Prog. Ind. Microbiol. 35, 323–333. doi:10.1016/S0079-6352(99)80124-6

Janssen, M., Slenders, P., Tramper, J., Mur, L.R., Wijffels, R., 2001. Photosynthetic efficiency of Dunaliella tertiolecta under short light/dark cycles. Enzyme Microb. Technol. 29, 298–305. doi:http://dx.doi.org/10.1016/S0141-0229(01)00387-8

Jassby, A., Platt, T., 1976. Mathematical formulation of the relationship between photosynthesis and light for phytoplankton. Limnol. Oceanogr. 21, 540–547.

John, E., Flynn, K., 2000. Modelling phosphate transport and assimilation in microalgae; how much complexity is warranted? Ecol. Modell. 125, 145–157.

Johnson, Z.I., Sheldon, T.L., 2007. A high-throughput method to measure photosynthesis-irradiance curves of phytoplankton. Limnol. Oceanogr. Methods 5, 417–424. doi:10.4319/lom.2007.5.417

Jones, S.M.J., Harrison, S.T.L., 2014. Aeration energy requirements for lipid production by Scenedesmus sp. in airlift bioreactors. Algal 5, 1–9. doi:10.1016/j.algal.2014.03.003

Juroszek, P., Tiedemann, A. von, 2015. Linking Plant Disease Models to Climate Change Scenarios to Project Future Risks of Crop Diseases: A Review. J. Plant Dis. Prot. 122, 3–15.

Kamen, M.D., 1963. Primary Processes in Photosynthesis. Academic Press, New York, NY. doi:10.1016/B978-1-4832-2959-1.50008-X

Kandilian, R., Lee, E., Pilon, L., 2013. Radiation and optical properties of Nannochloropsis oculata grown under different irradiances and spectra. Bioresour. Technol. 137, 63–73. doi:10.1016/j.biortech.2013.03.058

Kaneko, T., Sato, S., Kotani, H., Tanaka, a, Asamizu, E., Nakamura, Y., Miyajima, N., Hirosawa, M., Sugiura, M., Sasamoto, S., Kimura, T., Hosouchi, T., Matsuno, a, Muraki, a, Nakazaki, N., Naruo, K., Okumura, S., Shimpo, S., Takeuchi, C., Wada, T., Watanabe, a, Yamada, M., Yasuda, M., Tabata, S., 1996. Sequence analysis of the genome of the unicellular cyanobacterium Synechocystis sp. strain PCC6803. II. Sequence determination of the entire genome and assignment of potential protein-coding regions. DNA Res. 3, 109–136. doi:10.1093/dnares/3.3.109

Kaplan, A., Reinhold, L., 1999. Co 2 Concentrating Mechanisms in Microorganisms.

Transport 50, 539–570. doi:10.1139/b05-907

Keeling, C.D. (Scipps I. of O., 2015. Atmospheric CO2 Data [WWW Document]. URL http://scrippsco2.ucsd.edu/data/atmospheric_co2 (accessed 1.1.15).

Keymer, P.C., Lant, P. a., Pratt, S., 2013. Modelling microalgal activity as a function of inorganic carbon concentration: accounting for the impact of pH on the bicarbonate system. J. Appl. Phycol. 26, 1343–1350. doi:10.1007/s10811-013-0146-9

Kim, H.W., Vannela, R., Zhou, C., Harto, C., Rittmann, B.E., 2010. Photoautotrophic nutrient utilization and limitation during semi-continuous growth of Synechocystis sp. PCC6803. Biotechnol. Bioeng. 106, 553–63. doi:10.1002/bit.22724

Kok, B., 1956a. On the Inhibition of Photosynthesis by Intense Light. Biochim. Biophys. Acta 21, 234–244.

Kok, B., 1956b. Photosynthesis in flashing light. Biochim. Biophys. Acta 21, 245–258. doi:10.1016/0006-3002(56)90004-X

Krause, G.H., Weis, E., 1991. Chlorophyll Fluorescence and Photosynthesis: The Basics. Annu. Rev. Plant Physiol. Plant Mol. Bioi 42, 313–49. doi:10.1146/annurev.pp.42.060191.001525

Le Chevanton, M., Garnier, M., Bougaran, G., Schreiber, N., Lukomska, E., Bérard, J.B., Fouilland, E., Bernard, O., Cadoret, J.P., 2013. Screening and selection of growth-promoting bacteria for Dunaliella cultures. Algal Res. 2, 212–222. doi:10.1016/j.algal.2013.05.003

Lewis, N.S., 2007. Powering the Planet. Mater. Res. Soc. Spring Meet. 32, 808–820. doi:10.1557/mrs2007.168

Lindeburg, M.R., 2015. Environmental Engineering Reference Manual for the PE Exam, 3rd ed. Professional Publications, Inc, Belmont, CA.

Liu, X., Brune, D., Vermaas, W., Curtiss, R., 2010. Production and secretion of fatty acids in genetically engineered cyanobacteria. Proc. Natl. Acad. Sci. U. S. A. 6803, 2–7. doi:10.1073/pnas.1001946107

Losh, J.L., Young, J.N., Morel, F.M.M., 2013. Rubisco is a small fraction of total protein in marine phytoplankton. New Phytol. 198, 52–58. doi:10.1111/nph.12143

MacIntyre, H.L., Kana, T.M., Anning, T., Geider, R.J., 2002. Photoacclimation of Photosynthesis Irradiance Response Curves and Photosynthetic Pigments in Microalgae and Cyanobacteria. J. Phycol. 38, 17–38.

Madigan, M.T., Martinko, J.M., 2006. Brock Biology of Microorganisms, 11th ed. Pearson Education, Inc., Upper Saddle River, NJ.

Manabe, S., Wetherald, R.T., Milly, P.C.D., Delworth, T.L., Stouffer, R.J., 2004. Century-scale change in water availability: CO2-quadrupling experiment. Clim. Change 64,

59–76. doi:10.1023/B:CLIM.0000024674.37725.ca

Mayhew, P.J., Jenkins, G.B., Benton, T.G., 2008. A long-term association between global temperature and biodiversity, origination and extinction in the fossil record. Proc. Biol. Sci. 275, 47–53. doi:10.1098/rspb.2007.1302

Merchuk, J.C., Garcia-Camacho, F., Molina-Grima, E., 2007. Photobioreactor design and fluid dynamics. Chem. Biochem. Eng. Q. 21, 345–355.

Metcalf & Eddy, I., 2003. Wastewater Engineering Treatment and Reuse, Fourth Edi. ed. The McGraw-Hill Companies, Inc., Boston.

Mirón, A.S., Garcı´a, M.C.C., Gómez, A.C., Camacho, F.G., Grima, E.M., Chisti, Y., 2003. Shear stress tolerance and biochemical characterization of Phaeodactylum tricornutum in quasi steady-state continuous culture in outdoor photobioreactors. Biochem. Eng. J. 16, 287–297. doi:10.1016/S1369-703X(03)00072-X

Monod, J., 1949. The Growth of Bacterial Cultures. Annu. Rev. Microbiol. 3, 371–394.

Montemezzani, V., Duggan, I.C., Hogg, I.D., Craggs, R.J., 2015. A review of potential methods for zooplankton control in wastewater treatment High Rate Algal Ponds and algal production raceways. Algal Res. 11, 211–226. doi:10.1016/j.algal.2015.06.024

Morel, A., Bricaud, A., 1981. Theoretical Results Concerning Light-Absorption in a Discrete Medium, and Application To Specific Absorption of Phytoplankton. Deep. Res. Part a-Oceanographic Res. Pap. 28, 1375–1393. doi:10.1016/0198-0149(81)90039-X

Morell, M., Paul, K., Kane, H., Andrews, T., 1992. Rubisco: Maladapted or Misunderstood. Aust. J. Bot. 40, 431. doi:10.1071/BT9920431

Mulders, K.J.M., Lamers, P.P., Martens, D.E., Wijffels, R.H., 2014. Phototrophic pigment production with microalgae: biological constraints and opportunities. J. Phycol. 50, 229–242. doi:10.1111/jpy.12173

Muller-Feuga, A., Le Guédes, R., Pruvost, J., 2003. Benefits and limitations of modeling for optimization of Porphyridium cruentum cultures in an annular photobioreactor. J. Biotechnol. 103, 153–163. doi:10.1016/S0168-1656(03)00100-7

Murray, T., Scharrer, K., Selmes, N., Booth, A.D., James, T.D., Bevan, S.L., Bradley, J., Cook, S., Cordero Llana, L., Drocourt, Y., Dyke, L., Goldsack, A., Hughes, A.L., Luckman, A.J., McGover, J., 2015. Extensive retreat of Greenland tidewater glaciers, 2000-2010. Arctic, Antarct. Alp. Res. 47, 427–447.

Myers, J., 1946. Culture Conditions And The Development Of The Photosynthetic Mechanism. III. Influence of Light Intensity on Cellular Characteristics of Chlorella. J. Gneral Physiol. 29, 419–427.

Nath, K., Jajoo, A., Poudyal, R.S., Timilsina, R., Park, Y.S., Aro, E.-M., Nam, H.G., Lee,

C.-H., 2013. Towards a critical understanding of the photosystem II repair mechanism and its regulation during stress conditions. FEBS Lett. 587, 3372–81. doi:10.1016/j.febslet.2013.09.015

Nedbal, L., Trtílek, M., Červený, J., Komárek, O., Pakrasi, H.B., 2008. A photobioreactor system for precision cultivation of photoautotrophic microorganisms and for high-content analysis of suspension dynamics. Biotechnol. Bioeng. 100, 902–910. doi:10.1002/bit.21833

Nguyen, B.T., 2015. Photoautotrophic Production of Biomass, Laurate, and Soluble Organics by Synechocystis sp. PCC 6803. doi:10.1017/CBO9781107415324.004

Nguyen, B.T., Rittmann, B.E., 2015. Predicting Dissolved Inorganic Carbon in Photoautotrophic Microalgae Culture via the Nitrogen Source. Environ. Sci. Technol. 49, 9826–9831. doi:10.1021/acs.est.5b01727

Nishiyama, Y., Allakhverdiev, S.I., Murata, N., 2011. Protein synthesis is the primary target of reactive oxygen species in the photoinhibition of photosystem II. Physiol. Plant. 142, 35–46. doi:10.1111/j.1399-3054.2011.01457.x

NOAA, 2017. What are greenhouse gases? [WWW Document]. Greenh. Gases. URL https://www.ncdc.noaa.gov/monitoring-references/faq/greenhouse-gases.php

Park, J.B.K., Craggs, R.J., Shilton, A.N., 2011. Wastewater treatment high rate algal ponds for biofuel production. Bioresour. Technol. 102, 35–42. doi:10.1016/j.biortech.2010.06.158

Pereira, H.M., Leadley, P.W., Proença, V., Alkemade, R., Scharlemann, J.P.W., Fernandez-Manjarrés, J.F., Araújo, M.B., Balvanera, P., Biggs, R., Cheung, W.W.L., Chini, L., Cooper, H.D., Gilman, E.L., Guénette, S., Hurtt, G.C., Huntington, H.P., Mace, G.M., Oberdorff, T., Revenga, C., Rodrigues, P., Scholes, R.J., Sumaila, U.R., Walpole, M., 2010. Scenarios for global biodiversity in the 21st century. Science (80-.). 330, 1496–1501. doi:10.1126/science.1196624

Perez-Garcia, O., Escalante, F.M.E., de-Bashan, L.E., Bashan, Y., 2011. Heterotrophic cultures of microalgae: Metabolism and potential products. Water Res. 45, 11–36. doi:10.1016/j.watres.2010.08.037

Petit, R.J., Raynaud, D., Basile, I., Chappellaz, J., Ritz, C., Delmotte, M., Legrand, M., Lorius, C., Pe, L., 1999. Climate and atmospheric history of the past 420,000 years from the Vostok ice core, Antarctica. Nature 399, 429–413. doi:10.1038/20859

Platt, T., Jassby, A., 1976. The Relationship Between Photosynthesis and Light for Natural Assemblages of Coastal Marine Phytoplankton. J. Phycol. 12, 421–430.

Podevin, M., De Francisci, D., Holdt, S.L., Angelidaki, I., 2015. Effect of nitrogen source and acclimatization on specific growth rates of microalgae determined by a high-throughput in vivo microplate autofluorescence method. J. Appl. Phycol. 27, 1415–1423. doi:10.1007/s10811-014-0468-2

Poore, R.Z., Williams, R.S., Tracey, C., 2000. Sea Level and Climate, U.S. Geological Survey Fact Sheet.

Post, A.F., 1987. Transient state characteristics of changes in light conditions for the cyanobacterium oscillatoria-agardhii II. Dynamics in cellular contents and growth rates. Arch Microbiol 149, 19–23.

Pottier, L., Pruvost, J., Deremetz, J., Cornet, J.F., Legrand, J., Dussap, C.G., 2005. A fully predictive model for one-dimensional light attenuation by Chlamydomonas reinhardtii in a torus photobioreactor. Biotechnol. Bioeng. 91, 569–582. doi:10.1002/bit.20475

Powles, S.B., 1984. Photoinhibition of Photosynthesis Induced by Visible Light. Annu. Rev. Plant Physiol. 35, 15–44. doi:10.1146/annurev.pp.35.060184.000311

Privoznik, K.G., Daniel, K.J., Incropera, F.P., 1978. Absorption, extinction and phase function measurements for algal suspensions of chlorella pyrenoidosa. J. Quant. Spectrosc. Radiat. Transf. 20, 345–352. doi:10.1016/0022-4073(78)90103-6

Rashidan, K.K., Bird, D.F., 2001. Role of Predatory Bacteria in the Termination of a Cyanobacterial Bloom. Microb. Ecol. 41, 97–105. doi:10.1007/s002480000074

Razzak, S. a., Hossain, M.M., Lucky, R. a., Bassi, A.S., de Lasa, H., 2013. Integrated CO2 capture, wastewater treatment and biofuel production by microalgae culturing—A review. Renew. Sustain. Energy Rev. 27, 622–653. doi:10.1016/j.rser.2013.05.063

Reynolds, C., 2006. Ecology of Phytoplankton, The effects of brief mindfulness intervention on acute pain experience: An examination of individual difference. doi:10.1017/CBO9781107415324.004

Rippka, R., Deruelles, J., Waterbury, J.B., Herdman, M., Stanier, R.Y., 1979. Generic Assignments, Strain Histories and Properties of Pure Cultures of Cyanobacteria. J. Gen. Microbiol. 111, 1–61. doi:10.1099/00221287-111-1-1

Rittmann, B.E., 2008. Opportunities for renewable bioenergy using microorganisms. Biotechnol. Bioeng. 100, 203–12. doi:10.1002/bit.21875

Rittmann, B.E., Bae, W., Namkung, E., Lu, C.J., 1987. A critical evaluation of microbial product formation in biological processes. Water Sci. Technol. 19, 517–528.

Rittmann, B.E., McCarty, P.L., 2001. Environmental biotechnology: principles and applications. McGraw-Hill.

Rosenzweig, C., Elliott, J., Deryng, D., Ruane, A.C., Müller, C., Arneth, A., Boote, K.J., Folberth, C., Glotter, M., Khabarov, N., Neumann, K., Piontek, F., Pugh, T. a M., Schmid, E., Stehfest, E., Yang, H., Jones, J.W., 2014. Assessing agricultural risks of climate change in the 21st century in a global gridded crop model intercomparison. Proc. Natl. Acad. Sci. U. S. A. 111, 3268–73. doi:10.1073/pnas.1222463110

Saha, R., Liu, D., Connor, A.H., Liberton, M., Yu, J., Bhattacharyya-pakrasi, M., 2016.

Diurnal Regulation of Cellular Processes in the Cyanobacterium 7, 1–14. doi:10.1128/mBio.00464-16.Editor

Sañudo-Wilhelmy, S.A., Tovar-Sanchez, A., Fu, F., Capone, D.G., Carpenter, E.J., Hutchins, D.A., 2004. The impact of surface-adsorbed phosphorus on phytoplankton Redfield stoichiometry. Nature 432, 897–901. doi:10.1038/nature03125

Scheller, H.V., Haldrup, A., 2005. Photoinhibition of photosystem I. Planta 221, 5–8. doi:10.1111/j.1399-3054.2010.01437.x

Schirrmeister, B.E., Gugger, M., Donoghue, P.C.J., 2015. Cyanobacteria and the Great Oxidation Event: evidence from genes and fossils. Palaeontology 58, 769–785. doi:10.1111/pala.12178

Sheng, J., Kim, H.W., Badalamenti, J.P., Zhou, C., Sridharakrishnan, S., Krajmalnik-Brown, R., Rittmann, B.E., Vannela, R., 2011. Effects of temperature shifts on growth rate and lipid characteristics of Synechocystis sp. PCC6803 in a bench-top photobioreactor. Bioresour. Technol. 102, 11218–11225. doi:10.1016/j.biortech.2011.09.083

Shunyu, S., Yongding, L., Yinwu, S., Genbao, L., Dunhai, L., 2006. Lysis of Aphanizomenon flos-aquae (Cyanobacterium) by a bacterium Bacillus cereus. Biol. Control 39, 345–351. doi:10.1016/j.biocontrol.2006.06.011

Singh, A., Nigam, P.S., Murphy, J.D., 2011. Renewable fuels from algae: An answer to debatable land based fuels. Bioresour. Technol. 102, 10–16. doi:10.1016/j.biortech.2010.06.032

Snoeyink, V., Jenkins, D., 1980. Water Chemistry. John Wiley & Sons, Inc., New York, NY.

Sonoike, K., 2011. Photoinhibition of photosystem I. Physiol. Plant. 142, 56–64. doi:10.1111/j.1399-3054.2010.01437.x

Spolaore, P., Joannis-Cassan, C., Duran, E., Isambert, A., 2006. Commercial applications of microalgae. J. Biosci. Bioeng. 101, 87–96. doi:10.1263/jbb.101.87

Straka, L., Rittmann, B.E., 2017. Light attenuation changes with photo-acclimation in a culture of Synechocystis sp. PCC 6803. Algal Res. 21, 223–226. doi:10.1016/j.algal.2016.11.024

Stramski, D., Morel, A., 1990. Optical properties of photosynthetic picoplankton in different physiological states as affected by growth irradiance. Deep Sea Res. Part A, Oceanogr. Res. Pap. 37, 245–266. doi:10.1016/0198-0149(90)90126-G

Suttle, C. a, 2005. Viruses in the sea. Nature 437, 356–361. doi:10.1038/nature04160

Suttle, C. a., 2000. Ecological, evolutionary, and geochemical consequences of viralinfection of cyanobacteria and eukaryotic algae, Viral Ecology.

doi:10.1016/B978-012362675-2/50007-0

Szabó, I., Bergantino, E., Giacometti, G.M., 2005. Light and oxygenic photosynthesis: energy dissipation as a protection mechanism against photo-oxidation. EMBO Rep. 6, 629–34. doi:10.1038/sj.embor.7400460

Talmy, D., Blackford, J., Hardman-Mountford, N., Dumbrell, A.J., Geider, R.J., 2013. An optimality model of photoadaptation in contrasting aquatic light regimes. Limnol. Oceanogr. 58, 1802–1818. doi:10.4319/lo.2013.58.5.1802

Tennessee, T.U. of, 2017. Sunlight [WWW Document]. Inst. Agric. URL https://ag.tennessee.edu/solar/Pages/What Is Solar Energy/Sunlight.aspx

Tikkanen, M., Mekala, N.R., Aro, E.-M., 2014. Photosystem II photoinhibition-repair cycle protects Photosystem I from irreversible damage. Biochim. Biophys. Acta - Bioenerg. 1837, 210–215. doi:10.1016/j.bbabio.2013.10.001

Tomaselli, L., Boldrini, G., Margheri, M., 1997. Physiological behaviour of Arthrospira (Spirulina) maxima during acclimation to changes in irradiance. J. Appl. Phycol. 37–43.

Touloupakis, E., Cicchi, B., Benavides, A.M.S., Torzillo, G., 2016. Effect of high pH on growth of Synechocystis sp. PCC 6803 cultures and their contamination by golden algae (Poterioochromonas sp.). Appl. Microbiol. Biotechnol. 100, 1333–1341. doi:10.1007/s00253-015-7024-0

Vejrazka, C., Janssen, M., Streefland, M., Wijffels, R.H., 2011. Photosynthetic efficiency of Chlamydomonas reinhardtii in flashing light. Biotechnol. Bioeng. 108, 2905–13. doi:10.1002/bit.23270

Vejrazka, C., Streefland, M., Wijffels, R.H., Janssen, M., 2015. The role of an electron pool in algal photosynthesis during sub-second light-dark cycling. Algal Res. 12, 43–51. doi:10.1016/j.algal.2015.07.017

Vinyard, D.J., Ananyev, G.M., Charles Dismukes, G., 2013. Photosystem II: The Reaction Center of Oxygenic Photosynthesis*. Annu. Rev. Biochem. 82, 577–606. doi:10.1146/annurev-biochem-070511-100425

Wang, H., Zhang, W., Chen, L., Wang, J., Liu, T., 2013. The contamination and control of biological pollutants in mass cultivation of microalgae. Bioresour. Technol. 128, 745–750. doi:10.1016/j.biortech.2012.10.158

Wang, Y., Duanmu, D., Spalding, M.H., 2011. Carbon dioxide concentrating mechanism in Chlamydomonas reinhardtii: Inorganic carbon transport and CO2 recapture. Photosynth. Res. 109, 115–122. doi:10.1007/s11120-011-9643-3

Xia, H., Li, T., Deng, F., Hu, Z., 2013. Freshwater cyanophages. Virol. Sin. 28, 253–9. doi:10.1007/s12250-013-3370-1

Yao, B., Xi, B., Hu, C., Huo, S., Su, J., Liu, H., 2011. A model and experimental study of

phosphate uptake kinetics in algae: Considering surface adsorption and P-stress. J. Environ. Sci. 23, 189–198.

Yao, M., Elling, F.J., Jones, C., Nomosatryo, S., Long, C.P., Crowe, S.A., Antoniewicz, M.R., Hinrichs, K.U., Maresca, J.A., 2016. Heterotrophic bacteria from an extremely phosphate-poor lake have conditionally reduced phosphorus demand and utilize diverse sources of phosphorus. Environ. Microbiol. 18, 656–667. doi:10.1111/1462-2920.13063

Young, J.N., Heureux, A.M.C., Sharwood, R.E., Rickaby, R.E.M., Morel, F.M.M., Whitney, S.M., 2016. Large variation in the Rubisco kinetics of diatoms reveals diversity among their carbon-concentrating mechanisms. J. Exp. Bot. 67, erw163. doi:10.1093/jxb/erw163

Yu, J., Liberton, M., Cliften, P.F., Head, R.D., Jacobs, J.M., Smith, R.D., Koppenaal, D.W., Brand, J.J., Pakrasi, H.B., 2015. Synechococcus elongatus UTEX 2973, a fast growing cyanobacterial chassis for biosynthesis using light and CO2. Sci. Rep. 5, 8132. doi:10.1038/srep08132

Yun, Y.-S., Park, J.., 2001. Attenuation of monochromatic and polychromatic lights in Chlorella vulgaris suspensions. Appl. Microbiol. Biotechnol. 55, 765–770. doi:10.1007/s002530100639

Zavřel, T., Sinetova, M. a., Búzová, D., Literáková, P., Červený, J., 2015. Characterization of a model cyanobacterium Synechocystis sp. PCC 6803 autotrophic growth in a flat-panel photobioreactor. Eng. Life Sci. 15, 122–132. doi:10.1002/elsc.201300165

Zevin, A.S., 2015. Characterization of Structure and Function of Microbial Communities in Synechocystis sp. PCC6803 Photobioreactors.

Zhou, W.L., Qiao, X., Sun, J., Xing, K., Tang, X.X., 2011. Ecological effect of Z-QS01 strain on Chlorella vulgaris and its response to UV-B radiation stress. Procedia Environ. Sci. 11, 741–748. doi:10.1016/j.proenv.2011.12.115

Zonneveld, C., 1997. Modeling effects of Photoadaption on the Photosynthesis-Irradiance Curve. J. Theor. Biol. 186, 381–8.